Electrodeposition and Electroless Deposition of Copper in Interconnect Technology and Biotechnology Related Applications

Xiaoxuan Sun

Submitted in partial fulfillment of the
requirements for the degree of
Doctor of Philosophy
in the Graduate School of Arts and Sciences

COLUMBIA UNIVERSITY

2015

ABSTRACT

Electrodeposition and Electroless Deposition of Copper in Interconnect Technology and Biotechnology Related Applications

Xiaoxuan Sun

Electroless copper deposition is a promising alternative technique for interconnect fabrication because it may be difficult for electrodeposition to fill features that are 10 nm and smaller. An electroless copper bath of low toxicity and mild operating conditions with dimethylamine borane (DMAB) as reducing agent was examined. The results were interpreted within the framework of mixed potential theory, and a strong catalytic effect of the presence of the anodic reaction to the cathodic reaction was observed, possibly due to a significant pH decrease near the electrode that impacts the chelation of cupric ions. It was also found that the nucleus density not only depends on the type of substrates, but is also controllable by pH, temperature and the addition of PEG.

Whether electroless deposition will be implemented in manufacturing is dependent on continued improvements in electrodeposition, and organic additives play a major role in efficacy. Development of advanced additives continues, and two lab scale tools that facilitate additive studies are designed and implemented. A membrane-separated cell was developed to effectively differentiate additive aging on the cathode side and anode side. Additive behavior in the cell was characterized

by cyclic voltammetric stripping (CVS), and a significant aging effect of bis (3-sulfopropyl) disulfide (SPS) on the cathode side was observed. The rate of aging increases at higher acid level and lower current density, yet decreases in the presence of PEG. Complex wafer plating tools have been developed for use in manufacturing to guarantee a high uniformity of copper electrodeposition. Wafer size tools were "scaled down" for lab use by introduction of a simple insulating shield system for coupon size plating studies to avoid poor current distribution. By numerical simulation, sensitivities of parameters were systematically studied, with which the optimum shield design was made. The design reduced the spatial variation in current density from 18% to only 3%.

Copper deposition can be applied to other applications, and naturally constraints on processing can be very different. For example, for biosensor applications, copper deposition can be a signal amplification method of binding to engineered phages. Chapter 5 demonstrates the use of electroless copper deposition to image phage with both high sensitivity and low operational time and cost. A correlation between copper quantity and phage concentration was established, with a limit of detection in ppt level. A pre-concentration device can be utilized to detect phage of lower concentrations without significantly increasing the time for detection. In another example, copper deposition may be used in an integrated process to produce a biofuel. Here, the process is akin to copper electrowinning processes albeit with modified electrolytes. A design of the electrowinning cell was built in-house and showed product yield capability and scalability to serve the bioreactor. Lower cell potentials were demonstrated by utilizing novel mixed metal

oxides anodes. Copper deposit adhesion depended on electrolyte composition, and this impacts bioreactor performance. The current efficiency during electrowinning is between 70% and 90% depending on electrolyte composition.

TABLE OF CONTENT

LIST OF FIGURES

Chapter 2

Chapter 3

Chapter 4

Chapter 5

film was formed within the spotted area, except that most of the phage aggregated and aligned on the “hydro ring”

Figure 5. $PdCl_2$ calibration curve, showing the detection limit of $PdCl_2$ on filter paper and how prolonged deposition detected lower concentration of catalyst

Figure 6. Detection of insertless phage and RDX binding peptide phages on filter paper with phage not catalyzed by Pd, phage catalyzed by Pd and filtered solution of the mixture of phage and Pd catalyzation solution.

Figure 7. Phage concentration calibration curve with respect to the area of deposit after 3 minutes of deposition. The pasteurized well plate has polystyrene surface. Starting from top left well with E14 concentration, each well contained half concentration of the previous well, all the way to the bottom of second column of 3E9

Figure 8. Phage concentration calibration curve with respect to the time it took for deposit to appear. The pasteurized well plate has polystyrene surface. Starting from top left well with E14 concentration, each well contained half concentration of the previous well, all the way to the bottom of second column of 3E9

Figure 9. Electroless copper deposition (5 min) of catalyzed phage on silica filter column substrates (a) Appearance of deposit with labeled phage concentration and 20 μL phage applications (b) Appearance of different concentrations and volumes of phage with the control sample (TBS buffer with 50 mM Tris-HCl with 150 mM NaCl, pH 7.9)

Chapter 6

Figure 9. Dependence of cell voltage on applied current from 1 A to 16 A. Observation is done both at the onset and 4 hour of electrowinning experiment. Normal electrolyte and platinized titanium anode was used.

LIST OF TABLES

Chapter 2

Chapter 3

Chapter 4

Chapter 5

Acknowledgements

I would like to express my sincere gratitude to my advisor Professor Alan C. West for all his contributions of time, ideas and funding to make this work possible. Over the five years of my PhD, I have received invaluable support from Processor West, not only on my research but also my career development in general. I deeply appreciate his advise, guidance and mentorship.

I am also indebted to all my laboratory colleagues from West group, especially Dr. Igor Volov, Dr. Robert von Gutfeld, Dr. Damla Eroglu and Dr. Asli Sahin, for their help, advice and encouragement; Dr. Feng Qiao for his collaboration on my projects and his friendship; and Sheng-Hua Tsai, Yanbo Qi, Danjie Lu, Qian Zhang and Jingyang Guan for their productive support on the experiments. I would also like to extend my gratitude to Professor Scott A. Banta and Dr. Jennifer Haghpanah in particular, for their tremendous input and efforts during our collaborations.

Finally, I want to thank my family, especially my parents for their endless support and faith in me in every step of my life; and Zhe Kang, who became my wife during the journey of my PhD. She has supported me in everything I did with great love, understanding, encouragement and trust. For that I am deeply grateful.

Chapter 1:

Introduction

Overview of Copper Electrodeposition and Electroless Deposition

Electrodeposition (or electroplating) is a process that uses electric current to reduce dissolved metal cations into elemental metal state to form a coherent metal coating on electrodes. Copper is one the most common metals electroplated.[1] It has a soft, red, ductile and solderable surface. Electroplated copper is not only used in traditional applications such as plating on plastics, zinc die castings, automotive bumpers, electrorefining and electroforming, but also in modern fabrication techniques, such as printed circuit boards and semiconductor devices.[2] Copper plating systems that have been commercially used are the alkaline cyanide and pyrophosphate complex ion systems and the acid sulfate and fluoborate simple ion systems.[3] Currently, most copper deposition is performed in an acid copper bath that contain copper sulfate, sulfuric acid and various organic and inorganic additives. The electrodeposition of copper in such bath is considered to go through two steps:

$$Cu^{2+} + e^- \rightleftharpoons Cu^+ \quad (1)$$

$$Cu^+ + e^- \rightleftharpoons Cu \quad (2)$$

Electroless copper deposition, on the other hand, is similar to electrodeposition in that copper coating is deposited from an aqueous solution, yet different in that reducing agents are used in place of an external current source.

From a thermodynamic point of view, the electroless deposition can be considered as a purely spontaneous chemical process, which involves oxidation-reduction reactions.

There are two main types of electroless deposition, displacement deposition and autocatalytic deposition. Displacement deposition is also known as immersion plating, where a less noble metal is replaced by more noble metal when it is immersed into a solution that contained ions of the more noble metal. In this case, the reducing agent is the less noble metal and the deposition proceeds exclusively at the surface of the less noble metal. In the autocatalytic deposition, reducing agents are present in the solution, and constantly catalyzed by the metal to be reduced, enabling continuous growth of the deposit. In the scope of the thesis, only autocatalytic deposition is discussed.

Several types of reducing agents in electroless copper deposition have been used, such as formaldehyde, sodium hypophosphite, glyoxylic acid and dimethylamine borane (DMAB), with formaldehyde being the most widely used. The overall reaction for electroless copper deposition with formaldehyde as the reducing agent is:

$$Cu^{2+} + 2HCHO + 4OH^{-} \rightarrow Cu + 2HCOO^{-} + 2H_2O + H_2 \quad (3)$$

The rate-determining step for electroless copper deposition is most frequently associated with the anodic process, which is generally under kinetic control. Thus the catalytic activity of the substrate significantly affects the bath performance. For electroless copper bath with formaldehyde as reducing agent, copper itself is a very strong catalyst, more catalytic than gold, silver platinum, palladium and other

metals.[4] Because of the need of a catalyst to initiate the autocatalytic process, the reaction occurs on the substrate rather than in the bulk. However, at aggressive conditions, especially when significant concentration of free cupric ion exists in the solution, the process can also occur in the bulk, which is called “plate out” and also known as bath instability. Chelating agents are thus necessary in the solution to preserve most oxidized copper in chelated form. Typical chelating agents are ethylenediamine tetraacetic acid (EDTA), Rochelle salt and triethanol amine. Furthermore, as shown in reaction (3), the process consumes hydroxide ions, and thus a pH buffer is needed to maintain the pH to be relatively stable.

Although the most robust and generally having the best performance, the electroless copper bath with formaldehyde has disadvantages due to its high toxicity and demanding operating conditions of high temperature and high pH of around 12.5. Alternative reducing agents of lower toxicity and less demanding operating conditions are being explored to replace formaldehyde.

The scope of this thesis is aimed towards the application of electrodeposition and electroless deposition of copper to two areas: interconnect fabrication and biotechnology related fields.

Copper Interconnect Fabrication

Interconnects are the conductors on a chip that electrically connects all the functional electronic components, such as transistors, diodes and resistors.[5-7] Since 1997, when IBM first introduced its successful development of copper plating technology for fabrication of chip interconnects structure, copper has continued to

replace aluminum as the material for interconnects due to its superior conductivity and resistance to electromigration, and electrodeposition has been the technique for copper interconnect fabrication.[8-10]

Interconnect fabrication starts by patterning dielectric (e.g. silicon dioxide) with photolithography, on top of which a barrier layer (such as Ta, TaN and TiN) is deposited in high vacuum either with physical or chemical vapor deposition to prevent the diffusion of copper into the dielectric material.[11-13] Since the barrier layer is normally of low conductivity, a thin copper seed layer is deposited by physical vapor deposition to minimize the substrate resistance and to enable adhesion in preparation for the subsequent electrodeposition process. In the electrodeposition process, a wafer that is electrically connected on the perimeter is immersed into an acid copper plating bath. When a current is applied through the connection, current distributes on the wafer and copper film forms by reducing cupric ions close to the substrate. The final surface planarization step is accomplished by chemical mechanical polishing (CMP).[14]

The key in successful interconnect fabrication by copper electrodeposition is filling deep and narrow features (vias and trenches) without defects (such as voids and seams). This is accomplished by superconformal bottom-up filling enabled by using a combination of suppressor and accelerator that preferentially suppresses the sidewalls and top entrance of features rather than the bottom.[15-19] Suppressors are typically polymers containing ethylene or propylene glycol such as polyethylene glycol (PEG), which suppress copper deposition, especially in the presence of chloride ions.[20-24] Accelerators typically contain mercapto/disulfide and sulfonate

groups such as bis (3-sulfopropyl) disulfide (SPS) and 3-mercapto-1-propane sulfonic acid (MPSA). They accelerate deposition through either competitive adsorption with suppressors or catalytic reduction of Cu^{2+} by oxidation of MPSA to SPS. [15, 16, 25-30]

Although electrodeposition has served well in fabricating copper interconnects for the last two decades, the continued scaling of feature sizes is pushing the technique to its limit at wire sizes of 10 nm and below. At such scales, it becomes increasingly difficult to form a continuous Cu seed layer on the sidewalls of fine via holes, which is indispensible for subsequent electroplating.[31-34] Also, the decreasing size leaves even smaller room to deposit a seed layer. Furthermore, a thinner seed layer will inevitably result in a lower conductivity, and thus a pronounced potential loss across the wafer during electrodeposition.

In the first part of the thesis, electroless copper deposition is presented in chapter 2 as a potential technique for next-generation interconnect fabrication at feature sizes of 10 nm and smaller. In chapter 3 and 4 respectively, two lab-scale copper electrodeposition issues are addressed associated with additive studies and deposit uniformity.

Electroless Copper Deposition for next-generation Interconnect Fabrication

Electroless copper deposition, which may not require a vapor-deposited seed layer, is a means of filling high aspect ratio features.[35-40] An electroless Cu deposition process for filling trench patterns should be simple, safe, and inexpensive.

It must further be anticipated to result in conformal coverage. In filling extremely small features, it is also necessary that copper nuclei coalesce to a continuous film at a very thin thickness. The coalescence thickness is reversely correlated with copper nucleus density on the substrate, and thus it is desirable to develop methods to increase the nucleus density.

A non-traditional electroless copper bath with DMAB as the reducing agent was chosen over formaldehyde bath due to its lower toxicity and milder operating conditions. Systematic evaluation of bath performance with various parameters was carried out. The results was interpreted in the framework of mixed potential theory and a strong catalytic effect of anodic reaction to the cathodic reaction was observed, not seen in the traditional formaldehyde bath. The nucleation study results showed multiple parameters that may be used to achieve desirable nucleation densities.

Additive Aging Studies for Copper Electrodeposition process

The presence of an appropriate amount of accelerator in the solution is critical in filling small features without voids or other defects. However, SPS decomposes during the electrodeposition process through complex interactions involving copper, Cu^{+}, Cu^{2+}, thiol/disulfide, oxygen and related products.[30, 41-43] From a practical perspective, the degradation of SPS may significantly complicate process control. Most of the aging studies have been aimed at additive interactions with the anode, either ascribing to a high anodic potential that oxidizes SPS on insoluble anodes, or the generation of cuprous ion that oxidizes SPS with dissolved oxygen on copper anodes.[30, 44, 45] Membrane-separated cells, can effectively prevent

the diffusion of additives from one side to the other, but they can lead to an increase in copper concentration and depletion of acid in the anolyte and the reverse in the catholyte. A replenishment system is thus needed to maintain the solution composition. It is desirable to have a lab-scale aging device that simplifies the process. Furthermore, few efforts have been done at separating the impact of anode and cathode on aging.

In chapter 3, a cell design is presented, which facilitates additive aging studies with membrane-separated anolyte and catholyte compartments. The anolyte chemistry is modified to reduce or eliminate the need for catholyte replenishment of cupric ions or pH values. A modified electrochemical technique is employed to quantify effective SPS concentrations throughout the aging process. The aging of SPS on cathode was found to be significant and its aging behavior was characterized at varied acid levels, current densities and the presence/absence of PEG.

Copper Electrodeposition Uniformity on Coupons

In the attempt to minimize non-uniformity of copper electrodeposition over wafers, industry manufacturers have invested in designing optimum plating tools including complex electric-field-disturbing shields. However, such tools are almost non-existent for rotating disk coupon plating setup in beaker system, which is widely used in lab-scale electrodeposition studies. The lack of appropriate plating tools often results in current distribution profile over substrates with “high-edges” and “low-centers”. A nonuniform current distribution also leads a significant fraction of the area not depositing at the specified current density, rendering it difficult to

study the additives. For example, if a current density of 20 mA/cm^2 is specified, the center might deposit at only 15 mA/cm^2, while the edge at 25 mA/cm^2. The current density is an important electrochemical parameter that dictates many aspect of deposition, such as deposit quality, nucleation properties, and additive behavior. Thus a non-uniform current distribution can lead to difficulty in interpreting lab-scale plating studies and induce systematic error.

However, due to the complexity, the well-optimized wafer size tools cannot be easily "scaled down" for coupon size applications. A shield design is difficult without numerical simulation to systematically evaluate the sensitivity of design parameters on the distribution of current density. Through simulation, a shield that can be directly integrated to a rotating disk setup was designed. The practical shield design effectively reduces the variation in current density.

Copper Deposition in Biotechnology Related Fields

The second part of this thesis describes two applications of copper deposition in biotechnology related fields: biosensor signal amplification with electroless copper deposition and biofuel generation powered indirectly by electricity. Although the requirements for the two applications are quite different, the goals are accomplished by coupling the power of engineered biological elements with copper deposition.

Biosensor signal amplification with electroless copper deposition

Palladium and some other catalysts such as gold have been widely used to catalyze non-metallic substrates to initiate the electroless deposition process.[46-50] Recently, a selective catalyzation technique was developed based on the fact that Pd^{2+} tends to chemically bind ligands containing nitrogen, sulfur and phosphorous donor atoms,[51-53] particularly amines, thiols[54, 55] and pyridine[52] groups. Once the electroless copper deposition process initiates on such catalyzed substrate, copper deposition can continue to deposit to significant thickness and one can see from the appearance that a copper film is being formed.

Recently, phage has been engineered to display certain peptides that have strong affinity to explosives such as TNB and TNT.[56-58] These explosives can contaminate groundwater, sediments, soil, and surfaces waters. However, detection methods that can be used in the field are lacking. Using phage to specifically bind to a target explosive is of interest, yet no simple method has been developed to amplify the signal of phage concentration in the field.

The phage contains dense functional groups such as amines and thiols, which selectively trap free Pd^{2+} in the catalyzation solution onto the surface to serve as strong catalyst for copper deposition. And that is where the interface between the biosensor and electroless deposition emerges. By first catalyzing phage with palladium, the electroless copper bath selectively coated the phage with copper in contrast to multiple substrates. A correlation between copper quantity and phage concentration was established, with the limit of detection in ppt level. A pre-concentration device can also be utilized to detect phage of lower concentrations without significantly increasing the time for detection.

Design of a Copper Elelctrowinning Cell

Recently, *Acidithiobacillus ferrooxidans* bacteria have been genetically modified to fix gaseous CO_2 to produce valuable chemicals or biofuels by extracting energy from the oxidation of ferrous ion using atmospheric O_2 as the electron acceptor:[59, 60]. *A. ferrooxidans* cells are attractive candidates for electrofuels application as they grow planktonically and the Fe^{3+} produced by the cells can be readily reduced electrochemically. However, under the conditions optimum for cell growth, the solubility of Fe^{3+} is very low, resulting in limited energy density. [61] A coupled system was proposed to significantly improve existing energy density by utilizing Cu^{2+}/Cu redox mediator.

Whether the Cu^{2+}/Cu redox mediator can be successfully implemented to continuously sustain a high bacteria yield in the bioreactor depends on the capability of the electrochemical cell. Compared to the electrochemical cell that aims at reducing ferric ion to ferrous ion at relatively low rates, the electrochemical cell in the coupled system aims at reducing cupric ion to solid-state copper on the cathode at substantially higher rates. The deposited copper is then transferred to another reactor to reduce ferric ions generated in the bioreactor. A poor adhesion of copper deposit makes the process inefficient. From an economic point of view, it is desirable to minimize the cell's power consumption while maintaining a high rate of product yield.

These goals and requirements of the electrofuels process are similar to the copper electrowinning process albeit with modified electrolytes. The electrowinning

of copper derived from leaching, or solvent extraction is one of the largest contributors to the global copper commodity supply, and the electrowinning process is a well-developed and widely utilized technique in the industry.[62, 63] In copper electrowinning, a current is passed from the inert anodes through a liquid solution containing cupric ions to the cathodes, where cupric ions are reduced to form a copper sheet.

A copper electrowinning cell customized for the coupled system is thus designed and presented. The cell demonstrated great product yield capability and scalability to serve the bioreactor. Power consumption is minimized by utilizing novel mixed metal oxides anodes. Under optimized conditions, both good deposit quality and high current efficiency was achieved.

Reference

1. L. W. Flott, Metal Finishing **94** (3), 55-58 (1996).

2. R. Sard, M. B. Bever, Ed. ed. (Wiley, New York, 1986).

3. J. W. Dini and D. D. Snyder, in *Modern Electroplating* (John Wiley & Sons, Inc., 2010), pp. 33-78.

4. I. Ohno, O. Wakabayashi and S. Haruyama, J Electrochem Soc **132** (10), 2323-2330 (1985).

5. G. M. Schmid, M. D. Stewart, J. Wetzel, F. Palmieri, J. Hao, Y. Nishimura, K. Jen, E. K. Kim, D. J. Resnick, J. A. Liddle and C. G. Willson, Journal of Vacuum Science & Technology B **24** (3), 1283-1291 (2006).

6. N. Kumar and C. W. C. Lin, (Google Patents, 1992).

7. T. J. Licata, E. G. Colgan, J. M. E. Harper and S. E. Luce, Ibm J Res Dev **39** (4), 419-435 (1995).

8. P. C. Andricacos, C. Uzoh, J. O. Dukovic, J. Horkans and H. Deligianni, Ibm J Res Dev **42** (5), 567-574 (1998).

9. D. Edelstein, J. Heidenreich, R. Goldblatt, W. Cote, C. Uzoh, N. Lustig, P. Roper, T. McDevitt, W. Motsiff, A. Simon, J. Dukovic, R. Wachnik, H. Rathore, R. Schulz, L. Su, S. Luce and J. Slattery, presented at the Electron Devices Meeting, 1997. IEDM '97. Technical Digest., International, 1997 (unpublished).

10. T. Nogami, A. Preusse and V. Dubin, (Google Patents, 2000).

11. R. N. Hall and J. H. Racette, J Appl Phys **35** (2), 379-397 (1964).

12. M. Stavrev, D. Fischer, C. Wenzel, K. Drescher and N. Mattern, Thin Solid Films **307** (1–2), 79-88 (1997).

13. O. Chyan, T. N. Arunagiri and T. Ponnuswamy, J Electrochem Soc **150** (5), C347-C350 (2003).

14. J. M. Steigerwald, S. P. Murarka and R. J. Gutmann, *Chemical Mechanical Planarization of Microelectronic Materials*. (Wiley, 2008).

15. T. P. Moffat, J. E. Bonevich, W. H. Huber, A. Stanishevsky, D. R. Kelly, G. R. Stafford and D. Josell, J Electrochem Soc **147** (12), 4524-4535 (2000).

16. T. P. Moffat, D. Wheeler and D. Josell J Electrochem Soc **151** (4), C262-C271 (2004).

17. J. W. Gallaway, M. J. Willey and A. C. West, J Electrochem Soc **156** (4), D146-D154 (2009).

18. T. P. Moffat and D. Josell, J Electrochem Soc **159** (4), D208-D216 (2012).

19. D. Josell, D. Wheeler and T. P. Moffat, J Electrochem Soc **159** (10), D570-D576 (2012).

20. J. W. Gallaway and A. C. West, J Electrochem Soc **155** (10), D632-D639 (2008).

21. J. W. Gallaway, M. J. Willey and A. C. West, J Electrochem Soc **156** (8), D287-D295 (2009).

22. M. E. Huerta Garrido and M. D. Pritzker, J Electrochem Soc **155** (4), D332-D339 (2008).

23. M. L. Walker, L. J. Richter and T. P. Moffat, J Electrochem Soc **152** (6), C403-C407 (2005).

24. K. R. Hebert, S. Adhikari and J. E. Houser, J Electrochem Soc **152** (5), C324-C329 (2005).

25. T. P. Moffat, D. Wheeler, S.-K. Kim and D. Josell, J Electrochem Soc **153** (2), C127-C132 (2006).

26. N. T. M. Hai, K. W. Krämer, A. Fluegel, M. Arnold, D. Mayer and P. Broekmann, Electrochim Acta **83** (0), 367-375 (2012).

27. N. T. M. Hai, T. T. M. Huynh, A. Fluegel, M. Arnold, D. Mayer, W. Reckien, T. Bredow and P. Broekmann, Electrochim Acta **70** (0), 286-295 (2012).

28. J. J. Kim, S.-K. Kim and Y. S. Kim, J Electroanal Chem **542** (0), 61-66 (2003).

29. A. Frank and A. J. Bard, J Electrochem Soc **150** (4), C244-C250 (2003).

30. T. P. Moffat, B. Baker, D. Wheeler and D. Josell, Electrochem Solid St **6** (4), C59-C62 (2003).

31. T. Nguyen, L. J. Charneski and D. R. Evans, J Electrochem Soc **144** (10), 3634-3639 (1997).

32. N. M. Martyak and P. Ricou, Materials Science in Semiconductor Processing **6** (4), 225-233 (2003).

33. J. Reid, S. Mayer, E. Broadbetrt, E. Klawuhn and K. Ashtiani, Solid State Technology **43** (7), 86-103 (2000).

34. E. Webb, C. Witt, T. Andryuschenko and J. Reid, Journal of Applied Electrochemistry **34** (3), 291-300 (2004).

35. Y. Lantasov, R. Palmans and K. Maex, Microelectron. Eng. **50** (1-4), 441-447 (2000).

36. V. M. Dubin, Y. ShachamDiamand, B. Zhao, P. K. Vasudev and C. H. Ting, J Electrochem Soc **144** (3), 898-908 (1997).

37. H. H. Hsu, K. H. Lin, S. J. Lin and J. W. Yeh, J Electrochem Soc **148** (1), C47-C53 (2001).

38. J. J. Kim, S. H. Cha and Y. S. Lee, Japanese Journal of Applied Physics Part 2-Letters & Express Letters **42** (8A), L953-L955 (2003).

39. Z. L. Wang, O. Yaegashi, H. Sakaue, T. Takahagi and S. Shingubara, Mat Res S C, 567-572 (2004).

40. Z. L. Wang, Z. J. Liu, H. Y. Jiang and X. W. Wang, J Vac Sci Technol B **24** (2), 803-806 (2006).

41. J. P. Healy, D. Pletcher and M. Goodenough, J Electroanal Chem **338** (1–2), 179-187 (1992).

42. W. O. Freitag, C. Ogden, D. Tench and J. White, Plat Surf Finish **70** (10), 55-60 (1983).

43. N. A. Zhukauskaite, A. Y. Lazauskene and A. A. Malinauskas, Prot Met+ **25** (2), 244-248 (1989).

44. S.-K. Kim and J. J. Kim, Electrochemical and Solid-State Letters **7** (9), C98-C100 (2004).

45. C. Gabrielli, P. Mocoteguy, H. Perrot, A. Zdunek and D. Nieto-Sanz, J Electrochem Soc **154** (3), D163-D169 (2007).

46. S. Yokogawa, K. Kikuta, H. Tsuchiya, T. Takewaki, M. Suzuki, H. Toyoshima, Y. Kakuhara, N. Kawahara, T. Usami, K. Ohto, K. Fujii, Y. Tsuchiya, K. Arita, K. Motoyama, M. Tohara, T. Taiji, T. Kurokawa and M. Sekine, Ieee T Electron Dev **55** (1), 350-357 (2008).

47. T. Ishigami, T. Kurokawa, Y. Kakuhara, B. Withers, J. Jacobs, A. Kolics, I. Ivanov, M. Sekine and K. Ueno, Proceedings of the Ieee 2004 International Interconnect Technology Conference, 75-77 (2004).

48. Y. e. a. kakuhara, Proc. 2009 Int. Conf. Solid State Device and Materials, 804 (2009).

49. Y. e. a. Hayashi, Proc. 2009 IITC(IEEE 2009), 252.

50. W. K. Han, G. H. Hwang, S. J. Hong, H. H. An, C. S. Yoon, J. H. Kim, M. J. Lee, G. Hong, K. S. Park and S. G. Kang, Appl Surf Sci **256** (8), 2649-2653 (2010).

51. P. M. Maitlis, Academic Press, New York (1971).

52. W. J. Dressick, C. S. Dulcey, J. H. Georger, G. S. Calabrese and J. M. Calvert, J Electrochem Soc **141** (1), 210-220 (1994).

53. N. Kulyk, S. Cherevko and C. H. Chung, Electrochim Acta **59**, 179-185 (2012).

54. L. N. Xu, J. H. Liao, L. Huang, N. Gu, H. Q. Zhang and J. Z. Liu, Appl Surf Sci **211** (1-4), 184-188 (2003).

55. M. Ishida, M. Kasuga, T. Kaneko and T. Shimoda, Jpn J Appl Phys 2 **39** (3ab), L227-L229 (2000).

56. E. R. Goldman, M. P. Pazirandeh, P. T. Charles, E. D. Balighian and G. P. Anderson, Analytica Chimica Acta **457** (1), 13-19 (2002).

57. B. Krebs, H. Griffin, G. Winter and S. Rose-John, Journal of Biological Chemistry **273** (5), 2858-2865 (1998).

58. A. D. Griffiths, S. C. Williams, O. Hartley, I. Tomlinson, P. Waterhouse, W. Crosby, R. Kontermann, P. Jones, N. Low and T. J. Allison, The EMBO journal **13** (14), 3245 (1994).

59. M. P. Silverman and D. G. Lundgren, J Bacteriol **77** (5), 642-647 (1959).

60. M. Nemati, S. T. L. Harrison, G. S. Hansford and C. Webb, Biochemical Engineering Journal **1** (3), 171-190 (1998).

61. K. H. Gayer and L. Woontner, The Journal of Physical Chemistry **60** (11), 1569-1571 (1956).

62. N. T. Beukes and J. Badenhorst, J S Afr I Min Metall **109** (6), 343-356 (2009).

63. W. C. Cooper, Journal of Applied Electrochemistry **15** (6), 789-805 (1985).

Chapter 2:

Growth Kinetics and Nucleation of Copper Electroless Deposition with Dimethylamine Borane as Reductant

Abstract

Electroless copper deposition may be a strong candidate to replace electrodeposition in fabricating 10 nm and smaller interconnects. Among others, a type of electroless copper bath with dimethylamine borane (DMAB) as reducing agent is of great interest because of its mild operating conditions and low toxicity. However, compared with more common chemistries, the bath is much less understood. Additionally, little is known about controlling nucleation properties in order to achieve such small yet continuous copper structures. In this study, the sensitivity of deposition rates was examined to a variety of parameters. The results were interpreted in the framework of mixed potential theory and also showed a strong catalytic effect of the presence of the anodic reaction to the cathodic reaction, possibly due to a significant pH decrease near the electrode that impacts the chelation of cupric ions. The initial stages of copper electroless deposition were visualized and characterized by nucleation followed by coalescence and film growth. The dependence of the density of copper nuclei was explored in terms of operating conditions, substrate types and addition of additive.

Introduction

In advanced semiconductor device manufacturing, copper is the current choice of the interconnect metal due to its low resistivity and superior resistance against electromigration compared with conventional aluminum alloys.[1] Electrodeposition has been the primary means of producing metallization due to its bottom-up filling capability using organic additives.[2, 3] However, as the critical feature size continues decreasing, it becomes increasingly difficult to form a continuous Cu seed layer on the sidewalls of fine via holes, which is indispensible for subsequent electroplating.[4-7]

Electroless copper deposition, which may not require a vapor-deposited seed layer, is a means of filling high aspect ratio features.[8-13] An electroless Cu deposition process for filling trench patterns should be simple, safe, and inexpensive. It may further be anticipated to result in conformal coverage; however, it does require an activation process to initiate the autocatalytic electroless deposition. In other applications, $PdCl_2$ and $SnCl_2$ solutions are used to create Pd-metal catalytic particles.[14-17] However, the synthesized Pd catalysts may have irregular shapes and a broad size distribution ranging from nanometers to micrometers. As a result, this activation approach may not be easily applied to damascene copper process with feature sizes on the sub-10-nm scale.

A typical copper electroless bath contains a copper source, typically cupric sulfate or cupric chloride; a chelating agent, such as EDTA or tartrate to stabilize cupric ions, a reducing agent, which ideally is only able to reduce Cu on catalytic substrates, like palladium, or just-deposited copper itself. The electrolyte typically

also contains a pH buffer to counteract pH decrease resulting from consumption of hydroxide ions during oxidation of the reducing agent.

In addition, an electrolyte may contain additives to improve plating properties, such as uniformity, adhesion or morphology. One particular organic additive we included in this study is Polyethylene Glycol (PEG). PEG is a common suppressor that facilitates bottom-up via and trench filling and imparts desirable film qualities[18, 19]. Common copper electroless-deposition baths use formaldehyde as reducing agent.[20-22] Compared to other reducing agents, a formaldehyde bath usually has high deposition rates, long electrolyte stability and good film conductivity and mechanical characteristics. However, drawbacks exist in its volatility, toxicity, instability and the high alkalinity of the bath. Glyoxylic acid is another widely used reducing agent, but also operates at high pH.[23] A hypophosphite-based bath operates at a lower pH of 9 and is stable and safe, but it requires nickel ions in the solution to catalyze the deposition, resulting in co-deposited nickel in the copper film and decreased conductivity. In order to overcome this barrier, alternative approaches are required.

Dimethylamine borane (DMAB) bath, which was first proposed by Jagannathan, operates at a lower pH range.[24] It was stated that the copper obtained was of superior quality, having a higher conductivity and low roughness. High stability of several days was achieved by simultaneously using the strong chelating agent EDTA and the strong buffer Triethanolamine (TEA). Recently, Kulyk studied how pH affects the prevailing deposition mechanism in the bath and the deposition

rate; they also successfully deposited copper film onto a polyimide substrate with the bath.[25]

In this study, we report on the sensitivity of deposition rate to pH, temperature, bath constituents and additives. We interpreted the results with mixed potential theory and examined the dependence of each half-cell to the other. Further, we investigated how nucleation density varies with different operating conditions, substrate types and additives. In many cases, copper nuclei grow in a three-dimensional hemispherical mode, and the film coalesces when adjacent nuclei merge[26]. Therefore, by increasing the nucleation density, we can reduce the distance between nuclei and thus form a complete film at smaller thickness. We also report results on electroless deposition onto self-assembled monolayers (SAM) activated with $PdCl_2$ salt.[27] Ideally, Pd catalysts would align with the highly dense and ordered SAM molecules, generating high nucleus densities.[28]

Experiment

In all electroanalytical studies, we carried out experiments using an EcoChemie type III μAutolab potentiostat. The counter and reference electrodes were Pt wire and Ag/AgCl respectively. In the half-cell studies, linear sweep voltammetry (LSV) and open-circuit potential (OCP) measurements were performed on a rotating disk electrode (RDE) pre-deposited with a uniform copper layer, where either copper source or reducing agent was missing. All OCP measurements were performed by the chronopotentiometric method in a two-electrode cell.

Four-point probe measurements (Jandel) were made with a Keithley 2400 SourceMeter. All experiments were carried out on 1 cm square wafer coupons with 100 nm Cu seed layer. Cu film thickness before and after deposition was inferred from the sheet resistance change, assuming a constant resistivity of copper.

Quartz Crystal Microbalance (QCM) measurements were made with a phase-lock oscillator (PLO-10i, Maxtex) and a frequency counter (53131A, Agilent Technologies). 5 MHz, 1-inch diameter quartz crystals were plated with Au on both sides (Inficon). The crystals were electroplated with one micron of Cu by galvanostatic methods before each experiment. The QCM measures the frequency variation to correlate with the weight gain (thickness change) of the crystal.

Scanning Electron Microscopy (SEM) experiments were performed on a Hitachi 4700. About 1 cm square wafer coupons with either PVD Copper seed, PVD ruthenium, cobalt or SAM was used as substrate. For coupons with Cu seed layer, we first rinsed in citric acid (pH 3) for about 1 min to remove surface oxides prior to immersion into Cu ELD solutions. Nucleus density was manually counted from the SEM images.

To obtain a SAM substrate, we started with a silicon wafer coupon. The coupon was first cleaned in Piranha solution (H_2SO_4 : H_2O_2 = 4 : 1) for 5 min, and rinsed thoroughly. The SAM deposition was performed in 0.4 g (3-Aminopropyl) triethoxysilane (APTS) dissolved in 39.6 g toluene for 10 min, at 60°C.[27] Subsequently, the substrate was rinsed in methanol while under ultra sonication to eliminate any extra silane. After forming the SAM, the surface was activated in a

$PdCl_2$ (0.1g/L $PdCl_2$ in 2.5 ml/L dilute HCl) solution for 30s. Finally, the coupon was immersed in the Cu ELD solution.

Copper ELD was performed in solutions containing 0.03 mol/L $CuSO_4 \cdot 5H_2O$, 0.035 mol/L EDTA, 0.1 mol/L DMAB and 0.38 mol/L TEA, unless otherwise noted. Throughout this paper, the molecular weight of the PEG used is 3350 and its concentration is 3g/L. The pH was adjusted by the addition of small amounts of tetramethylammonium hydroxide (TMAH).

Results and discussions

Sensitivity study of the deposition rate

Deposition rate was characterized by an *ex situ* method that measured film electrical resistance with a four-point probe and an *in-situ* method that monitored frequency shift with a quartz crystal microbalance. While the results are consistent, the resistance measurements are characterized by an initial time lag, where the apparent film thickness does not change. This is presumably because individual Cu nuclei do not appreciably alter the sheet resistance until the film coalesces. Figure 1a shows four-point probe measurements demonstrating that increasing pH significantly increased the rate of deposition. This can be understood through the mechanism of the reactions. It is generally assumed that the reducing agent DMAB dissociates easily in alkaline solution:[29]

$$(CH_3)_2NH \cdot BH_3 + OH^- \rightarrow BH_3OH^- + (CH_3)_2NH \quad (1)$$

Then the intermediate hydroxytrihydroborate anion is oxidized through two possible routes. One pathway leads to an exchange of six electrons:[30, 31]

$$BH_3OH^- + 6OH^- \rightarrow B(OH)^-_4 + 3H_2O + 6e^- \quad (2)$$

An alternative oxidation process results in the transfer of only three electrons due to the production of hydrogen gas instead of water:

$$BH_3OH^- + 3OH^- \rightarrow B(OH)^-_4 + 3H_2 + 3e^- \quad (3)$$

Apparently, OH^- is actively involved in both the dissociation of reducing agent DMAB into its active form and its subsequent oxidation. Hence, since the oxidation is considered the limiting step of the ELD process, it is expected that increasing pH would generate higher deposition rate. Figure 1b shows how temperature affects deposition performance during a longer period of time. Obviously, increasing temperature from 22°C to 35°C significantly increased the deposition rate. Also, compared to the increasing deposition rate during the first 20 min shown in Figure 1a, the deposition reaches a steady state after 30 min as shown in Figure 1b.

In order to monitor short times, where Cu is nucleated as individual islands, we used QCM to obtain real-time observation. Figure 2a shows an apparent thickness increase as calculated from the Sauerbrey relationship, where adsorbed mass on the quartz crystal electrode Δm is related to its change in frequency Δf:

$$\Delta m = -C \times \Delta F \quad (4)$$

where C = 20.5 ng Hz^{-1} cm^{-2} as determined by a calibration method recommended by Gabrielli, et al[32].

The figure shows representative results, demonstrating how an increasing concentration of cupric ion or DMAB affects deposition. The deposition rate is not

constant in time, and this is shown more clearly by the differentiation of the data in figure 2a as shown in figure 2b. We found the data appear to be rather scattered in the beginning but start to steadily increase from about 40 seconds to roughly 3 min after which a relatively stable rate is obtained. The gradual increase is most likely due to coverage of PVD copper with just-plated copper with higher surface energy and catalytic activity. From figure 2, it is clear that increasing copper or DMAB concentration both increased the rate of deposition. Averaging the rates of deposition along the "smoother region" from 4 min to 5 min, the baseline chemistry with normal copper and DMAB concentration was 11.8 nm/min, while the additional 50% (0.015 mol/L) copper sulfate and 50% (0.05 mol/L) DMAB respectively promoted the rates by 41% to 16.6 nm/min and 25% to 14.8 nm/min. This result shows that the rate of deposition is sensitive to both reductant and oxidant content.

Apart from the results shown in Figure 1 and Figure 2, we also surveyed other parameters with similar experiments and summarized their rates of deposition for different immersion times in Table 1. The deposition rates in the four-point probe experiments were calculated from the slope of the linearly regressed thickness during the specified period of time, and those in the QCM experiments were the arithmetic average of the deposition rates from 4 min to 5 min after immersion. Results show that elevating pH or temperature significantly increases deposition rate; likewise, increasing concentration of the cupric ions and the reducing agent both tend to increase rate. Also, we found an additional 50% (0.017 mol/L) in the concentration of chelating-agent EDTA leads to a 33% decrease in

deposition rate at pH 8.2 and 22°C. However, when EDTA concentration is cut in half, a rapid homogeneous deposition, also named “plate out”, is observed. This “plate out” effect is due to the stoichiometric excess of cupric ions, resulting in copper ions not stabilized by the EDTA.

Among all these parameters, we found that the rate of deposition is most sensitive to pH change. At 22°C, simply by increasing the pH by 0.45 from 8.2, the rate of deposition more than doubled from 2.1 nm/min to 4.8 nm/min, and another increase of only 0.25 from 8.65 lead to an increase in rate of 2.3 nm/min to 7.1 nm/min. We also observed a similar pattern at 55°C. Starting from 9.8 nm/min at pH 8.2, the rate of deposition increased by 2.0 and 4.7 nm/min respectively with progressive increase in pH to 8.65 and then 8.9. This high sensitivity of deposition rate to pH also stresses the need of utilizing a high capacity buffer in maintaining a consistent bath performance in the long run.

Mixed-potential theory studies

Although the rate of deposition (nm/min) is a fairly intuitive measure to quantify the deposition process, current density (mA/cm^2) is often used in electrochemistry studies to reflect the nature of electron transfer from oxidant to reductant. With the measured rate of deposition, Faraday’s law can predict an expected current density. With the complete bath, we are able to obtain the potential (OCP) and equivalent current density at which the reaction occurs. Half-cell current densities, on the other hand, can be measured either with oxidant removed or reductant removed as a function of applied potential.

According to mixed potential theory, the potential and rate of deposition can be predicted by the intercept of the oxidation and reduction polarization curves, if the anodic and cathodic reactions are non-interacting. Often, the two half reactions interact, presumably by modifying the local electrolyte composition near the electrode. By examining the applicability of mixed potential theory and the dependency of one reaction to the other, insights into the reaction mechanism may be inferred.

One example of mixed potential study is shown in Figure 3 and Figure 4. From Figure 3a, it is clear that copper reduction is insignificant during the negative scan from -0.3V until about -0.6V, while it accelerated significantly at more negative potentials from -0.6V to -0.9V, where deposition occurs. Oxidation polarization was scanned from -0.9V to -0.3V. The rates of oxidation increased with the increase in potential (overpotential) as expected. We show results obtained at pH 8.2, 22°C or pH 8.6, 55°C, with or without PEG. At increasing values of pH and temperature both the reduction rate and oxidation rate increase, consistent with the results of Figure 1. However, although PEG has been proved to be a very strong suppressor in many studies [33, 34], it barely suppressed (polarized) the copper reduction half reaction. In contrast, for DMAB oxidation, as shown in Figure 3b, PEG clearly suppressed the oxidation of DMAB, which might be accountable for the overall suppressing effect for the full bath performance.

In Figure 3c, we show the measured potentials of electrode in the complete electroless copper solutions. It seems that PEG has a negligible impact on the OCP, but higher pH and temperature lowered OCP quite significantly. The current

densities, corresponding to these OCPs and operating conditions, are calculated from rates of deposition in figures 3a and 3b. These potential and current density sets, which represent the complete bath performance, are displayed as points in Figure 4. Additionally, with both cathodic and anodic polarization curves measured from half-cells, the current density and potential as shown in Figure 4 can be predicted. In both cases, the OCP predicted by the polarization curves deviated negatively from the measured values by roughly 100 mV. This suggests that the redox reactions are not independent of each other. A previous study also concluded that at room temperature, the redox reactions are not independent of each other since the intersection of polarization curves fails to predict neither the estimated rates of deposition nor the OCPs[25].

As shown in Figure 4, for the bath with a pH of 8.6 at 55°C, the equivalent current density (1.11 mA/cm^2) is close to the value predicted by the oxidation curve (1.23 mA/cm^2). However, the predicted reduction rate is only 0.28 mA/cm^2, i.e. the presence of oxidation reaction accelerated the reduction rate by a factor of three. Similar results were also seen in the bath operated under pH 8.2 at 22°C. The equivalent current density (0.4 mA/cm^2) at its measured OCP (-0.64V) was similar to the predicted oxidation rate (0.3 mA/cm^2), while again much higher than the predicted reduction rate of only 0.05 mA/cm^2. Both examples suggest that the oxidation reaction is not appreciably influenced by the reduction reaction, while the rate of reduction is strongly catalyzed by the presence of the oxidation reaction.

As shown in reaction (1) through (3), the oxidation of DMAB consumes significant amount of hydroxide ion. In the near field of substrate, a sharp decrease

in pH can be thus expected accompanying the anodic reaction. When the pH is lowered, it is known that the chelating ability of EDTA to cupric ion, or the critical stability constant, decreases significantly.[35] The loss of chelating power of EDTA can lead to increase in the concentration of free cupric ion in the near field and possibly also the rate of deposition, or a catalyzation effect.

Nucleation characteristics on different substrates

By performing electroless deposition on wafer coupons, we were able to examine copper nucleation by *ex situ* SEM. In some cases, wafer coupons with PVD Cu coated were used as the substrate. Figure 5 shows one example of observation of copper deposition with SEM under increasing deposition time. The bright features are copper particles, as confirmed by Energy-dispersive X-ray spectroscopy (EDX). We demonstrate the progression of nucleation, growth, coalescence and subsequent bulk film growth with this method. Apart from the visualization of the process, we were also able to obtain the nucleation densities by counting the number of nuclei in three randomly chosen 3 μm^2 areas and taking the average. Similar experiments were performed at different pH values and temperature. Systematic study was done on PVD copper substrate, but we also report results with other substrates as well in the end of this chapter.

Often, it is assumed that copper nuclei are randomly distributed over the electrode surface and grow in a three-dimensional hemispherical mode[36]. The nuclei coalesce when they grow and impinge on each other.[37] Hence, a higher nucleus density will lead to a thinner coalescence thickness. Quantitatively, the minimum

coalescence thickness of copper (b_{coal}, nm) could be approximately calculated from nucleus density (N, cm^{-2}):[38]

$$b_{coal} = 0.5 \times N^{-0.5} \quad (5)$$

Figure 6 shows the resulting nucleus density as a function of pH. Results are shown with and without PEG. First, if we look at the two curves at 55°C, with or without PEG, we can see that the addition of PEG decreased the nucleation density by about half with all three pH values studied. At pH 8.25, the nucleus density decreased from 3.7×10^{10} cm^{-2} to 1.5×10^{10} cm^{-2}, while at 8.6 it decreased from 0.6×10^{10} cm^{-2} to 0.3×10^{10} cm^{-2}, and at 8.9 from 0.8×10^{10} cm^{-2} to 0.5×10^{10} cm^{-2}.

This effect of PEG on the nucleation density is attributed to its impact on polarization for Cu plating from an acid-copper bath. This polarization is not seen in this chemistry, and a clear explanation is lacking. Interestingly, the lower pH of 8.2 yielded a higher nucleus density, despite its lower growth rate. This may be practically beneficial, since lower growth rates allow a longer operating window and thus better control for Cu to nucleate and coalesce prior to filling of a feature in device manufacturing. Also, we noticed that the film deposited at the pH of 8.2 looked smoother and more uniform. Additionally, if we compare room temperature of 22°C with 55°C both without PEG, the nucleation densities at both pH 8.6 (1.8×10^{10} cm^{-2}) and 8.9 (1.7×10^{10} cm^{-2}) were significantly higher at room temperature. Similarly, the deposition rate operated at room temperature was lower and the film was generally smoother as well.

We also examined electroless copper nucleation performance on other substrates. Ruthenium is interesting because it provides excellent adhesion to both

copper and the underlying barrier. Additionally, it has been shown that electroless copper can directly deposit on pretreated Ru to form smooth, uniform and continuous films.[39] The Ru coupon was pretreated by passing cathodic current at -0.316V *vs.* Ag/AgCl for 1 min in sulfuric acid immediately prior to electroless process. This procedure was originally optimized to effectively remove surface oxides to facilitate nucleation of electrodeposited copper on Ru.[40] As shown in Figure 7, on Ru we achieved higher nucleus density (4.8×10^{10} cm^{-2}) comparable to the highest achieved on Cu (3.7×10^{10} cm^{-2}).

Similarly we deposited onto cobalt coupons as shown in Figure 8a. We found that the resulting nucleus density (1.2×10^{10} cm^{-2}) on Co was lower than that on Cu. This might be due to the fact that Co is a weaker catalyst for electroless copper deposition than Cu.[41] By comparing the OCPs at which copper deposits on Co or Cu substrate as shown in Figure 8b, we found that on copper, the OCP was lower. This is in accordance with most other OCP observations that the faster the deposition, the lower the OCP.

Another approach to increase the nucleus density is to modify a substrate with a self-assembled monolayer (SAM). The SAM then can be used to bind Pd ions (which can be subsequently reduced by the reductant in electroless copper bath in situ). The reduced monolayer of Pd is highly catalytic to electroless deposition, which possibly renders rapid coalescence of nuclei to form a continuous film. The advantage of this approach is to increase the density of active nucleation sites. As shown in Figure 9, we took SEM images after every step of the process. First, the substrate was treated with methanol to remove surface organic contaminant and the

image showed a smooth surface with no nuclei as shown in Figure 9a. Then the cleaned substrate was immersed in SAM developing solution to bond a dense monolayer of SAM onto the silicon surface (top layer rich in native oxide). The SAM exposes amine groups on the top, which tightly bound Pd ions to the surface with its strong affinity to Pd. Subsequently, the bound Pd ions were reduced into Pd nuclei as shown in Figure 9b. Eventually, we deposited copper electrolessly onto the Pd activated surface as shown in Figure 9c. From the preliminary results, we obtained a relatively high nucleus density (3.1×10^{10} cm^{-2}) with this method and one can anticipate a much higher nucleus density and thus smaller coalescence thickness by further optimization.

Conclusions

The DMAB bath performance was characterized, which showed that the rate of deposition most dramatically increases with an increase in pH, followed by temperature and then the concentrations of DMAB and copper sulfate. Inhibition was seen with additional EDTA and the addition of PEG. Mixed potential theory studies revealed a catalytic effect of the presence of the anodic reaction to the cathodic reaction, possibly due to a significant pH decrease near the electrode that impacts the chelation of cupric ions.

Nucleation study results showed that the nucleus density is consistently reduced by the addition of the PEG by about half, that the nucleus density at pH 8.2 is significantly higher than those at pH 8.6 and 8.9, and that the lower temperature of 22°C results in higher nucleus density than at 55°C. The substrate also influences

nucleus density, with the highest nucleus density obtained on pretreated ruthenium, followed by PVD copper and then cobalt. With the use of a combination of SAM pretreatment and Pd activation, copper nuclei was formed onto non-catalytic silica substrate with comparable nucleus density.

ACKNOWLEDGMENTS

This study is financially supported by Semiconductor Research Corporation under the Task ID 2338.001. The authors gratefully acknowledge Yanbo Qi, Qian Zhang and Sheng-Hua Tsai of Columbia University for assistance in performing experiments.

Reference

1. K. Rahmat, O. S. Nakagawa, S. Y. Oh, J. Moll and W. T. Lynch, presented at the Electron Devices Meeting, 1995. IEDM '95., International, 1995 (unpublished).

2. P. C. Andricacos, C. Uzoh, J. O. Dukovic, J. Horkans and H. Deligianni, Ibm J Res Dev **42** (5), 567-574 (1998).

3. T. P. Moffat, J. E. Bonevich, W. H. Huber, A. Stanishevsky, D. R. Kelly, G. R. Stafford and D. Josell, J Electrochem Soc **147** (12), 4524-4535 (2000).

4. T. Nguyen, L. J. Charneski and D. R. Evans, J Electrochem Soc **144** (10), 3634-3639 (1997).

5. N. M. Martyak and P. Ricou, Materials Science in Semiconductor Processing **6** (4), 225-233 (2003).

6. J. Reid, S. Mayer, E. Broadbetrt, E. Klawuhn and K. Ashtiani, Solid State Technology **43** (7), 86-103 (2000).

7. E. Webb, C. Witt, T. Andryuschenko and J. Reid, Journal of Applied Electrochemistry **34** (3), 291-300 (2004).

8. Y. Lantasov, R. Palmans and K. Maex, Microelectron. Eng. **50** (1-4), 441-447 (2000).

9. V. M. Dubin, Y. ShachamDiamand, B. Zhao, P. K. Vasudev and C. H. Ting, J Electrochem Soc **144** (3), 898-908 (1997).

10. H. H. Hsu, K. H. Lin, S. J. Lin and J. W. Yeh, J Electrochem Soc **148** (1), C47-C53 (2001).

11. J. J. Kim, S. H. Cha and Y. S. Lee, Japanese Journal of Applied Physics Part 2-Letters & Express Letters **42** (8A), L953-L955 (2003).

12. Z. L. Wang, O. Yaegashi, H. Sakaue, T. Takahagi and S. Shingubara, Mat Res S C, 567-572 (2004).

13. Z. L. Wang, Z. J. Liu, H. Y. Jiang and X. W. Wang, J Vac Sci Technol B **24** (2), 803-806 (2006).

14. P. P. Lau, C. C. Wong and L. Chan, Appl Surf Sci **253** (5), 2357-2361 (2006).

15. P. P. Lau, C. C. Wong, L. Chan, A. See and S. B. Law, J Electrochem Soc **151** (6), C436-C438 (2004).

16. S. W. Hong, Y. S. Lee, K. C. Park and J. W. Park, J Electrochem Soc **150** (1), C16-C18 (2003).

17. R. L. Cohen and K. W. West, J Electrochem Soc **120** (4), 502-508 (1973).

18. M. J. Willey and A. C. West, J Electrochem Soc **154** (3), D156-D162 (2007).

19. C. H. Lee, S. C. Lee and J. J. Kim, Electrochim Acta **50** (16-17), 3563-3568 (2005).

20. Y. M. Lin and S. C. Yen, Appl Surf Sci **178** (1-4), 116-126 (2001).

21. Y. J. Oh and C. H. Chung, Thin Solid Films **515** (4), 2137-2144 (2006).

22. A. Vaskelis, J. Jaciauskiene, I. Stalnionien and E. Norkus, J Electroanal Chem **600** (1), 6-12 (2007).

23. Y. Y. Shacham-Diamond, Electrochem Solid St **3** (6), 279-282 (2000).

24. R. Jagannathan and M. Krishnan, Ibm J Res Dev **37** (2), 117-123 (1993).

25. N. Kulyk, S. Cherevko and C. H. Chung, Electrochim Acta **59**, 179-185 (2012).

26. Y. Cao and A. C. West, J Electroanal Chem **514** (1-2), 103-108 (2001).

27. T. Osaka and M. Yoshino, Electrochim Acta **53** (2), 271-277 (2007).

28. T. Lim, H.-C. Koo, K. J. Park, M. J. Kim, S.-K. Kim and J. J. Kim, J Electrochem Soc **159** (3), D142-D147 (2012).

29. A. Sargent and O. A. Sadik, J Electrochem Soc **148** (6), C413-C420 (2001).

30. G. Rozovskis, J. Vinkevicius and J. Jaciauskiene, J Adhes Sci Technol **10** (5), 399-406 (1996).

31. L. C. Nagle and J. F. Rohan, Electrochem Solid St **8** (5), C77-C80 (2005).

32. C. Gabrielli, M. Keddam and R. Torresi, J Electrochem Soc **138** (9), 2657-2660 (1991).

33. J. W. Gallaway and A. C. West, J Electrochem Soc **155** (10), D632-D639 (2008).

34. M. Hasegawa, Y. Okinaka, Y. Shacham-Diamand and T. Osaka, Electrochem Solid St **9** (8), C138-C140 (2006).

35. A. E. Martell and R. M. Smith, *Critical stability constants*. (Plenum Press, 1975).

36. Y. Cao, P. C. Searson and A. C. West, J Electrochem Soc **148** (5), C376-C382 (2001).

37. B. Scharifker and G. Hills, Electrochim Acta **28** (7), 879-889 (1983).

38. M. Nagar, P. M. Vereecken, K. Strubbe and A. Radisic, Ecs Transactions **41** (35), 75-82 (2012).

39. Q. Chen, X. Lin, C. Valvede, V. Paneccasio, R. Hurtubise, P. Ye, E. Kudrak and J. Abys, Ecs Transactions **6** (8), 179-184 (2007).

40. U. Emekli and A. C. West, Electrochim Acta **54** (4), 1177-1183 (2009).

41. L. D. Burke and M. M. Murphy, J Electrochem Soc **138** (1), 88-94 (1991).

List of Tables

Table I. Summary of rates of deposition with varying operating conditions and chemistry utilizing both four-point probe method and QCM method.

Four-point Probe	Deposition rate (nm/min)	QCM, 3g/L PEG	Deposition rate (nm/min)
20-90min: pH 8.2, 22°C	9.6	pH 8.20, 50°C	9.8
30-90min: pH 8.2, 35°C	12.6	pH 8.65, 50°C	11.8
5-20min: pH 8.20, 22°C	2.1	pH 8.90, 50°C	16.5
5-20min: pH 8.65, 22°C	4.8	pH 8.65, 20°C	7.0
5-20min: pH 8.90, 22°C	7.1	pH 8.65, 50°C, no PEG	21.8
5-20min: pH 8.20, 22°C, C_{EDTA} * 1.5	1.4	pH 8.65, 50°C, C_{DMAB}*1.5	14.8
5-20min: pH 8.20, 22°C, C_{EDTA} * 0.5	N/A†	pH 8.65, 50°C, C_{CuSO4}*1.5	16.6

†Homogeneous deposition occurred, i.e. plated out

List of Figures

Figure 1

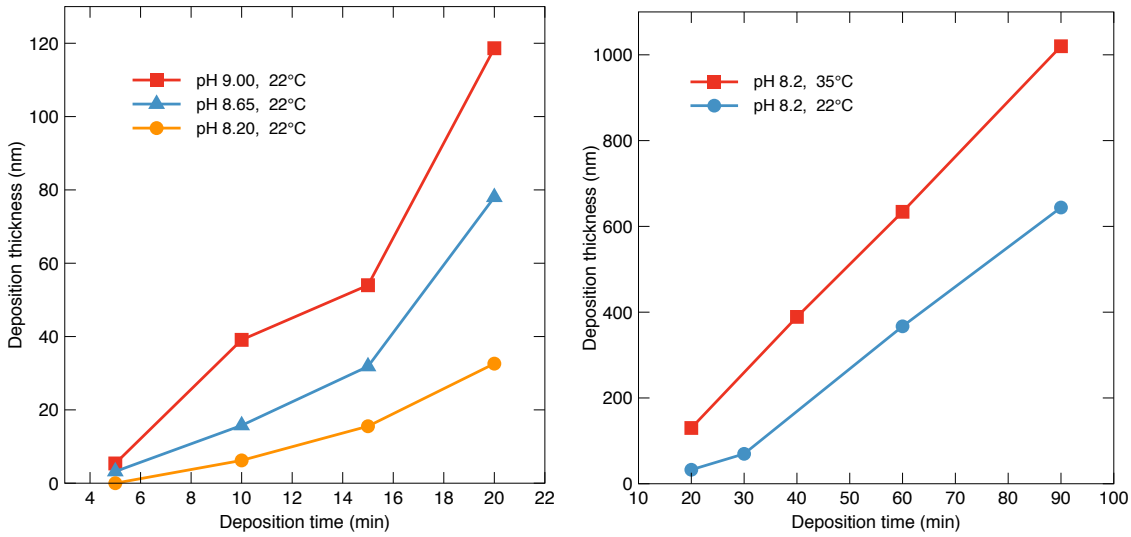

(a) (b)

Figure 1. Discrete ex situ four-point probe measurements: (a) ELD dependence on pH at 22°C during 20min of deposition; (b) ELD dependence on temperature at pH 8.2 during 90min of deposition

Figure 2

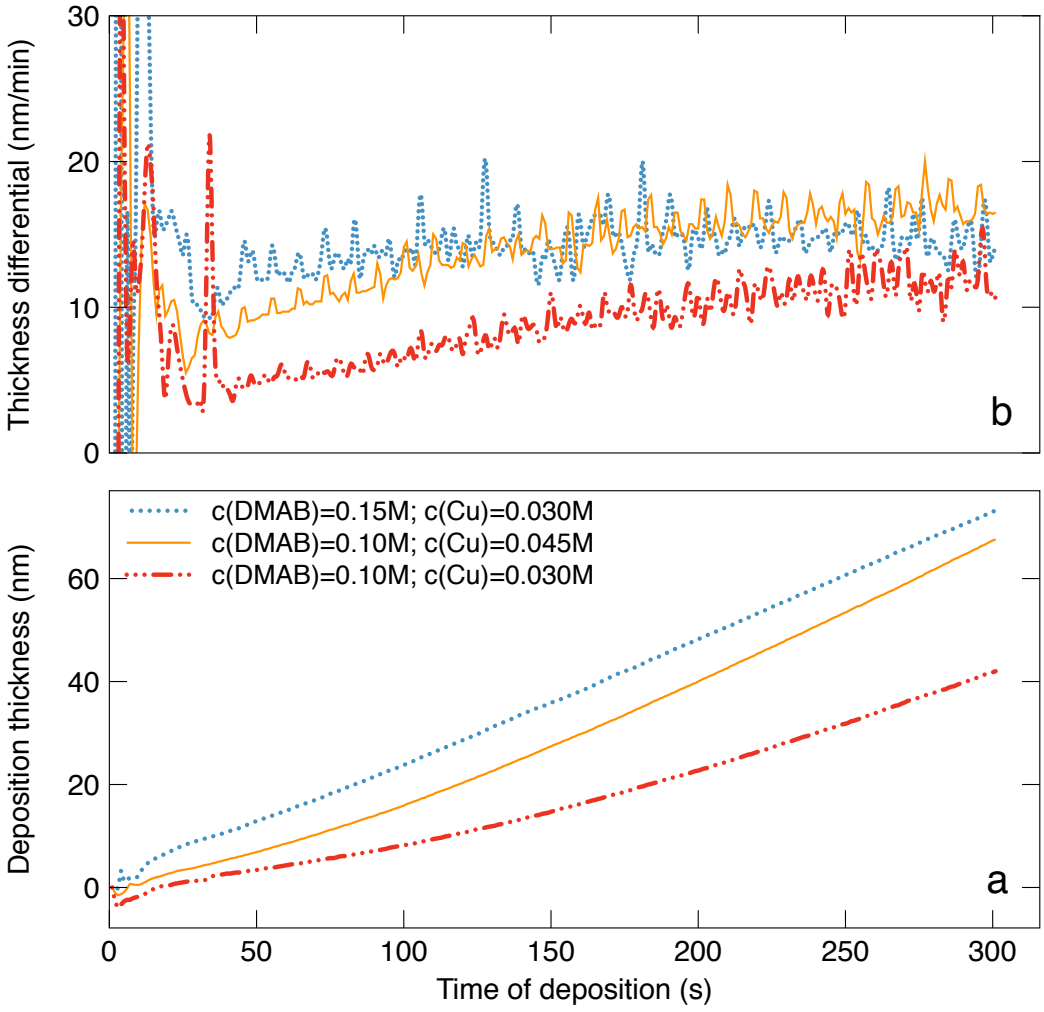

Figure 2. Effect of increased concentration of copper and DMAB. Continuous in situ QCM measurement of Cu ELD under 50°C, pH 8.65; C_{DMAB}=0.1M, C_{Cu}=0.03M is base amount: (a) Deposition thickness change vs. time of deposition; (b) thickness differential vs. time of deposition

Figure 3

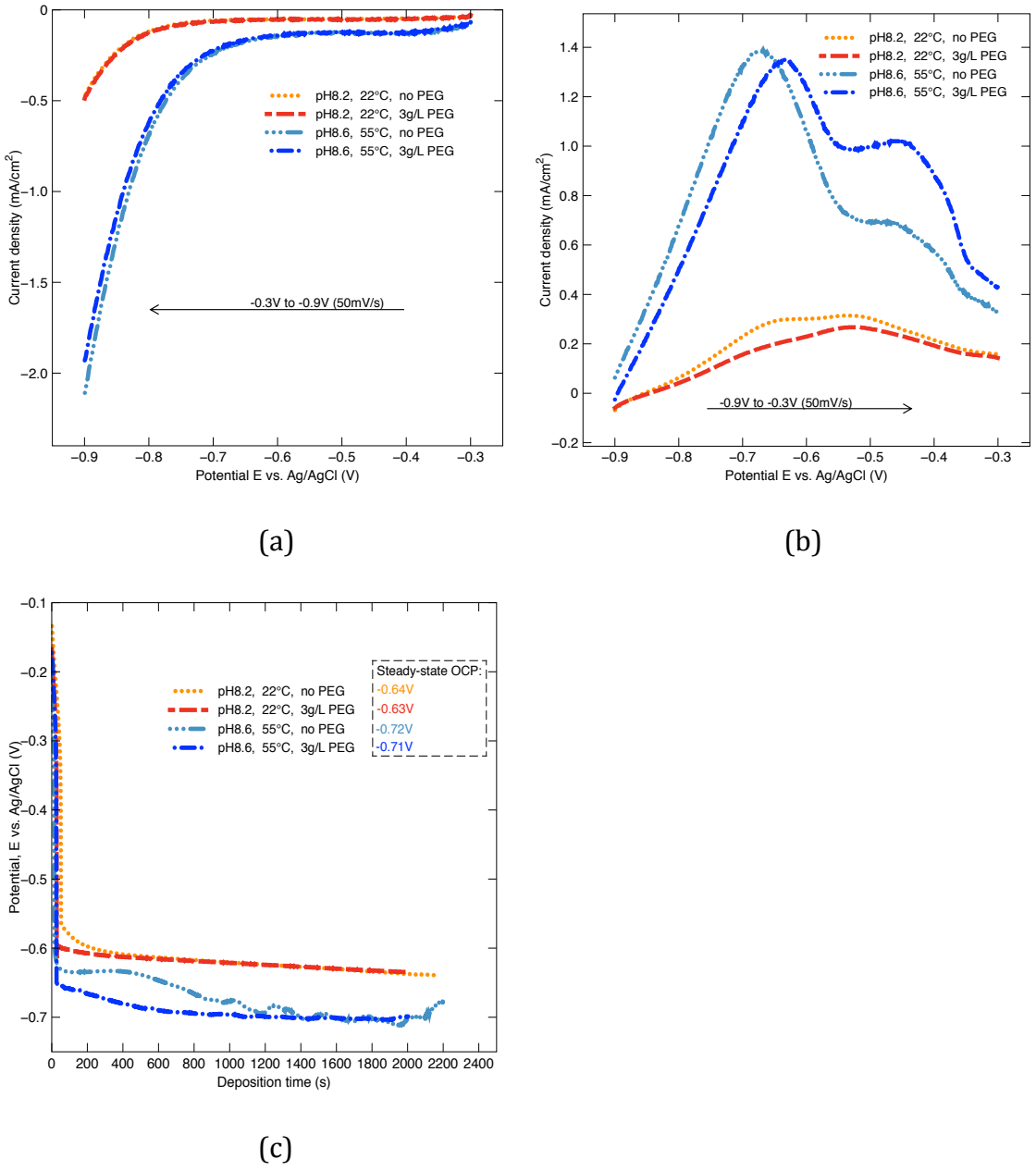

Figure 3. (a) Polarization curves of reduction half-cell (DMAB eliminated); (b) Polarization curves of oxidation half-cell ($CuSO_4$ eliminated); (c) OCPs of complete baths

Figure 4

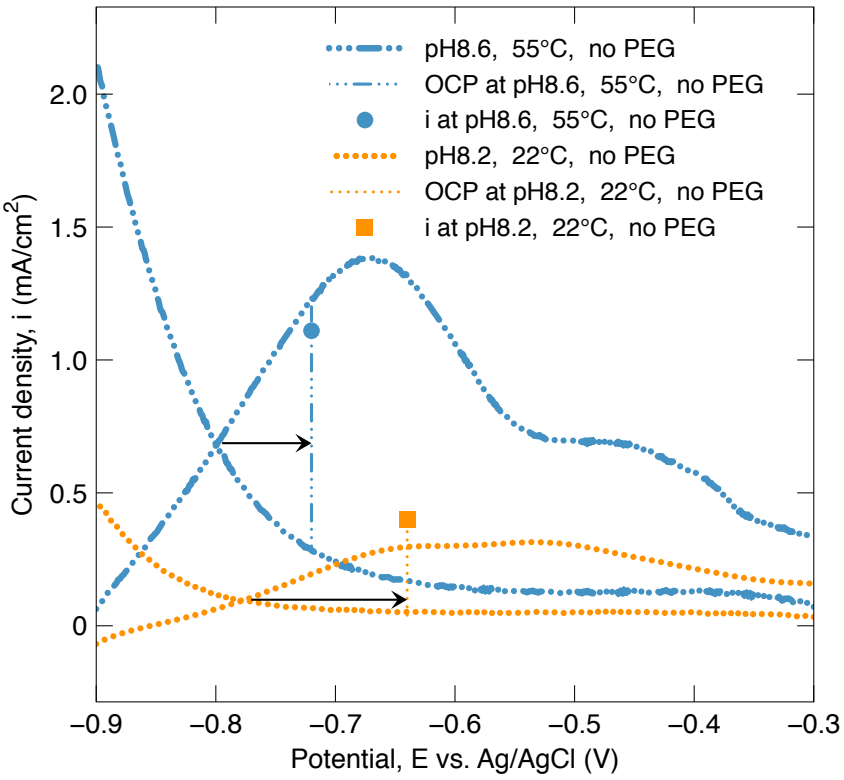

Figure 4. Mixed potential theory interpretation by summarizing oxidation and reduction polarization curves, the measured OCPs and current densities calculated from QCM measurements, under two cases without PEG

Figure 5

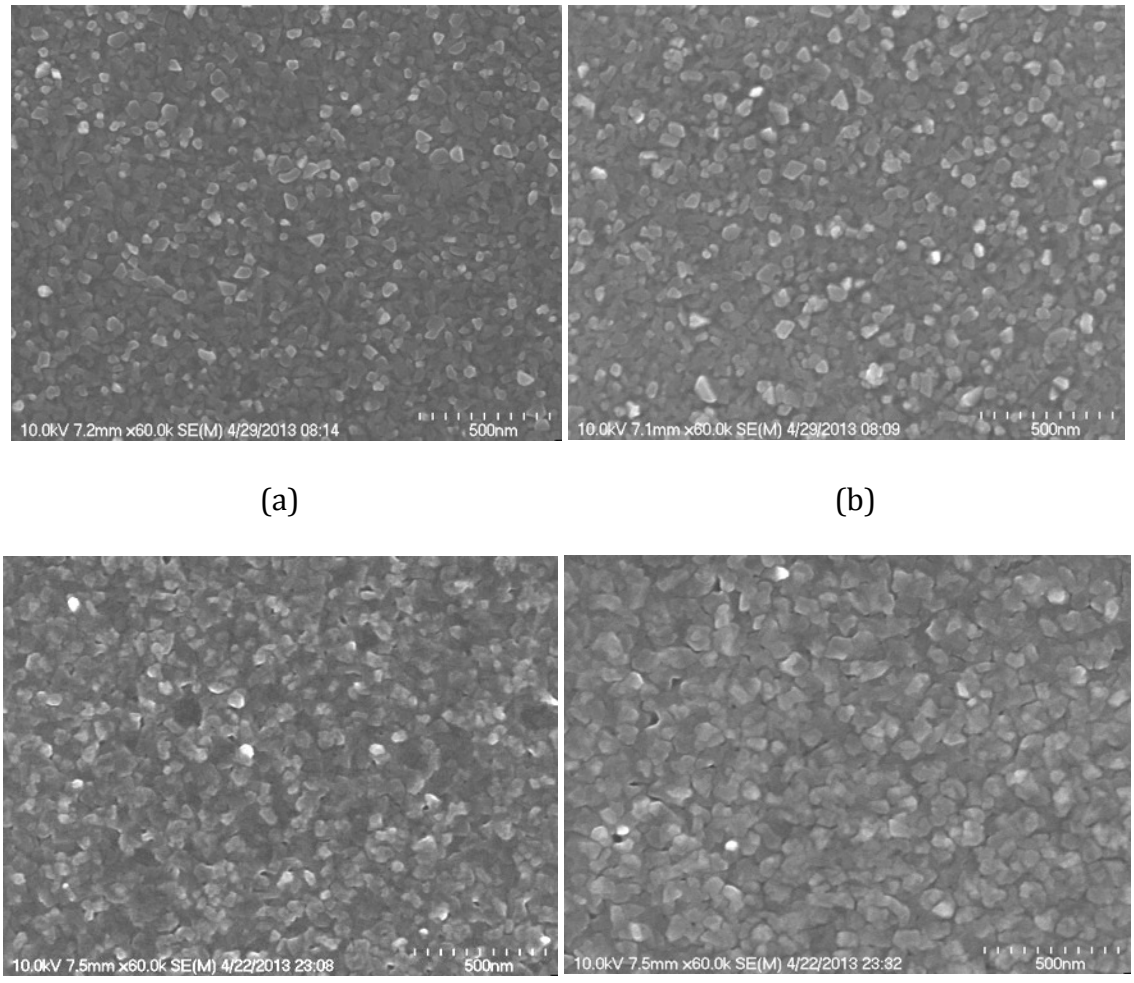

Figure 5. Exemplary time-wise SEM observation of Cu ELD on PVD Cu wafer coupon under pH 8.9, 55°C, no PEG. (a) 10s ELD; (b) 15s ELD; (c) 30s ELD; (d) 60s ELD

Figure 6

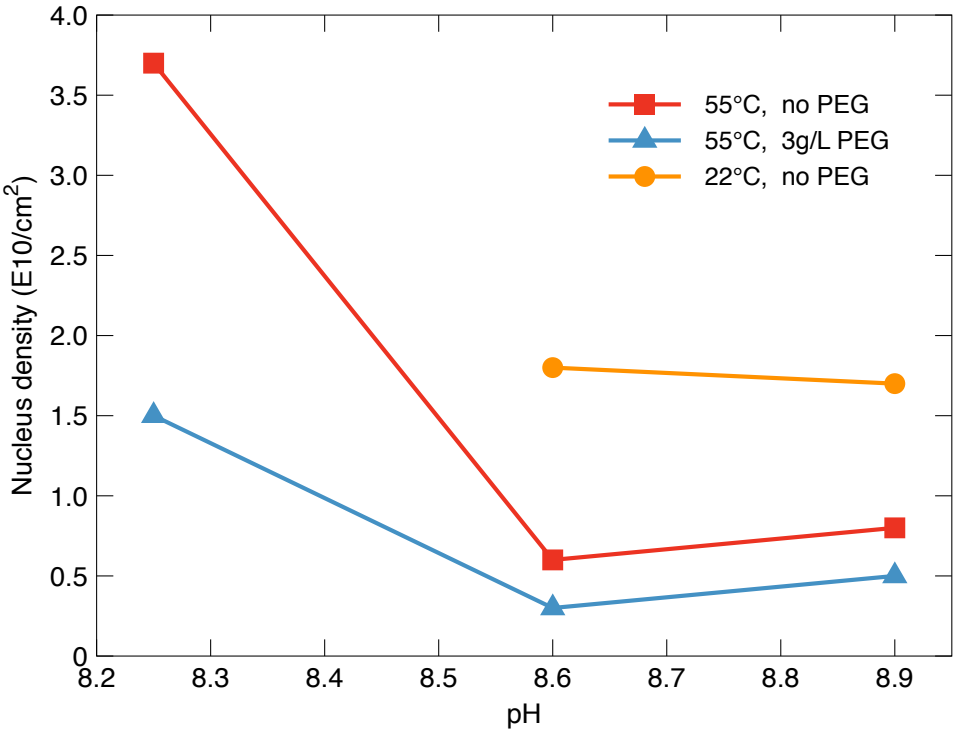

Figure 6. Summary of nucleus density with respect to pH, temperature and addition of PEG, deposition thickness ranges from 4nm to 10nm depending on the clearness of nuclei displayed on SEM images to optimize accuracy

Figure 7

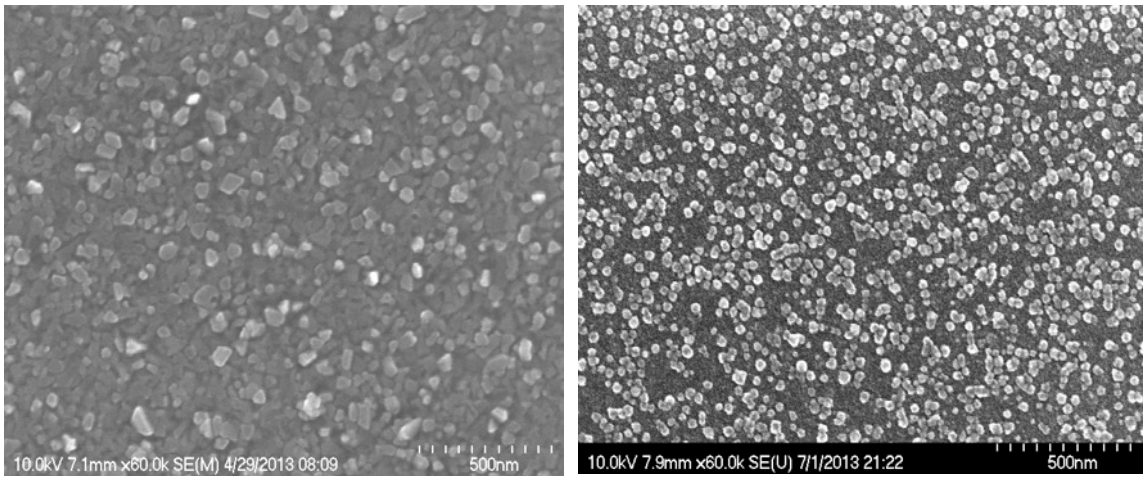

(a) (b)

Figure 7. Comparison of copper nucleation on: (a) PVD Cu plated wafer coupon; (b) Ruthenium plated wafer coupon

Figure 8

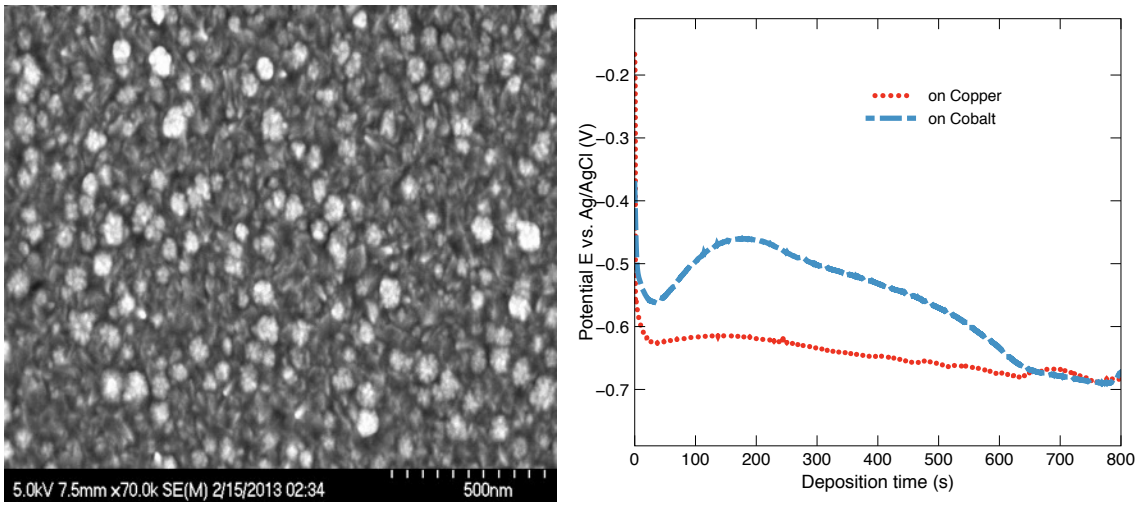

(a) (b)

Figure 8. (a) SEM picture of copper nucleation on cobalt substrate; (b) Open circuit potential of electroless copper deposition on copper and cobalt respectively, both under static condition on pre-plated rotating disk electrode

Figure 9

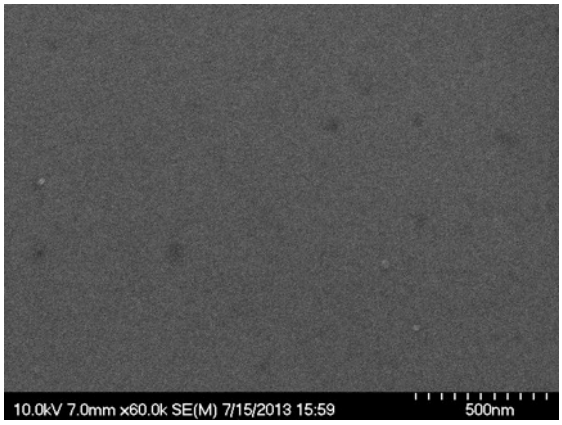

(a)

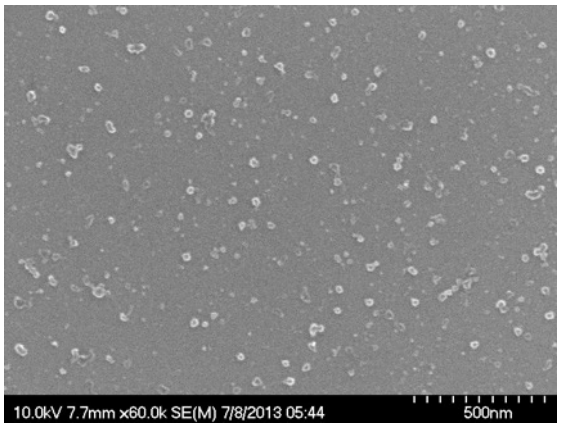

(b)

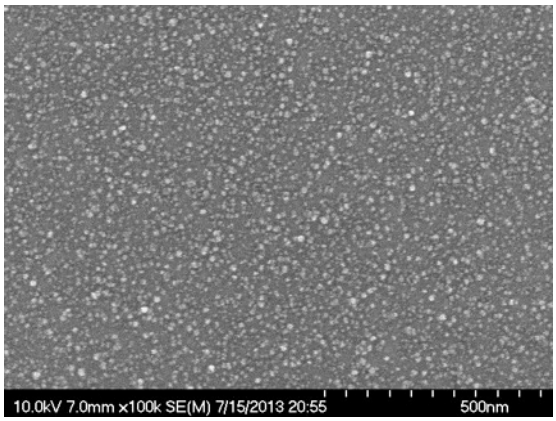

(c)

Figure 9. Step-wise observation of copper metallization on silicon oxide with SAM and Palladium activation. (a) After cleaning with methanol; (b) After Pd activation; (c) Copper nucleation

Chapter 3:

Design of Lab-scale Apparatus for Aging Studies of Copper Electrodeposition Additives

Abstract

A lab-scale additive aging device was developed as a tool for copper electrodeposition technologies. A cation exchange membrane separated the cathode and anode compartments to differentiate the aging effect. The anolyte chemistry was modified to ensure more uniform catholyte composition without the need of extra monitoring and replenishment. A cyclic voltammetric stripping (CVS) method was utilized to quantify the concentration of bis (3-sulfopropyl) disulfide (SPS). Aging studies were performed on the cathode side and significant degradation of SPS was observed. The aging process was determined to be diffusion controlled by comparing the rate of aging with calculated maximum mass transfer rate of SPS to rotating cylinder electrode. It was also found that higher acid level and lower current density accelerated the SPS aging process by the cathode, while the addition of PEG lowered the rate of SPS aging.

Introduction

Organic additives are extensively utilized in copper electrodeposition for interconnect technology to achieve various deposit properties.[1-5] A combination of suppressor and accelerator has been employed in the industry to facilitate "bottom-up" feature filling. Suppressors are typically polymers containing ethylene or propylene glycol such as polyethylene glycol (PEG), which suppress copper deposition.[6-10] Accelerators typically contain mercapto/disulfide and sulfonate groups such as bis (3-sulfopropyl) disulfide (SPS) and 3-mercapto-1-propane sulfonic acid (MPSA). They accelerate deposition through either competitive adsorption with suppressors or catalytic reduction of Cu^{2+} by oxidation of MPSA to SPS. [1, 2, 11-16]

The presence of an appropriate amount of accelerator in the solution is critical in filling small features without voids or other defects. However, SPS decomposes during the electrodeposition process through complex interactions involving copper, Cu^{+}, Cu^{2+}, thiol/disulfide, oxygen and related products.[16-19] From a practical perspective, the aging SPS may significantly complicate process control. Significant emphasis of aging studies has been carried out on additive interactions with the anode, either ascribing to a high anodic potential that oxidizes SPS on insoluble anodes, or the generation of cuprous ion that oxidizes SPS with dissolved oxygen on copper anodes.[16, 20, 21] Some studies evaluated SPS aging in a non-separated complete bath, while little attention has been paid on SPS aging on cathodes.

In this study, a cell to study additive aging with membrane-separated anolyte and catholyte compartments has been developed and used. A modified CVS technique is employed to quantify SPS concentrations throughout aging process. The anolyte chemistry is modified to reduce or eliminate the need for catholyte replenishment of cupric ions or pH values. The aging of SPS was characterized at varied acid levels, current densities and the presence/absence of PEG.

Experiments and Methods

The base catholyte consisted of 0.3 M cupric sulfate ($CuSO_4$), 0.8 M sulfuric acid (H_2SO_4), 300 ppm polyethylene glycol (PEG), 1.4 mM hydrochloric acid (HCl), and 30 ppm SPS. The base anolyte contained all the base catholyte but sulfuric acid. CVS was performed in the range between -0.225 V and 1.575 V vs. Ag/AgCl reference electrode (Basi) at 100 mV/s for 2 cycles, with the peak area integrated from 0.0972 V to 0.6725 V. The working electrode (WE) was a platinum rotating disk electrode (Pine Research Instrumentation) of 0.5 mm in diameter, operated at 900 rpm. A silver-silver chloride (Ag/AgCl) reference electrode (RE) was used to reference the potential of working electrode. The counter electrode (CE) was a platinum wire. Prior to CVS measurement, the electrode was preconditioned in SPS-free acid copper solutions with the same CVS scan pattern. An EcoChemie type III μ Autolab potentiostat was used to supply controlled potential and monitor current response.

In the cathode aging experiments, each catholyte and anolyte compartment contained 167 mL of solution. The rotating cylinder cathode had a surface area of

16.7 cm^2, equal to that of the rectangular copper anode sheet. The cathode was rotated at 900 rpm with no additional agitation in the catholyte. Both cathode and anode were placed 2 cm from the membrane. The electrolyte behavior was monitored as a function of total charge passed (ampere-hour) per liter (Ah/L) as this is the most common metric to characterize bath life. 1 mL of solution from each compartment was sampled for measurement of SPS concentration along different time intervals.

Design of Aging Device and Analysis Routine

Quantifying SPS concentration with optimized CVS method

The CVS method is a widely used method to quantify organic additives in copper electroplating baths because of its simplicity and high sensitivity.[22-24] The CVS was performed in a tapered reactor as shown in the insert of Figure 1. The wider opening of the reactor accommodates all three electrodes to be adequately immersed in the solution, while the small bottom minimizes the solution needed. Through this study, all CVS measurements were performed with 10 mL of solution. Figure 1 shows exemplary CVS scans of increasing SPS concentration from 0ppm to 5 ppm, with increased stripping peak height and peak area. The stripping peak area is an indicator of the rate of deposition, and thus the acceleration effects from SPS.

Usually the CVS is scanned for 10 cycles and analysis is performed on the last cycle. However, we determined that 2 cycles is preferred in our case since SPS also ages during the CVS scan and thus reduces the peak area for calibration at such low

SPS detection level. Furthermore, with 2 cycles of preconditioning without SPS, we found the CVS analysis performed on the 2nd cycle very reproducible.

In a normal plating chemistry, 30 ppm of SPS is a typical concentration. We performed CVS on a wider range up to 120 ppm as shown in Figure 2. The peak area of CVS increased with an increasing amount of added SPS in the solution from 0 ppm up to about 20 ppm, while additional SPS did not further increase the deposition rate. A range from 0 to 3 ppm was determined as our calibration range as shown in the insert of Figure 2. From 0 to 3 ppm, the CVS peak area and SPS concentration showed great linearity. Moreover, diluting from up to 30 ppm of SPS, only 1 mL of sample solution is needed to make a 10 mL test solution.

Designs of Aging device

We designed several iterations of aging devices, with two illustrative concepts shown in Figure 3 and Figure 4. (Courtesy of Feng Qiao, who fabricated the membrane separated cells and made the CAD drawings) The first concept shown in Figure 3a is a self-contained anolyte compartment of 110 mL completely immersed in a much larger catholyte compartment of 800 mL, separated only by the cation exchange membrane screwed to the gasket to the top of the anolyte compartment. The major advantage of this design is that the anolyte compartment is separated from the catholyte compartment so that the aging device can easily be adopted in existing electroplating system in beaker scale. However, this design was challenged by the long-term sealing of the screw and gasket system. Leakage, especially undetected leakage, can easily distort the experimental results due to the

interference from one compartment to another. More importantly, since the anode needs to be supplied from a thin tube down to the anolyte compartment, it has to be connected as a wire. Once the aging time is long, the copper wire thins down and breaks from middle, leading to open circuit failure. Even though non-dissolving metal could be connected to a copper anode, it was difficult to replace the anodes and clean the anolyte compartment with the screw and gasket design. Last but not least, when the membrane was horizontally facing the cathode, bubbles tend to float up and accumulate below the membrane, affecting the transport properties.

Figure 2b shows the current design used in the aging studies. The catholyte and anolyte compartments were of exact same cuboid shape and size. One sidewall of each compartment had a square opening for membrane. The sidewalls with openings, together with the membrane, are glued together permanently with silicon glue and sealant. A rotating cylinder electrode instead of rotating disk electrode was utilized in the setup for better uniformity of current density. The permanently glued setup was much more leak proof in the long run. Furthermore, the equal size of both compartments allowed for the study of both aging of SPS on anode and cathode at the same time. Furthermore, the setup is very easy to use in implementation. The wide opening on the top allows for easy sampling, cleaning and poses little limitation on the dimensions of the anode.

Engineering anolyte chemistry to compensate for the lack of selectivity of membrane

In unseparated electroplating cells, ions diffuse freely throughout the reactor. The cupric ions generated on the copper anodes constantly flow towards cathodes, where cupric ions are consumed at the same rate, so that cupric concentration remained constant in time. In a separated cell, it may be more difficult to achieve equal concentration in the catholyte without a cupric-ion selective membrane. However, there is no known membrane that allows cupric-ion transport with zero proton flux. As a matter of fact, hydrogen always diffuses more quickly through the membrane. In most of the test solutions, the concentration of sulfuric acid is 0.8 M, compared with cupric sulfate of only 0.3 M. The much higher concentration of hydrogen ions further promotes the preferential diffusion of hydrogen ion from anolyte to the catholyte when an external electrical field is applied. In aging experiments that use the same anolyte and catholyte compositions, the cupric ions were depleted in the catholyte, while increased in concentration in the anolyte. As importantly, the acid level significantly increased in the catholyte, leaving the anolyte acid-deprived. The acid level change affects the rate of additive aging as shown in the results section. Although replenishment system could be possibly performed to replenish/deplete cupric ion and neutralize the acid level variation, it apparently adds many folds of complexity to the aging system.

To reduce cupric ion and acid level variations in the catholyte, without using a complex monitoring and replenishment system, the anolyte composition was modified to favor cupric-ion transport across the membrane. Similarly, the study of aging on the anode side could be possibly done, by eliminating the cupric ion and

increasing the acid level on the catholyte side while keeping the desired chemistry for the anolyte.

Results and Discussions

As shown in Figure 5, we performed SPS aging experiments in both high acid and low acid chemistry for 3.75 hours at 40 mA/cm^2, equivalent to 15 Ah/L. Starting from about 30 ppm of SPS, in the high acid bath, the apparent SPS concentration decreases to 15 ppm after 15 Ah/L of aging. The rate of aging is roughly 1 ppm per Ah/L. In the low acid bath however, the rate of aging was only 0.5 ppm per Ah/L. The relatively higher rate of aging in the bath containing higher acid level might suggest the positive participation of hydrogen ion in the breakdown of SPS.

On the other hand, 15 Ah/L of aging was also performed at 20 mA/cm^2 in 7.5 hours. The apparent SPS concentration is 9 ppm, yielding a rate of about 1.8 ppm per Ah/L. Interestingly, the slower deposition rate aged SPS more rapidly. At 30 ppm, the concentration of SPS is less than 100 uM.

Under such low concentration, mass-transfer process may play an important role. On rotating cylinder electrode, the mass-transfer-limited current could be characterized by Eisenberg equation,[25, 26] and the mass-transfer-limited rate of consumption can be calculated as:

$$N_L = 0.0791 \cdot A \cdot d_{cyl}^{-0.3} \cdot D_{sps}^{+0.644} \cdot \upsilon^{-0.344} \cdot U_{cyl}^{+0.7} \cdot C_{sps} \quad (1)$$

The calculated N_L is 6.9×10^{-10} mol/s, equivalent to 1.28 ppb/s and 4.6 ppm/h with the catholyte volume of 167 mL. The parameters used in calculating N_L are as

follows: A (cathode's surface area) is 16.7 cm^2, d_{cyl} (diameter of cathode) is 1.2 cm, D_{sps} (diffusion coefficient of SPS) of 1×10^{-6} cm^2/s is used same as previous literature,[27] υ (kinematic viscosity) is roughly 1×10^{-2} cm^2/s at room temperature with water as the solvent, U_{cyl} (linear surface velocity) is 56.5 cm/s based on 900 rpm, C_{sps} (bulk concentration of SPS) is 9.68×10^{-8} mol/cm^3 as calculated from 30 ppm with SPS molecular weight of 310.

Evidently, with a maximum mass transfer limited rate of consumption of 4.6 ppm per hour, the aging process can be influenced by mass transfer at 40 mA/cm^2, where SPS aged at 4 ppm/h in high acid solution. The mass transfer is less important for low acids where an aging rate of 2 ppm/h was measured. For a high acid bath at 20 mA/cm^2, SPS aged at 2.8 ppm/h.

The result that a longer deposition time led to more SPS aging also raises the question of whether the exposure of SPS to a copper surface itself would significantly age SPS, as has been also suggested in the literature.[28] In order to compensate for this loss, we passed zero current and measured the SPS concentration over a long period of time as shown in Figure 6. Clearly, over 38 hours, SPS aged in a very slow manner of only 0.08 ppm per hour, which is too little to explain the large difference between the 20 mA/cm^2 and 40 mA/cm^2 scenarios. Hence the faster aging rate with lower deposition rate is not a result of the longer immersion time.

For the three scenarios, we also measured the pH before and after aging for both compartments as shown in Table 1. For both high acid cases, the catholyte pH before and after was not changed at 0.2 with little to no variation in the anolyte pH

around 3. A similar pattern was also observed in the low acid case. This suggests that little acid transport between the two compartments occurred and cupric ion have been the major cation transferred from anolyte to catholyte.

Another interesting direction of studying the rate of SPS aging would be the presence and absence of suppressor, like PEG. We performed no-PEG scenario to compare with normal scenario and showed the results in Figure 7. The rate of SPS aging without PEG was roughly 30% higher than that with PEG.

Conclusions

In this study, a novel additive aging cell for copper electrodeposition process is presented. A modified anolyte chemistry for cathode SPS aging was proposed to overcome the limitation of membrane selectivity, which leads to significant acid level and copper content variation during aging process. A CVS method successfully quantified SPS concentration in copper plating bath. Results showed that SPS aging on cathodes is significant. The rate of aging as a function of charge passed is higher at lower current density and higher acid level. Also, the addition of PEG reduces the rate of SPS aging. Through characterization of mass transfer of SPS on rotating cylinder electrode, it was found that the aging process under current operating conditions may be diffusion controlled. By monitoring the pH change of the membrane-separated compartments before and after aging experiments, the effectiveness and practicality of using modified anolyte chemistry in achieving desired transport properties was validated.

ACKNOWLEDGMENTS

This research was supported by Atotech, USA. The authors gratefully acknowledge Feng Qiao of Columbia University for his work in fabricating aging devices.

Reference

1. T. P. Moffat, J. E. Bonevich, W. H. Huber, A. Stanishevsky, D. R. Kelly, G. R. Stafford and D. Josell, J Electrochem Soc **147** (12), 4524-4535 (2000).

2. T. P. Moffat, D. Wheeler and D. Josell J Electrochem Soc **151** (4), C262-C271 (2004).

3. J. W. Gallaway, M. J. Willey and A. C. West, J Electrochem Soc **156** (4), D146-D154 (2009).

4. T. P. Moffat and D. Josell, J Electrochem Soc **159** (4), D208-D216 (2012).

5. D. Josell, D. Wheeler and T. P. Moffat, J Electrochem Soc **159** (10), D570-D576 (2012).

6. J. W. Gallaway and A. C. West, J Electrochem Soc **155** (10), D632-D639 (2008).

7. J. W. Gallaway, M. J. Willey and A. C. West, J Electrochem Soc **156** (8), D287-D295 (2009).

8. M. E. Huerta Garrido and M. D. Pritzker, J Electrochem Soc **155** (4), D332-D339 (2008).

9. M. L. Walker, L. J. Richter and T. P. Moffat, J Electrochem Soc **152** (6), C403-C407 (2005).

10. K. R. Hebert, S. Adhikari and J. E. Houser, J Electrochem Soc **152** (5), C324-C329 (2005).

11. T. P. Moffat, D. Wheeler, S.-K. Kim and D. Josell, J Electrochem Soc **153** (2), C127-C132 (2006).

12. N. T. M. Hai, K. W. Krämer, A. Fluegel, M. Arnold, D. Mayer and P. Broekmann, Electrochim Acta **83** (0), 367-375 (2012).

13. N. T. M. Hai, T. T. M. Huynh, A. Fluegel, M. Arnold, D. Mayer, W. Reckien, T. Bredow and P. Broekmann, Electrochim Acta **70** (0), 286-295 (2012).

14. J. J. Kim, S.-K. Kim and Y. S. Kim, J Electroanal Chem **542** (0), 61-66 (2003).

15. A. Frank and A. J. Bard, J Electrochem Soc **150** (4), C244-C250 (2003).

16. T. P. Moffat, B. Baker, D. Wheeler and D. Josell, Electrochem Solid St **6** (4), C59-C62 (2003).

17. J. P. Healy, D. Pletcher and M. Goodenough, J Electroanal Chem **338** (1–2), 179-187 (1992).

18. W. O. Freitag, C. Ogden, D. Tench and J. White, Plat Surf Finish **70** (10), 55-60 (1983).

19. N. A. Zhukauskaite, A. Y. Lazauskene and A. A. Malinauskas, Prot Met+ **25** (2), 244-248 (1989).

20. S.-K. Kim and J. J. Kim, Electrochemical and Solid-State Letters **7** (9), C98-C100 (2004).

21. C. Gabrielli, P. Mocoteguy, H. Perrot, A. Zdunek and D. Nieto-Sanz, J Electrochem Soc **154** (3), D163-D169 (2007).

22. R. Haak, C. Ogden and D. Tench, Plat Surf Finish **68** (4), 52-55 (1981).

23. R. Haak, C. Ogden and D. Tench, Plat Surf Finish **69** (3), 62-66 (1982).

24. L. T. Koh, G. Z. You, C. Y. Li and P. D. Foo, Microelectronics Journal **33** (3), 229-234 (2002).

25. M. Eisenberg, C. W. Tobias and C. R. Wilke, J Electrochem Soc **101** (6), 306-320 (1954).

26. D. R. Gabe and F. C. Walsh, Journal of Applied Electrochemistry **13** (1), 3-21 (1983).

27. Y. Cao, P. Taephaisitphongse, R. Chalupa and A. C. West, J Electrochem Soc **148** (7), C466-C472 (2001).

28. C. C. Hung, W. H. Lee, S. Y. Hu, S. C. Chang, K. W. Chen and Y. L. Wang, J Electrochem Soc **155** (5), H329-H333 (2008).

List of Tables

Table I. pH variations in catholyte compartment and anolyte compartment before and after aging in three scenarios

	Catholyte pH before	Catholyte pH after	Anolyte pH before	Anolyte pH after	Catholyte aging rate ppm/(Ah/L)
80 g/L H_2SO_4 40 mA/cm^2	0.2	0.2	3.2	3.1	1.0
30 g/L H_2SO_4 40 mA/cm^2	0.8	0.8	3.0	2.9	0.5
80 g/L H_2SO_4 20 mA/cm^2	0.2	0.2	3.0	2.6	1.8

List of Figures

Figure 1

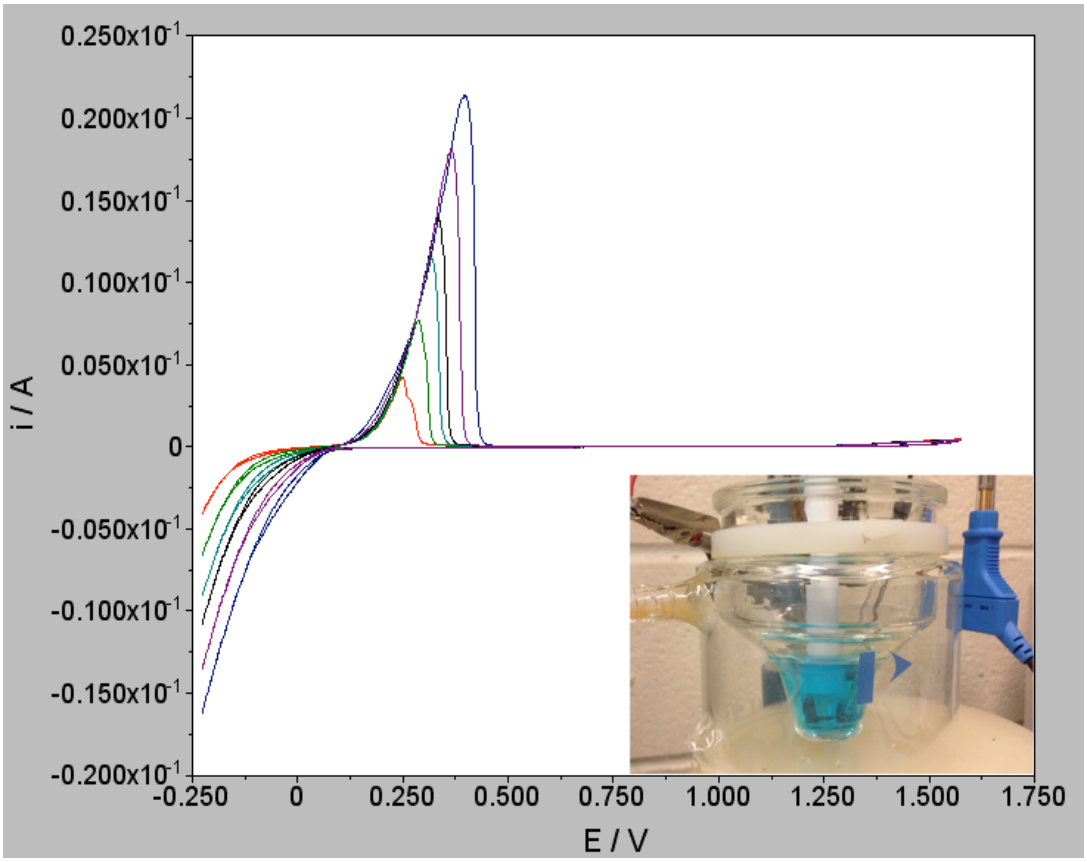

Figure 1. CVS scan with various SPS concentration added to the acid copper solution. (Red) 0 ppm; (green) 1 ppm; (light blue) 2 ppm; (black) 3 ppm; (purple) 4 ppm; (blue) 5 ppm; (insert) the tapered CVS reactor with all three electrodes immersed

Figure 2

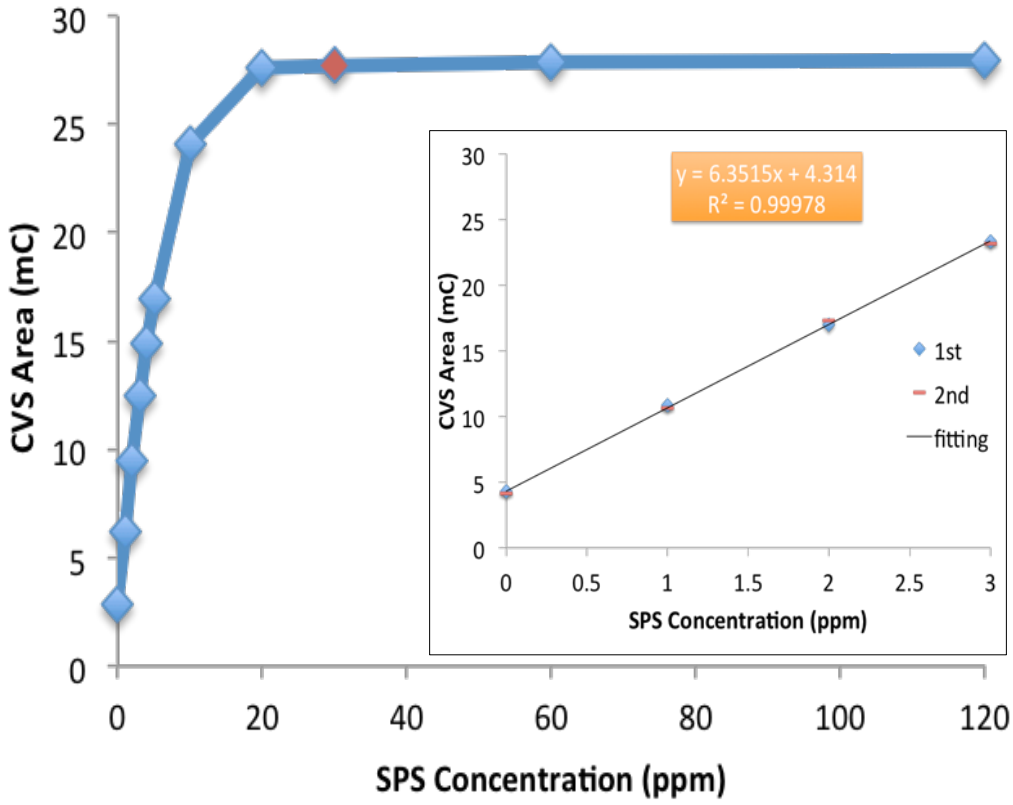

Figure 2. CVS peak area performed under various SPS concentration from 0 ppm up to 120 ppm. (insert) calibration curve of CVS peak area versus SPS concentration over the range of 3 ppm

Figure 3

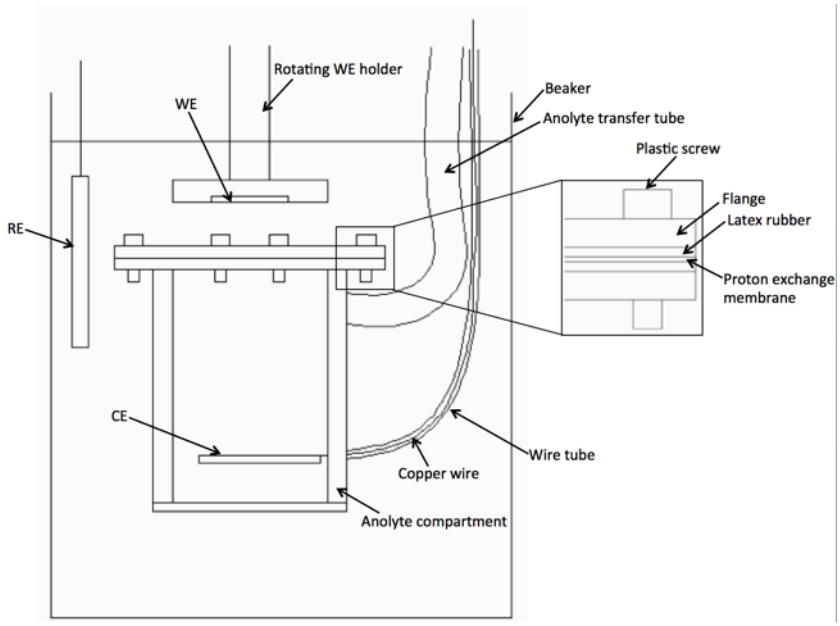

(a)

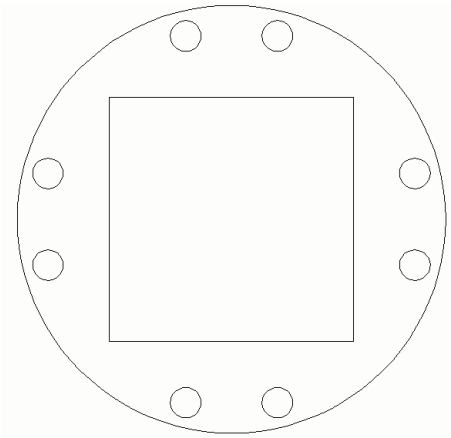

(b)

Figure 3. Exemplary design of a previous aging device. (a) side view of the whole apparatus; (b)top-down view of the flange cover with screw tightened gasket (Drawing courtesy of Feng Qiao)

Figure 4

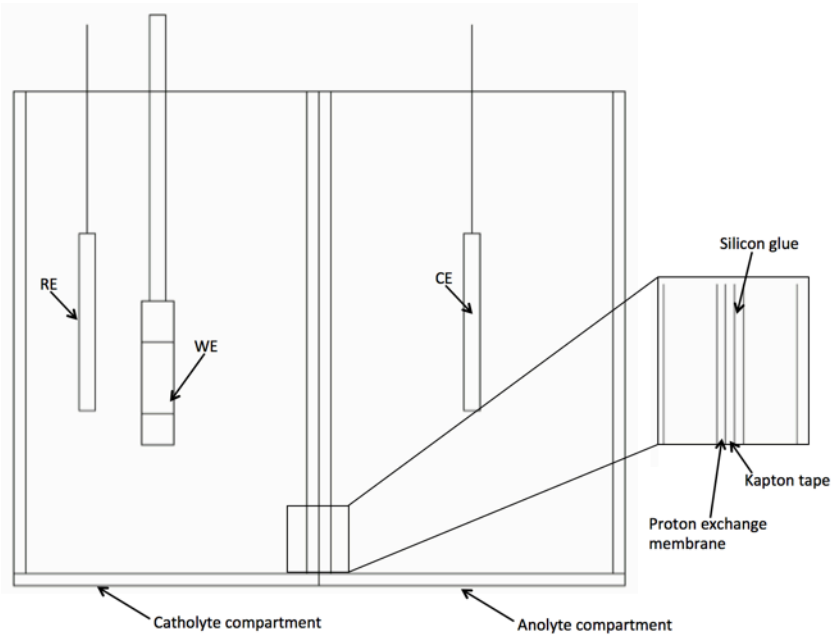

(a)

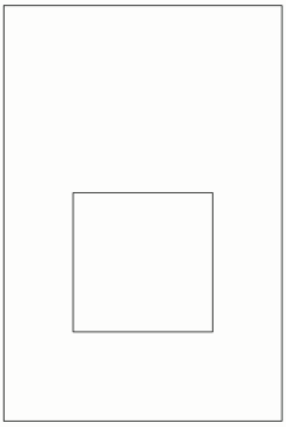

(a)

Figure 4. Design of the aging device utilized within this study. (a) side view of the whole apparatus; (b) top-down view of the flange cover. (Drawing courtesy of Feng Qiao)

Figure 5

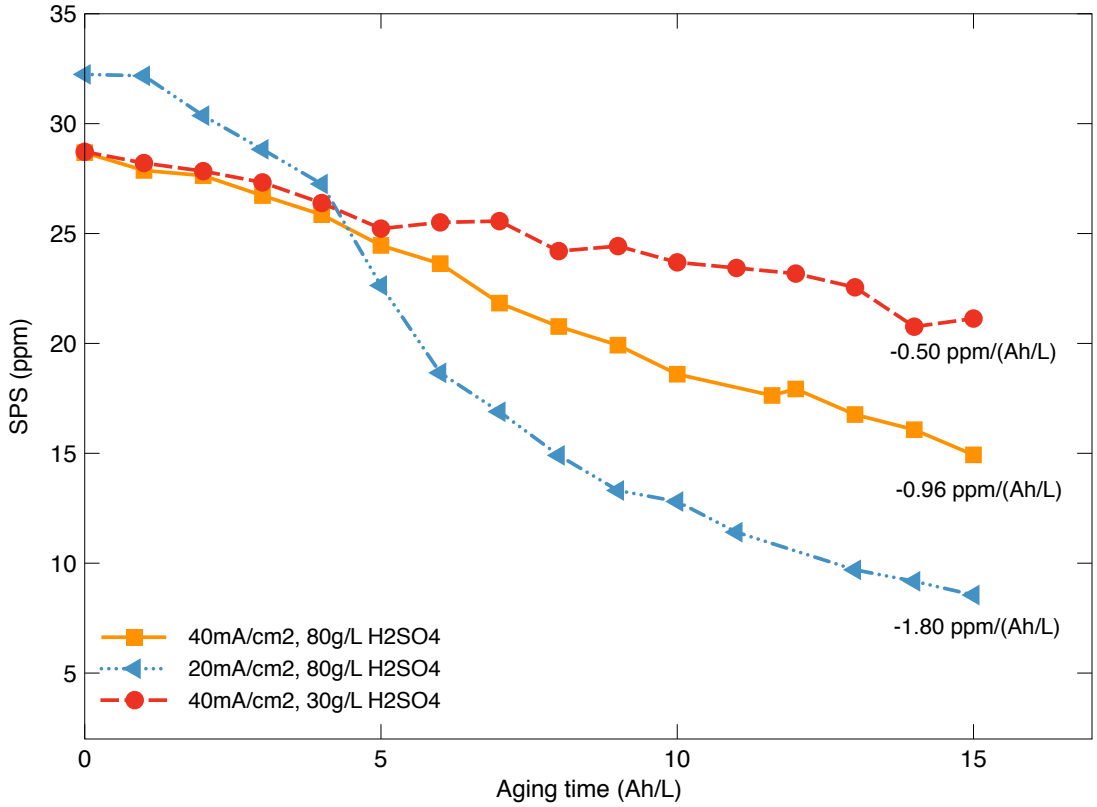

Figure 5. SPS concentration variation over 15 Ah/L of aging time under three operational conditions as shown in the legend.

Figure 6

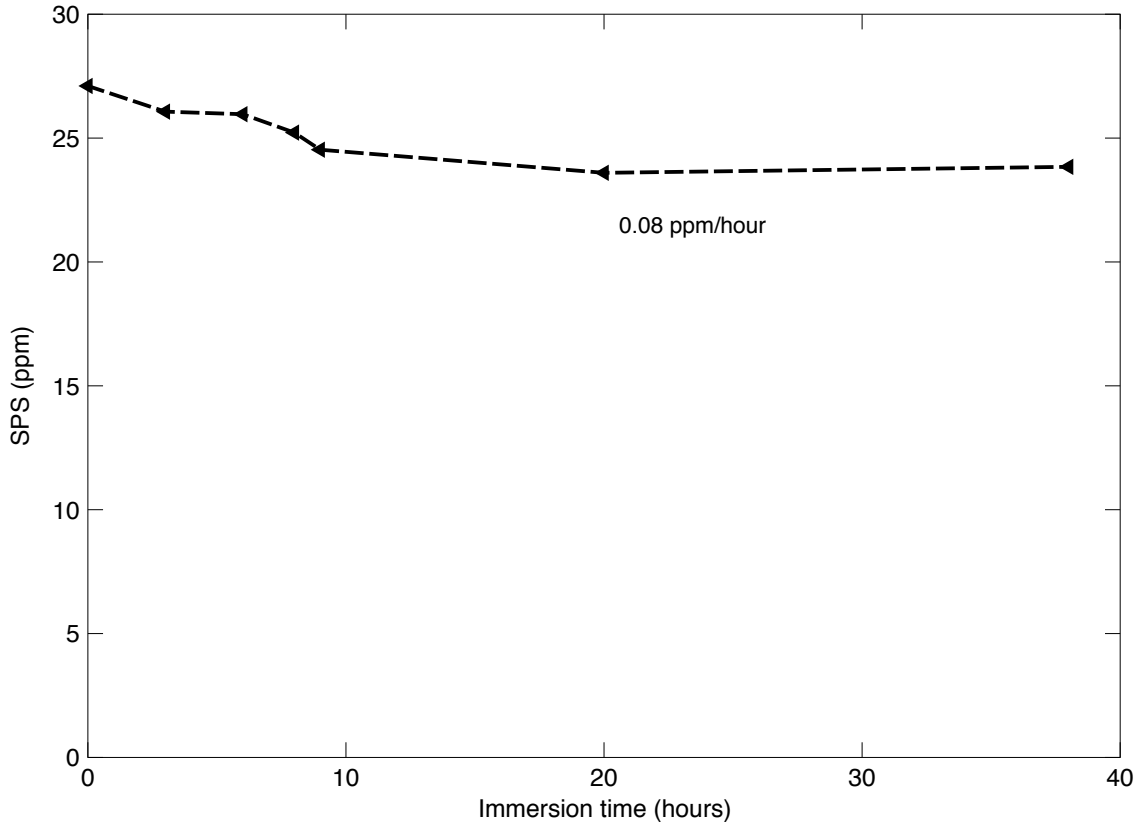

Figure 6. SPS concentration variation over 38 hours of "zero-current-aging" in typical high acid copper solution. All other constituents and electrode configuration remained same with normal aging experiments

Figure 7

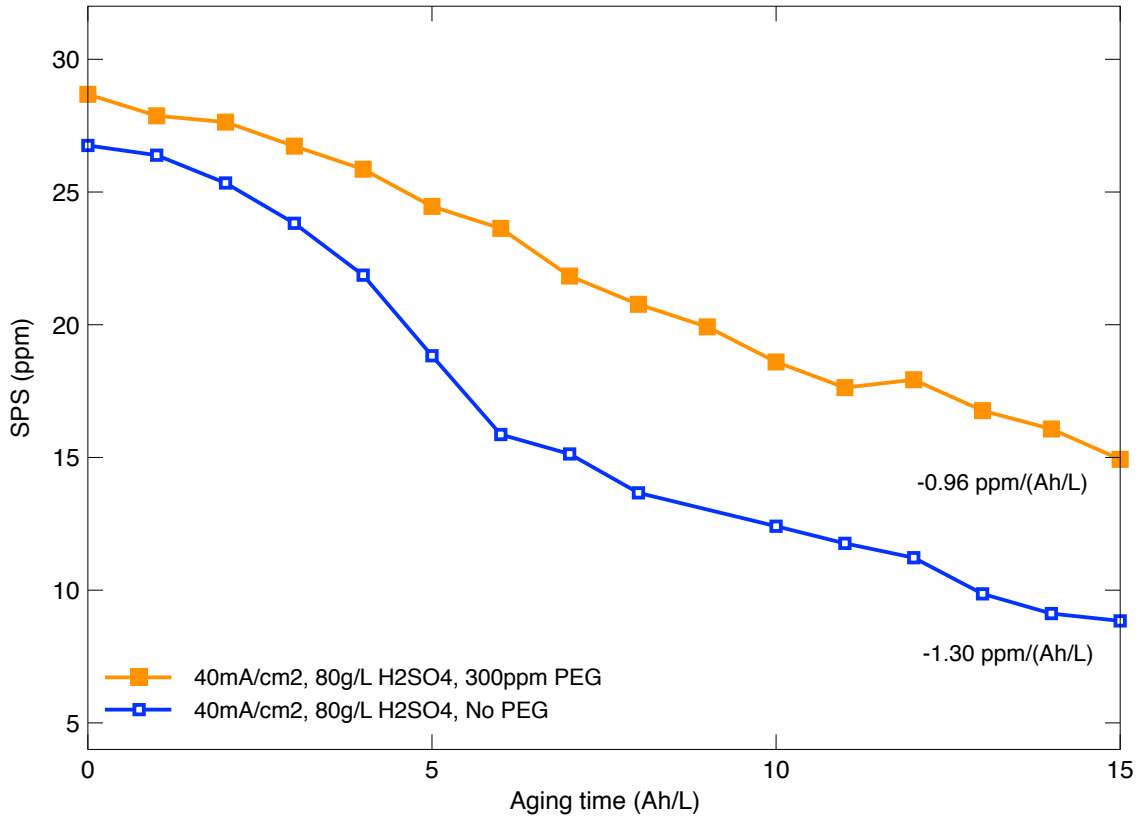

Figure 7. Comparison of SPS aging over 15 Ah/L between with and without PEG addition scenarios

Chapter 4:

Design of Laboratory Electrodes for Electrolytic Copper Deposition with Improved Current Distribution

Abstract

Thoroughly designed and optimized wafer plating tools have long existed in the industry to guarantee a high uniformity of copper electrodeposition. However, this type of tools is not easily "scaled down" to a laboratory beaker scale due to their complexities, which often leaves poor current distribution over the substrates. In this chapter we present a simple insulating shield system that significantly improves the current distribution over rotating disk setup while at the same time very easily made and integrated. Systematic numerical simulation analysis is performed to evaluate the influence of the shape and position of the shield on the current distribution uniformity. Through optimization with the determined parameter sensitivities for a coupon-size system, we were able to design a shield that reduces the disparity between the average current density and the lowest current density on the substrate profile from 18% down to only 3%. A collaborating colleague, prototyped and performed electrodeposition experiments with some shields we designed and found a good agreement between the measured deposition uniformity and our simulation results. Finally, we also demonstrate shield designs for larger substrate sizes as an extension to the current project.

Introduction

As of today, the chip manufacturing industry has lived up to Moore's law and continued to shrink the feature size to 10nm and even beyond. Copper interconnect is still of choice today and being fabricated at this scale with electrodeposition techniques[1]. In the attempt to minimize non-uniformity of copper electrodeposition over wafers, industry manufacturers have invested in designing optimum plating tools including complicated electric field disturbing shields. However, such tools are almost non-existent in laboratory beaker-scale system, which is still widely used in characterizing electrodeposition processes as the electrolyte composition is modified. The lack of appropriate plating tools often result in unmodified secondary current distribution profile over substrates with "high-edges" and "low-centers". It is very common to see a disparity of around 20% and even more between average current densities and substrate center current densities in similar applications. For example, Lee et al. encountered a 35% measured disparity between average film thickness and substrate center thickness during Ni deposition on 3-in wafer. He was able to design a shield that effectively reduced this disparity to less than 10%.

In this study, we improved this design to be better suited for copper electrodeposition systems of unique solution and kinetics characteristics. This optimization is based upon estimating sensitivities of shield geometries to current density distribution. With this understanding, we determined a highly practical shield design that effectively reduces the current density disparity between the average and lowest-point from 18% down to a minimal 3%. Several variations of the design were prototyped and tested in experiments by a collaborating colleague,

Feng Qiao. We found that the experimental results of as-plated film thicknesses along the coupons are in good agreement with our simulation results. Aside from our designs for small coupons, we also demonstrated optimized designs for larger substrate sizes and proved their effectiveness in larger scale.

Mathematical Model

The electrochemistry system we modeled is based on a widely used copper electrodeposition bath. It contains 0.63 M cupric sulfate ($CuSO_4$) and 0.3 M sulfuric acid (H_2SO_4). The bath operates at room temperature and has a current efficiency of nearly 100%. The electrical conductivity of this electrolyte at room temperature is reported to be 0.115 S/cm. The cathodic charge transfer coefficient α_c is estimated to be 0.5. Current density is assumed to be 15 mA/cm^2.

Figure 1 shows the schematic diagram of the plating cell with an insulating shield used in simulation. All the geometric parameters shown in Fig. 1 are listed in Table 1. The radius of the cathode r_o is chosen as the characteristic length of the system and was fixed to 10mm. In the simulations, the other geometric parameters were made dimensionless by dividing by r_o.

Several assumptions are applied to simplify the simulation. First of all, we assumed the electrolyte to be well mixed, based on the fact that the cupric ion is relatively concentrated and strong agitation is usually performed in these applications. Under such conditions, the current density is given by Ohm's law:

$$i = -\kappa \nabla \phi \qquad (2)$$

in which i is the current density, κ is the electrolyte conductivity, and ϕ is the electrical field in the electrolyte. By conservation of charge, the electrical field in the electrolyte is determined by Laplace's equation:

$$\nabla^2\phi = 0 \tag{3}$$

On any insulating surface such as the cathode coupon holder and the insulating shield, the gradient component of the electrical potential normal to the surface is zero:

$$\mathbf{n}\cdot\nabla\phi = 0 \tag{4}$$

in which $\mathbf{n}$ is the normal unit vector to the corresponding surface. On the counter electrode (anode) surface, a uniform current density is assumed:

$$\mathbf{n}\cdot\nabla\phi = -\frac{i_c\cdot A_c}{\kappa\cdot A_a} \tag{5}$$

in which i_c is the applied cathodic current density, A_c is the surface area of the working electrode (cathode), and A_a is the surface area of the counter electrode (anode). While it may not be achieved in the experiment, the boundary condition (5) ensures that the desired spatial average current density is achieved on both the working and counter electrodes. Since the counter electrode is far away from the working electrode, this imposed constraint does not impact the simulated current distribution on the working electrode.

On the working electrode (cathode) surface, Tafel kinetics is assumed:

$$\frac{\partial\phi}{\partial\mathbf{z}} = \frac{i_o}{\kappa}\exp\left[-\frac{\alpha_c F(V-\phi)}{RT}\right] \tag{6}$$

in which **z** is the axial coordinate and its direction is normal to the working electrode surface, i_o is the exchange current density, α_c is the cathodic charge transfer coefficient, F is Faraday constant, V is the potential on the working electrode, T is the temperature, and R is the gas constant. We assume that the substrate is an ideal conductor (i.e., no terminal effect [2]so that V is constant).

Simulation results depend only on the geometric parameters as well as the Tafel Wagner number of the system, which as described by Newman[3] can be given by

$$Wa_T = \frac{\kappa RT}{r_o \mid i_c \mid \alpha_c F} \tag{7}$$

in which the working electrode radius r_o is taken as the characteristic length of the system.

A boundary element method (BEM) validated, for example, by Lee et al.[4] was employed for the simulation. As shown in Figure 1, the simulation was carried out by assuming an axisymmetric problem in a cylindrical computational region with a dimensionless radius of 5 and an overall height corresponding also to a dimensionless distance of 5. The computational region thus consists of eight sub-regions: the anode surface, the cathode surface, the insulating cathode coupon holder surface, the surface of a hypothetical "insulating wall", and the four surfaces (upper, lower, outer, and inner) of the insulating shield. On the cathode surface, 100 node points were used (and constant elements were assumed[4]). On the insulator region next to the cathode, 100 node points were used for $1 < r/r_o < 2$, and an additional 100 node points were used for $2 < r/r_o < 5$. Along all other surfaces, only

20 nodes were used on each of them, and numerical experiments confirmed that this sparse spacing had insignificant impact on calculated current distribution. Once the sets of equations were generated in matrix form, Gaussian elimination using the subroutine MATINV [5]was used for solving the system of equations.

Results and Discussion

Investigation of the sensitivity of current distribution to shield geometric parameters

Although the Wagner number in the desired beaker-scale system is 0.394, we would like to start with Wagner number at zero, where the most pronounced disparity as well as improvement could be seen. In this way we could best determine the sensitivity of the shield's geometric parameters to current distribution. The parameters of interest are distance between cathode and shield, *h;* outer radius of shield, r_s*;* inner radius of shield, r_{ho}*;* thickness of shield, *t.*

The simulated current densities are normalized against their average for easy comparison with experimental results. The average value is obtained by:

$$\frac{i(r)}{\int_{r=0}^{r=r_0} i(r)\,dr / r_o} = \frac{\pi}{4\sqrt{1-\left(\frac{r}{r_o}\right)^2}} \approx \frac{0.785}{\sqrt{1-\left(\frac{r}{r_o}\right)^2}} \tag{8}$$

As shown in Figure 2 and Figure 3, the variation of r_s and t both showed minimal impact on the current distribution, even with aggressive increments. Hence the shield thickness and outer radius were chosen based on practical considerations.

The outer radius is determined to be the same as the cathode coupon holder radius of 30 mm for easy integration and the shield thickness is determined as 3 mm, which is just thick enough to be dimensionally stable during the rotation motion and not too thick so to minimize the disturbance of mass transfer.

Figure 4a shows multiple simulation results for various h/ r_o . Apparently, h is a very strong factor that disturbs the electric field and thus the current distribution. Figure 4b provides a summary of results by showing the minimum normalized thickness and the standard deviation for the corresponding conditions used in Figure 4a. Here, the standard deviation s of normalized thickness is defined as below:

$$s = \sqrt{\frac{1}{N}\sum_{1}^{N}\left(\frac{\lambda_i}{\lambda_a vg} - 1\right)^2} \tag{9}$$

Depending on the application, the minimum thickness or the standard deviation may be a more relevant figure of merit. Low s and large $\lambda_{\min} / \lambda_{avg}$ are indications of better current distribution uniformity. As shown in Figure 4a, the predicted thickness increases significantly near the edge (r/r_o) and are comparatively flat where r/r_o < 0.75. As the normalized distance h/ r_o increases, the normalized thickness profile approaches the result without a shield. As seen in Figure 4b, the standard deviation has a minimum value at h/ r_o while the minimum normalized thickness reaches a highest value at h/ r_o = 0.35. Combining these two results, h/ r_o appears to be a good range.

As a point of comparison, the standard deviation without the shield is 0.53 and its minimum normalized thickness is 0.64. As seen in Figure 4b, the standard

deviation and minimum thickness approach the values without a shield when h/ r_o increases beyond 0.8, indicating that the influence of the decrease as it is further away from the substrate.

As shown in Figure 5a and 5b, the inner radius of the shield r_{ho}/r_o also demonstrated a strong impact on the current density profile. Following a similar process as described above, the optimum inner radius of the shield r_{ho}/r_o was determined to be in a range between 0.8 and 0.9 as shown in Figure 5c. The results were shown for both $h/ r_o = 0.24$ and $h/ r_o = 0.36$.

Through the investigation with the four geometric parameters of the shield under Wagner number at zero, we determined that the outer radii of the shield as well as the shield thickness are insignificant factors for current distribution. The determination of the ideal value could thus be based on practical considerations in terms of its integration to current plating tools. On the contrary, shield-to-substrate distance and inner radius of shield exhibited strong impact on current distribution. Their respective optimum range is estimated to be h/ r_o between 0.25 and 0.30 and r_{ho}/r_o between 0.8 and 0.9.

Beaker-scale design and validation in experiments

With the above understanding, we were able to design our beaker-scale shield system based on practical considerations. We thus determined $r_{ho}/r_o = 0.8$, $r_s = 3$, $t = 0.3$ and $h/ r_o = 0.24$. In accordance with experiments performed by Qiao et al., where the Wagner number is calculated to be 0.394 based on applied current density of 15 mA/cm^2, we simulated the shield under such new conditions. Figure 6

shows predicted and measured normalized thickness profiles after plating with and without a shield. The measured thickness profiles are similarly normalized against its average obtained by:

$$\lambda_{avg} = \frac{1}{N}\sum_{1}^{N}\lambda_i \tag{10}$$

In both cases, we observed good agreement between experiment and simulation. Also, it is clear that the addition of shield significantly improved the film uniformity. Particularly at Wa = 0.394, we were able to use this shield to reduce the disparity between the minimum to average from 18% down to only 3%.

Figure 7 demonstrates the agreement between experiments and simulations with variations of shield-to-substrate distance and also the better uniformity at h/r_o = 0.24. Figure 8 also showed more experimental results in agreement with our simulation predictions and experimental proved r_{ho}/r_o = 0.8 results in a more uniform current distribution.

Other shapes of design and simulation considerations

Through the course of optimization, we found it sometimes difficult to quantify the uniformity based only on parameters. For example, it could be hard to decide a universally best geometry among the four very different designs shown in Figure 9. Although some distribution patterns have both low standard deviation and large minimum thickness, they are no longer “reasonable” distributions and thus have to be ruled out visually.

Other than the rectangle section design of the shield as discussed above, we also experimented with “step-shape” and ”wedge-shape” designs as shown in Figure 10. From the primary results, we found the “wedge-shape” shield generated a distribution pattern with both high minimum thickness and high level of “flatness”. This is very interesting since it reveals a possibility of further improving the design in the future.

Conclusions

By simulation, optimal insulating shields for lab scale plating tool was designed to redistribute current for much better film uniformity during copper plating on coupons. In the sensitivity screening, it was concluded that the shield-to-substrate distance and inner radius of shield are the most critical factors in redistributing current density. Some of the designs were validated in experiments with good agreement. A significant reduction in the disparity between the minimum current density and the average was obtained. This design was also tested to be very simply integrated and manufactured.

ACKNOWLEDGMENTS

The authors would like to thank Atotech Inc. for their financial support for this project.

Reference

1. R. W. Keyes, Solid-State Circuits Society Newsletter, IEEE **11** (5), 25-27 (2006).
2. C. W. Tobias and R. Wijsman, J Electrochem Soc **100** (10), 459-467 (1953).
3. J. Newman, J Electrochem Soc **113** (12), 1235-1241 (1966).
4. J. M. Lee, J. T. Hachman, J. J. Kelly and A. C. West, J Microlith Microfab **3** (1), 146-151 (2004).
5. T.-A. K. Newman J, Electrochemical Systems (2012).

List of Tables

Table I. Geometric parameters in the simulation of 10mm radius coupon

Geometric parameters	Dimension (mm)
Distance between anode and cathode, H	50
Radius of insulating cathode coupon holder, R	50
Radius of cathode, r_0	10
Distance between cathode and shield, h	To be optimized
Outer radius of shield, r_s	To be optimized
Inner radius of shield, r_{ho}	To be optimized
Thickness of shield, t	To be optimized

Table II. List of symbols

Symbol	Meaning
r_o	Radius of cathode (mm)
R	Radius of insulating cathode coupon holder (mm)
H	Distance between anode and cathode (mm)
h	Distance between cathode and shield (mm)
r_s	Outer radius of shield (mm)
r_{ho}	Inner radius of shield (mm)
t	Thickness of shield (mm)
A_c	Surface area of cathode (cm^2)
A_a	Surface area of Anode (cm^2)
z	Cylindrical coordinate (cm)
r	Cylindrical coordinate (cm)
n	Normal unit vector
κ	Electrolyte conductivity (S/cm)
α_c	Cathodic charge transfer coefficient
F	Faraday Constant, 96,485 C/mol
T	Temperature (K)
R	Gas constant, 8.314 J/(K mol)
Wa	Wagner number
V	Potential on the working electrode (V)
i_c	Applied current density (mA/cm^2)
i	Local current density (mA/cm^2)
i_o	Exchange current density (mA/cm^2)
S	Standard deviation of normalized thickness

List of Figures

Figure 1

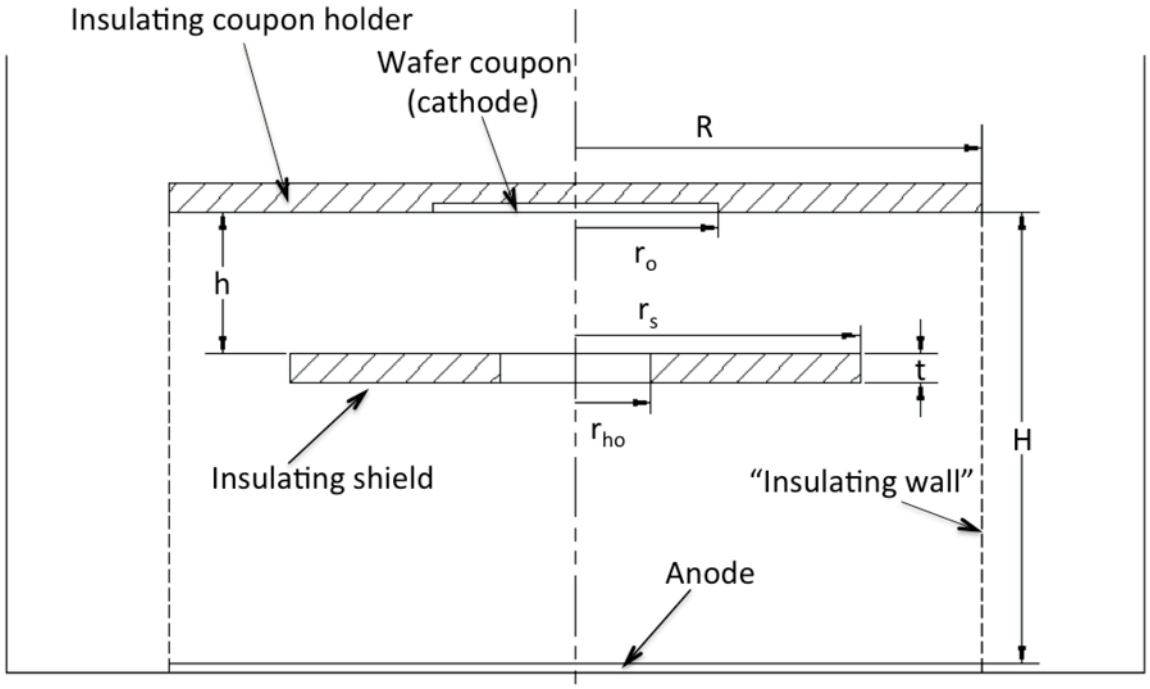

Figure 1. The schematic diagram of the plating cell with an insulating shield used in simulation

Figure 2

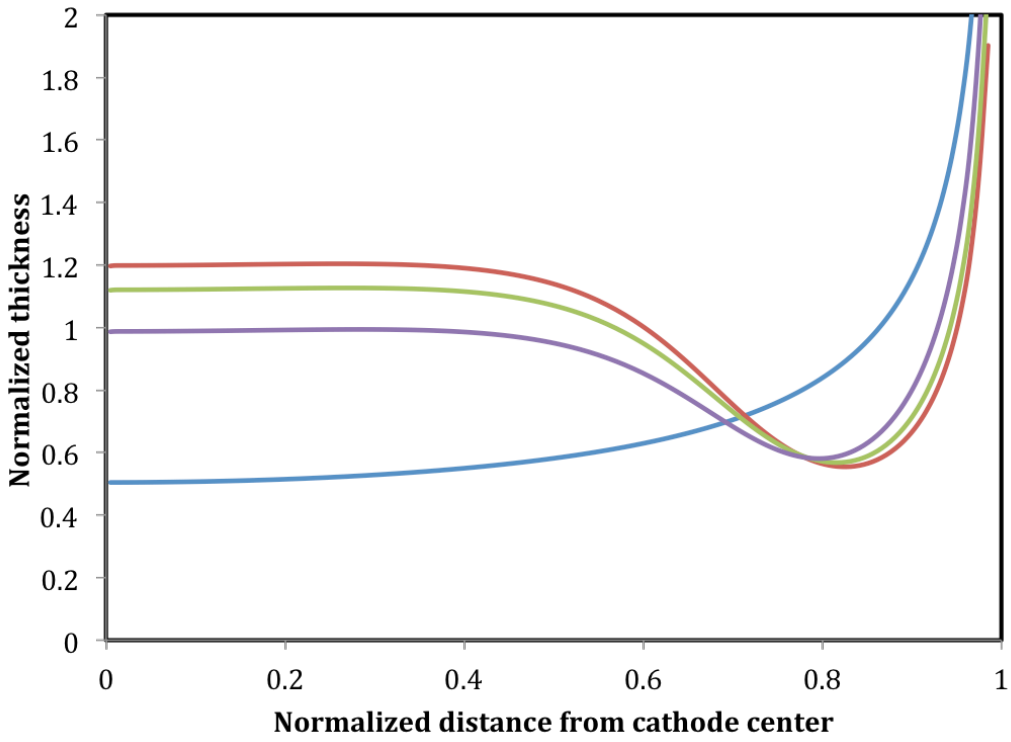

Figure 2. Normalized current distribution profiles for different outer radii of shield r_s/r_o assuming Wa = 0, r_{ho}/r_o = 0.7, h=0.2, t=0.3. For reference, results are also shown for a primary current distribution on a disk without a shield. (red) r_s/r_o=4; (green) r_s/r_o=3; (purple) r_s/r_o=2; (blue) primary distribution without shield

Figure 3

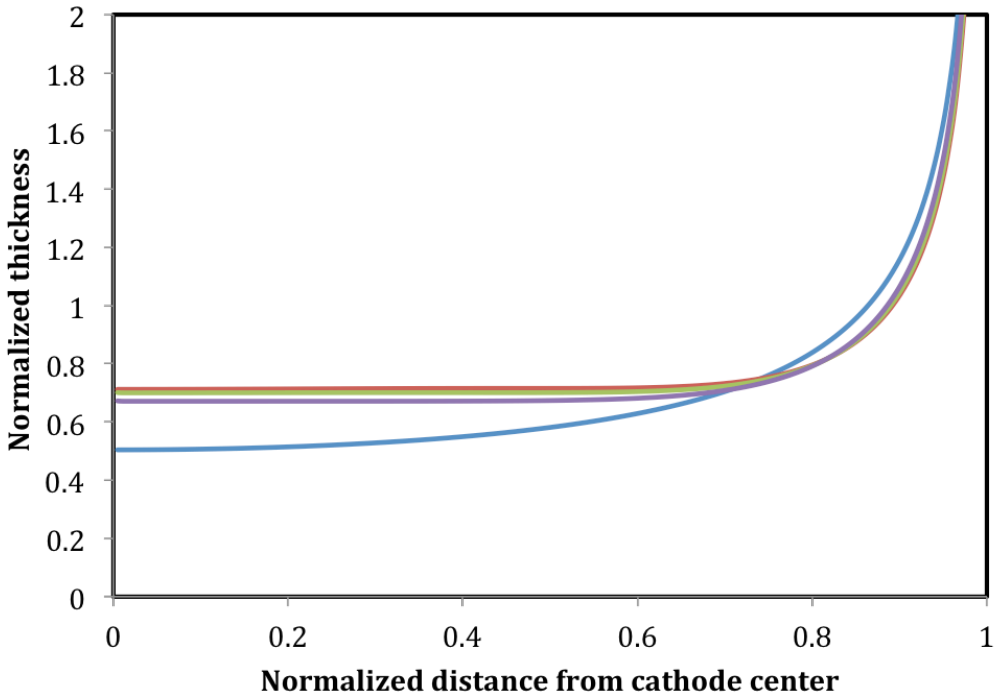

Figure 3. Normalized current distribution profiles for different shield thickness t assuming Wa = 0, r_{ho}/r_o = 0.8, h=0.4, r_s=3. For reference, results are also shown for a primary current distribution on a disk without a shield. (red) t=0.3; (green) t=0.4; (purple) t=0.6; (blue) primary distribution without shield

Figure 4

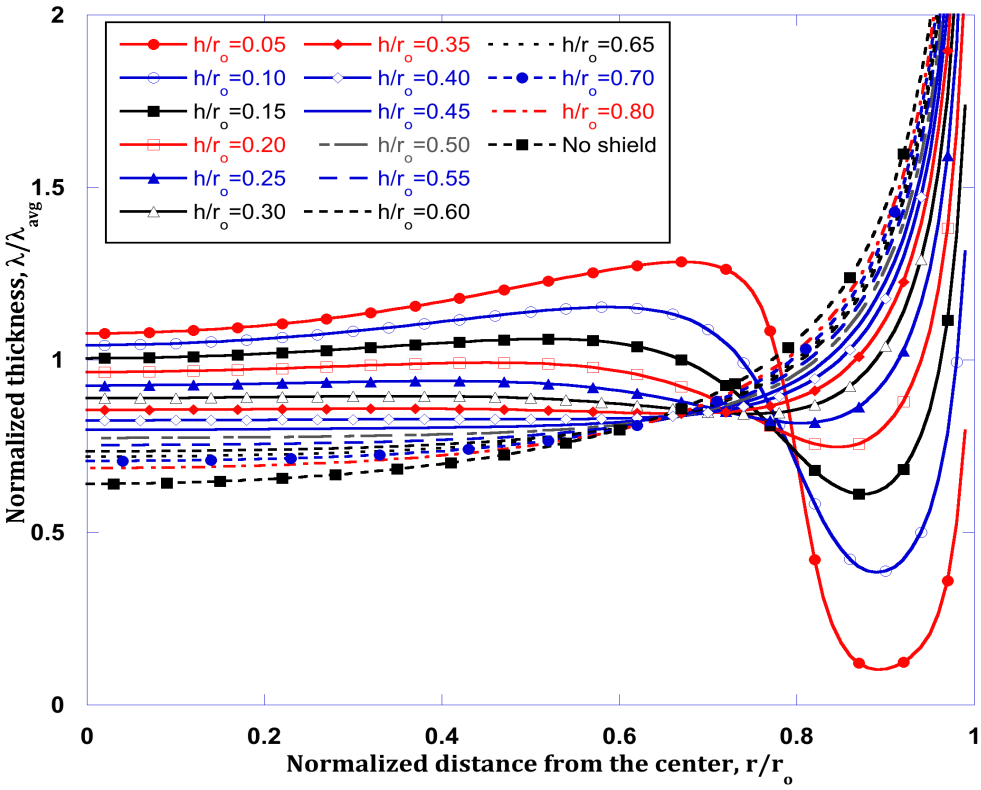
h/r_o=0.05
h/r_o=0.10
h/r_o=0.15
h/r_o=0.20
h/r_o=0.25
h/r_o=0.30
h/r_o=0.35
h/r_o=0.40
h/r_o=0.45
h/r_o=0.50
h/r_o=0.55
h/r_o=0.60
h/r_o=0.65
h/r_o=0.70
h/r_o=0.80
No shield
Normalized thickness, λ/λ_avg
Normalized distance from the center, r/r_o
0
0.5
1
1.5
2
0.2
0.4
0.6
0.8

(a)

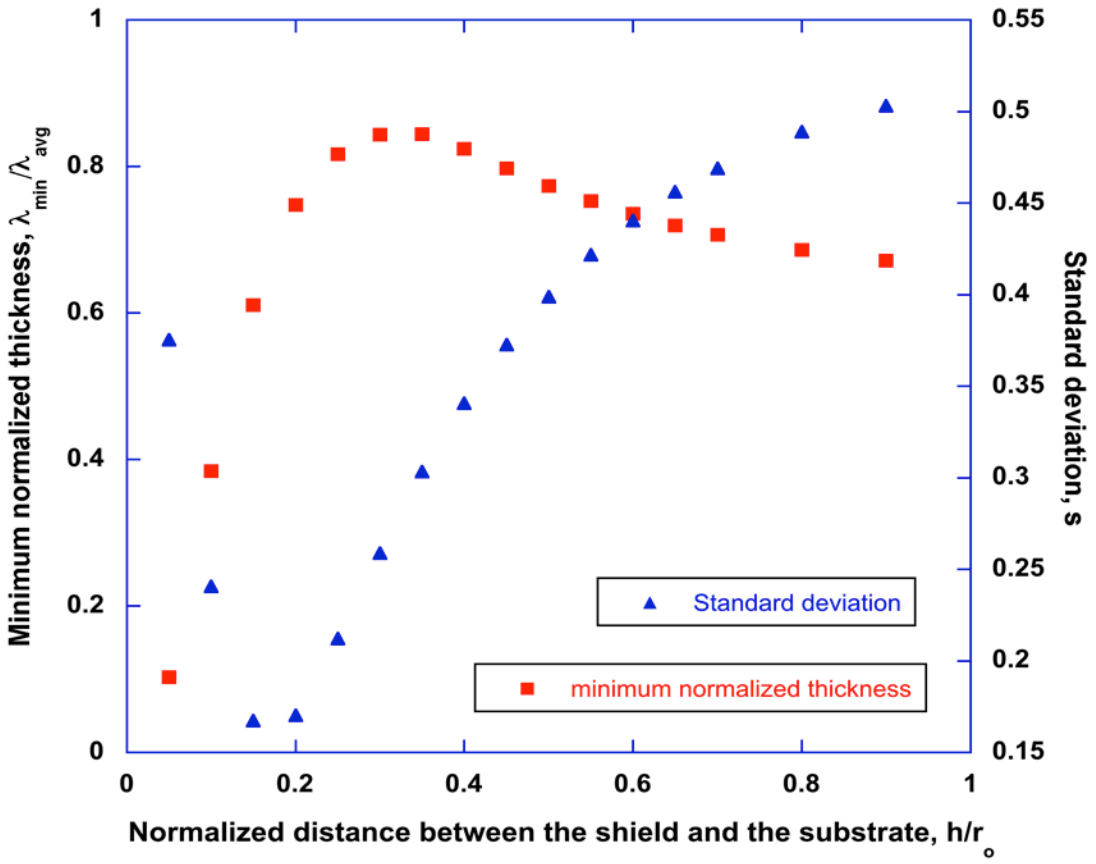

(b)

Figure 4. (a) Normalized thickness profiles for different shield-to-substrate distances assuming Wa = 0. For reference, results are also shown for a primary current distribution on a disk without a shield. r_{ho}/r_o = 0.8, r_s = 3, t = 0.3; (b) Minimum normalized thickness and standard deviation of the simulation results for the corresponding thickness profiles in (a).

Figure 5

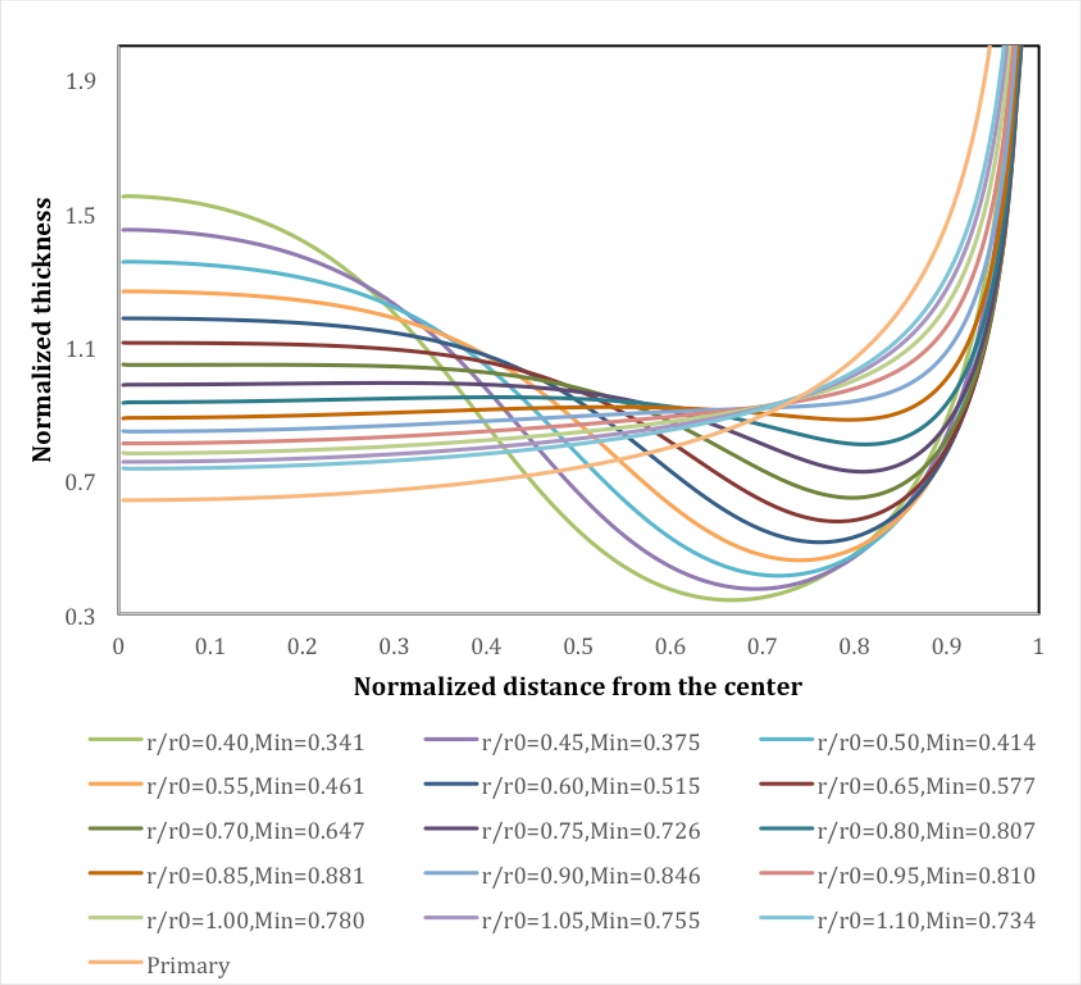
1.9
1.5
1.1
0.7
0.3
Normalized thickness
0
0.1
0.2
0.3
0.4
0.5
0.6
0.7
0.8
0.9
1
Normalized distance from the center
r/r0=0.40,Min=0.341
r/r0=0.45,Min=0.375
r/r0=0.50,Min=0.414
r/r0=0.55,Min=0.461
r/r0=0.60,Min=0.515
r/r0=0.65,Min=0.577
r/r0=0.70,Min=0.647
r/r0=0.75,Min=0.726
r/r0=0.80,Min=0.807
r/r0=0.85,Min=0.881
r/r0=0.90,Min=0.846
r/r0=0.95,Min=0.810
r/r0=1.00,Min=0.780
r/r0=1.05,Min=0.755
r/r0=1.10,Min=0.734
Primary

(a)

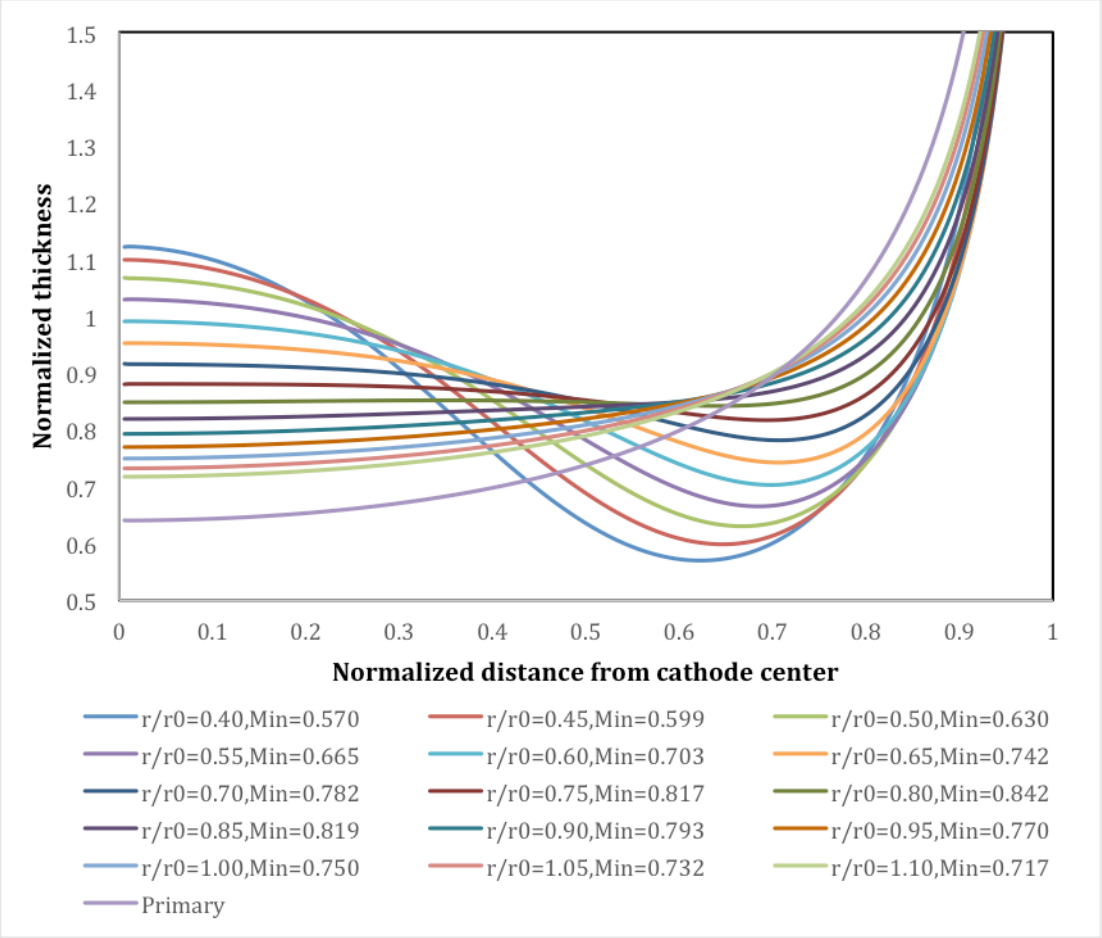
Normalized thickness
1.5
1.4
1.3
1.2
1.1
1
0.9
0.8
0.7
0.6
0.5
0
0.1
0.2
0.3
0.4
0.5
0.6
0.7
0.8
0.9
1
Normalized distance from cathode center
r/r0=0.40,Min=0.570
r/r0=0.45,Min=0.599
r/r0=0.50,Min=0.630
r/r0=0.55,Min=0.665
r/r0=0.60,Min=0.703
r/r0=0.65,Min=0.742
r/r0=0.70,Min=0.782
r/r0=0.75,Min=0.817
r/r0=0.80,Min=0.842
r/r0=0.85,Min=0.819
r/r0=0.90,Min=0.793
r/r0=0.95,Min=0.770
r/r0=1.00,Min=0.750
r/r0=1.05,Min=0.732
r/r0=1.10,Min=0.717
Primary

(b)

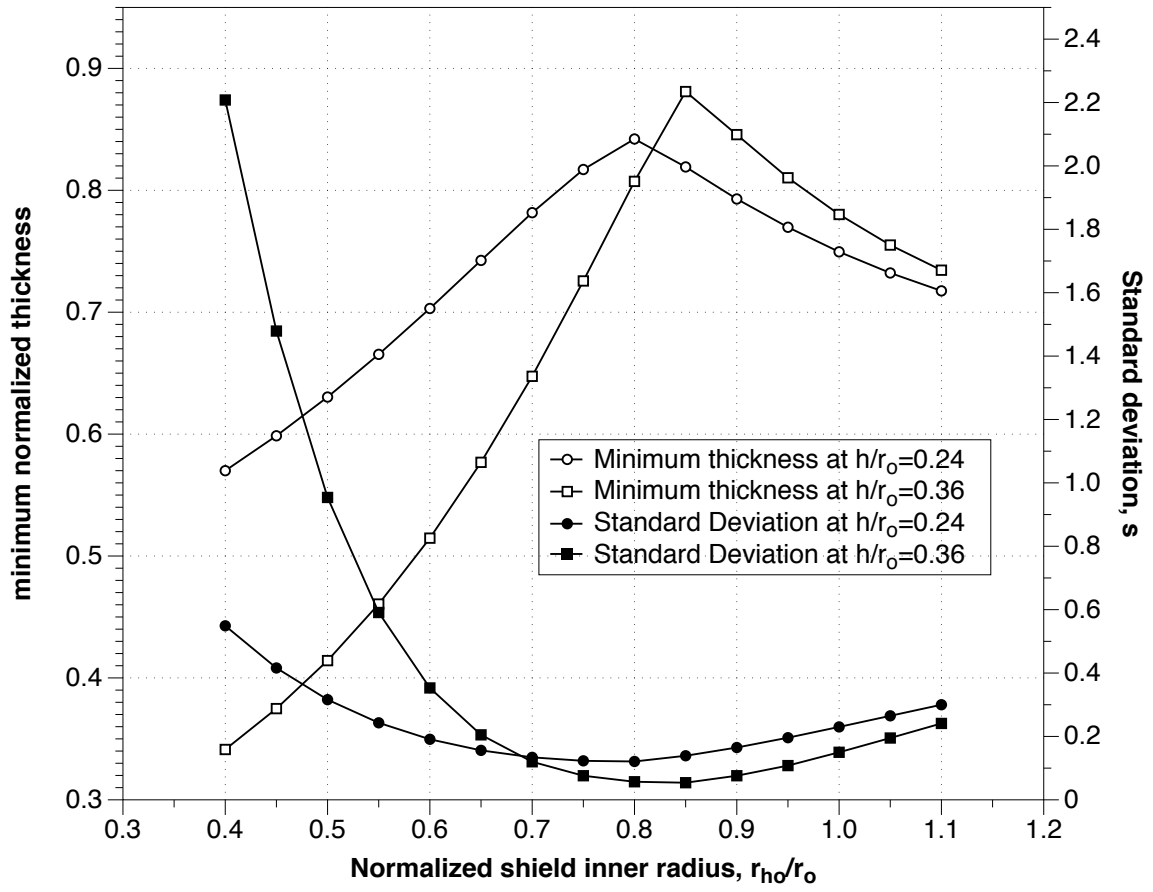

(c)

Figure 5. (a) (b) Respectively at h=0.24 and h=0.36, normalized current distribution profiles under varying r_{ho}/r_o ratio, assuming Wa = 0, r_s = 3, t = 0.3. For reference, results are also shown for a primary current distribution on a disk without a shield. (c) Minimum normalized thickness and standard deviation of the simulation results under varying r_{ho}/r_o ratio in (a) and (b)

Figure 6

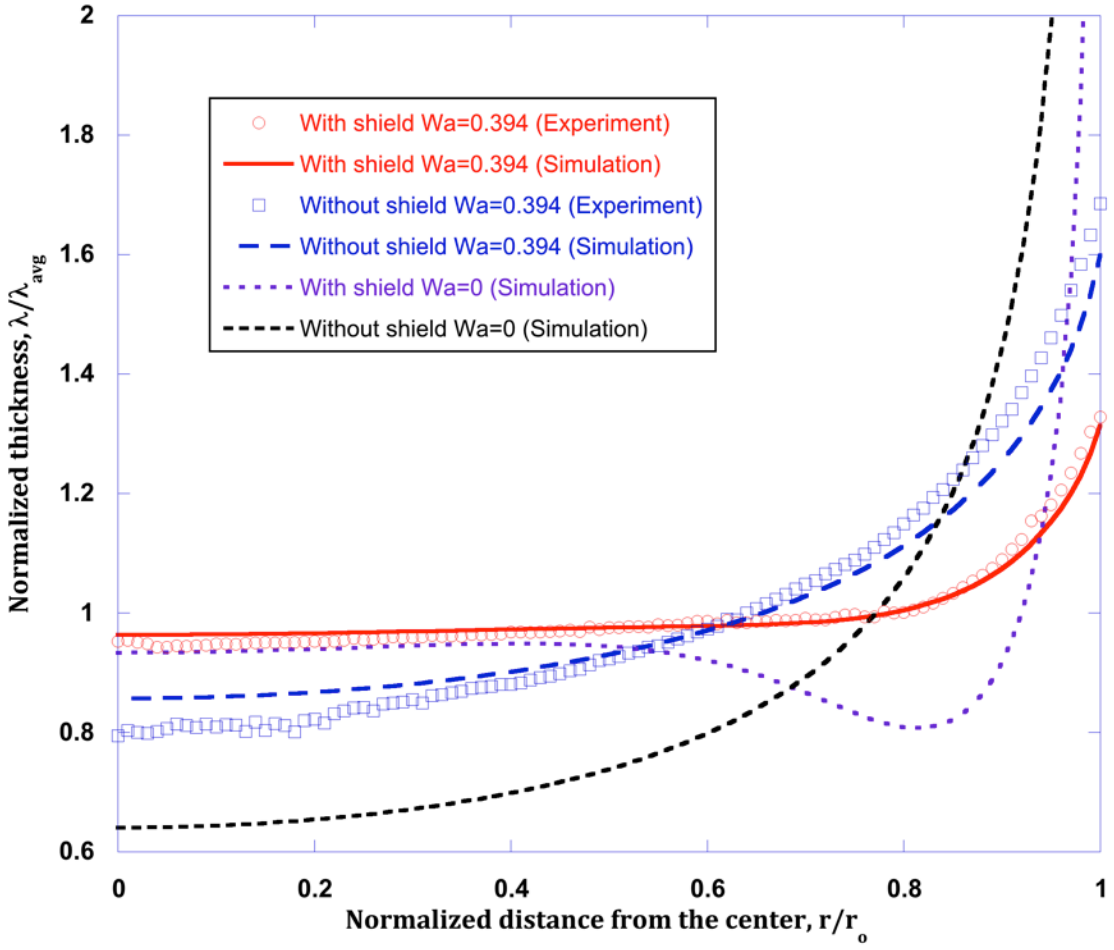

Figure 6. Comparison of simulation and experimental results (Wa = 0.394) for h/r_o = 0.24 and r_{ho}/r_o = 0.8 and for a shield-free RDE. To emphasize the impact on uniformity of electrode kinetics, the simulation results when Wa = 0 are also shown

Figure 7

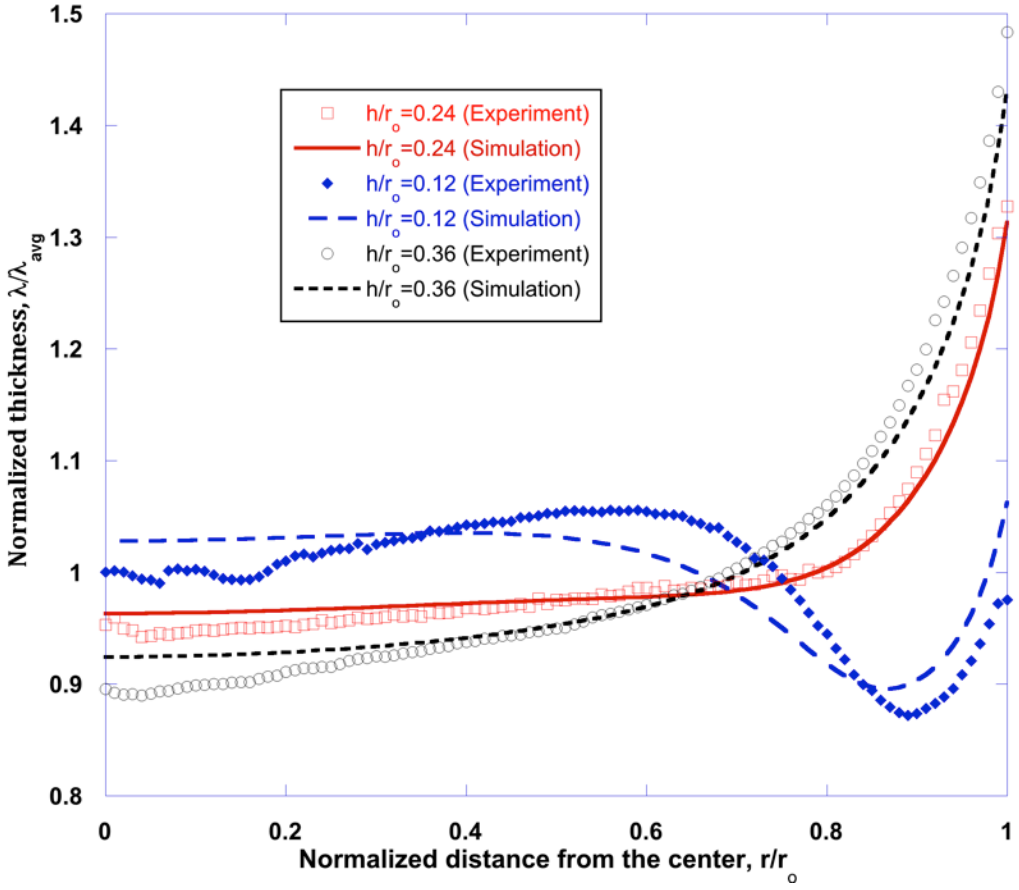

Figure 7. Comparison of simulation and experimental results for r_{ho}/r_o = 0.8, Wa = 0.394 and three shield distances h/r_o.

Figure 8

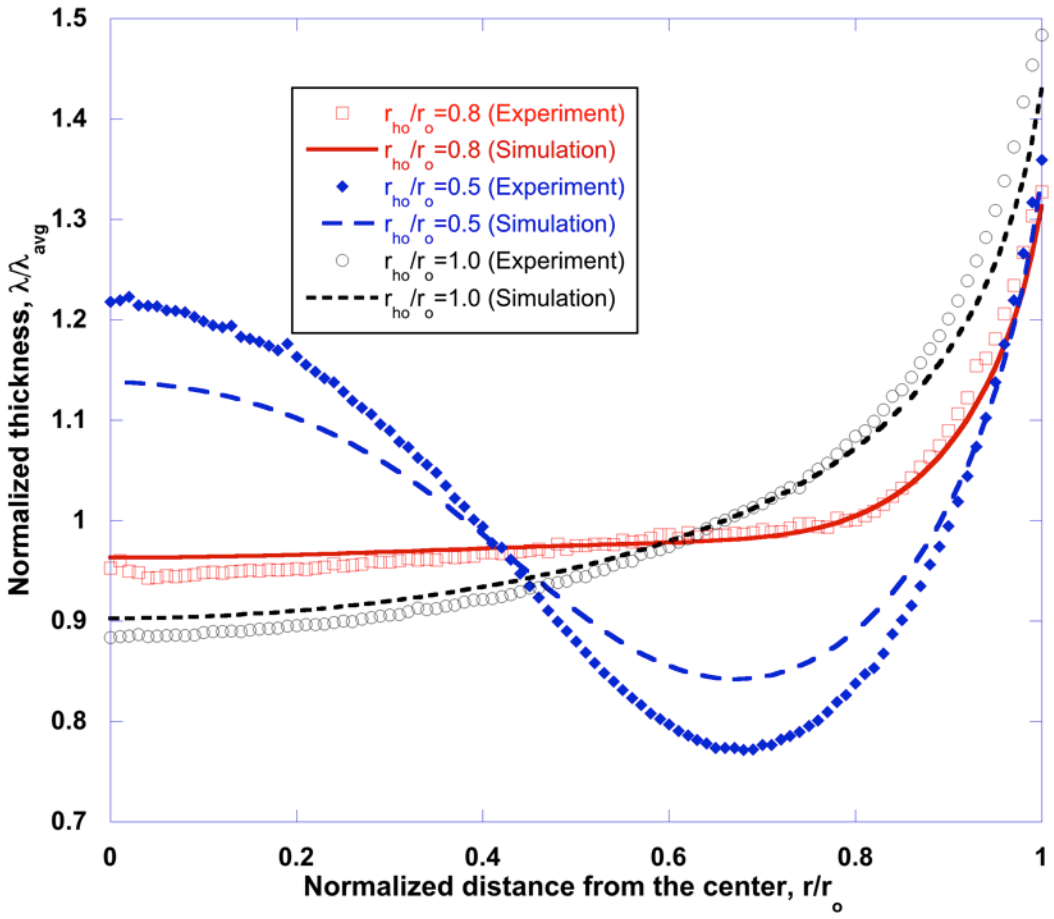

Figure 8. Comparison of simulation and experimental results for different inner radii (r_{ho}/r_o = 0.5, 0.8, 1.0) with h/r_o = 0.24 and Wa=0.394.

Figure 9

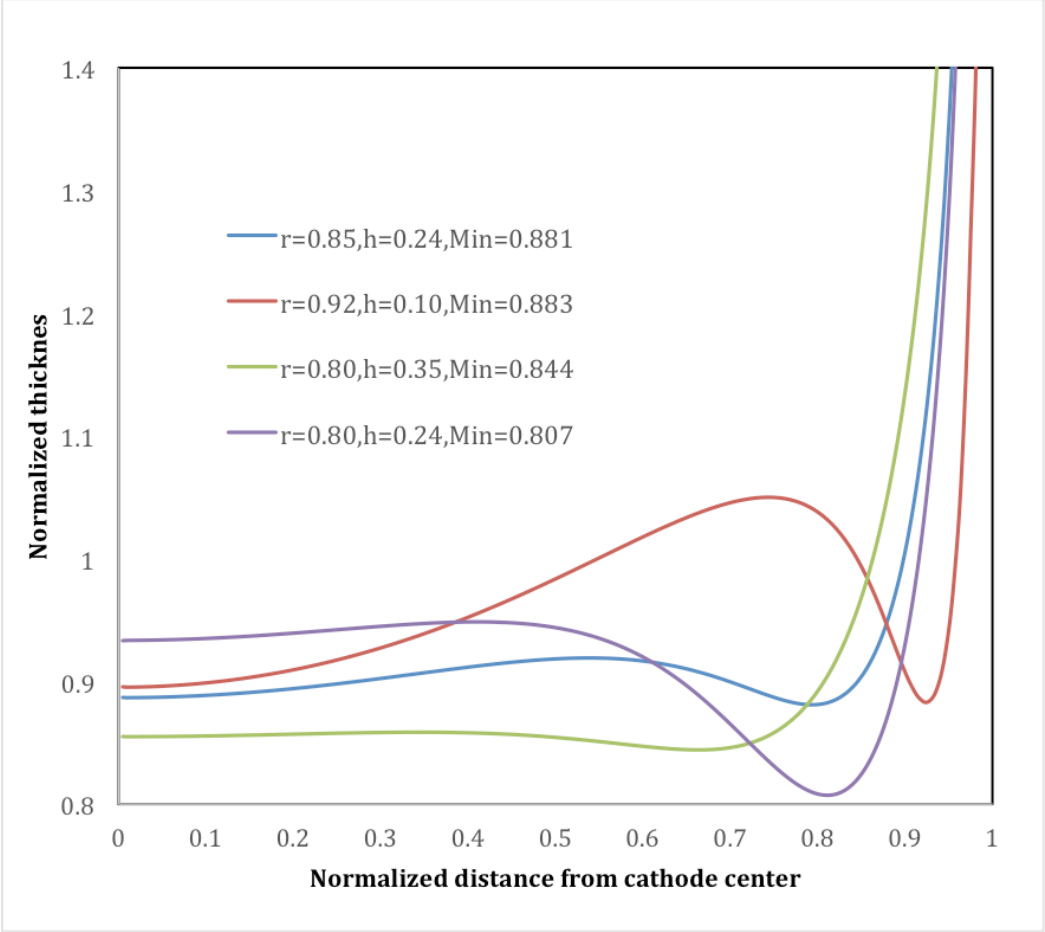

Figure 9. Comparison of current distribution profile types that increase the complexity in evaluation

Figure 10

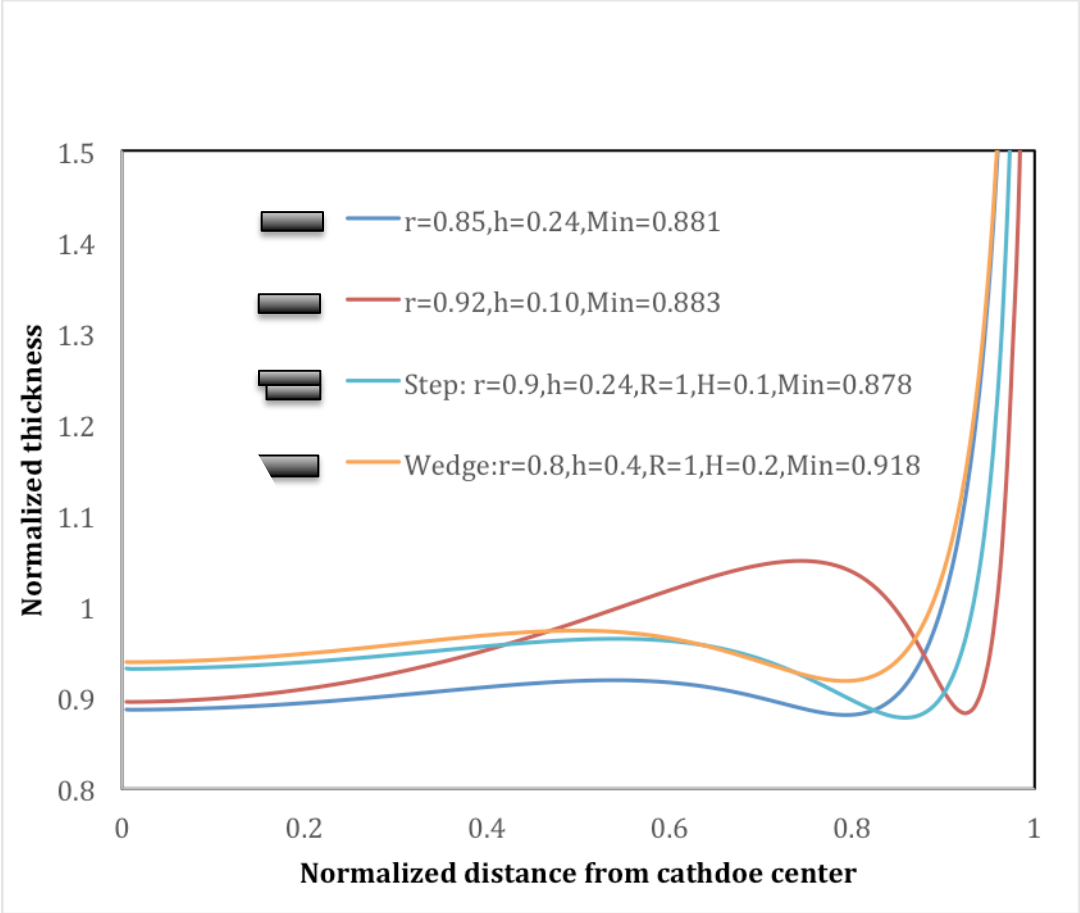

Figure 10. Other step-shape and Wedge-shape shields with schematic drawings

Chapter 5:

Electroless Copper Deposition Coupled with Engineered Phage as a Novel Explosive Biosensor[1]

Abstract

For the last two decades, biosensors for explosives have emerged as a promising candidate because they can be highly selective at ultra-trace levels. Most of these sensors are based on an antigen-antibody framework. Recently some researchers successfully used phage to display peptides that have selective and strong affinity to explosives. Quantitative correlation between these phage and target explosives can be expected. In this study, a novel biosensor is demonstrated that utilizes an electroless copper deposition technique to amplify the signal and to measure phage concentration with both high sensitivity and low operational time and cost. The method's performance was evaluated on multiple substrates. A detection limit in the ppt level is achieved, and a pre-concentration device is shown to detect phage of lower concentrations without significantly increasing the time for detection.

[1] Work in this chapter was carried out in collaboration with Jennifer Haghpanah and Professor Scott Banta from Columbia University

Introduction

Explosives have been manmade in numerous physical forms for mining, engineering, terrorist attacks and warfare protection. During World War II, tons of explosives were produced by industries for warfare protection. These industries contributed to large amounts of contamination of the environment with nitroamine compounds.[1] Significant contamination required significant quantities of water to purify, which lead to "red water" containing up to 30 different nitroaromatic compounds.[2, 3] Groundwater, sediments, soil, and surface waters were contaminated, and more than 1000 people still live within three miles of one site.[1] The toxicological effects, together with the presence of dangerous unexploded ordinance have made detection of explosives a high priority.

Since the early 1990's, the promise of explosives detection based on antigen-antibody formation has become a reality, offering an alternative to physical methods such as LC or GC separation of decomposition products.[4] Antibodies have been engineered to induce changes in physical properties such as optical transmittance or fluorescence, which have been adapted to continuous-flow immunosensors. This has offered the field a highly selective detection platform for explosives at ultratrace levels. Goldman et al. worked on the detection of TNT using recombinant TNT antibodies.[5,6] They were able to isolate binders and evaluate their ability to bind to TNB-BSA via ELISA.[5] Competition ELISA was used to demonstrate that the antibody could bind to other TNB related compounds like TNT. Continuous flow assays revealed that the lowest level of detection for their TNT antibody was 1 ng mL^{-1}, which is lower than the commercially available TNT antibody (2.5 ng mL^{-1}).[5] Overall,

Goldman was able to lower the limits of detection for TNT antibody via directed evolution.[5] Goldman asserted that there was potential for his antibodies to be re-engineered for specificity to other explosives.[5] Green et al. developed an immune sensor based on the reverse displacement format for the detection of TNT in seawater samples.[7]

Goldman et al. also generated a TNB-binding phage, which is the first use of phage peptides to select for TNB.[6] Goldman et al. also generated a TNT antibody via a recombinant anti-TNT antibody isolated from the Griffin Library of phage displayed ScFvs[8, 9] and selected for TNB-BSA. Bateriophage has many unique properties. One of the nice properties of M13 bacteriophage is that the genetic information is inside the protein coat gp8 and it can easily produce 5 proteins (gP3, gP6, gP7, gP8 and gP9) rapidly at a rate of 200 mg/ L.[10] It has also been an attractive template for 1D nanowires because they require minimal modification, have substrate specificity with predictable self-assembly; can store genetic information and yield monodispersed crystalline nanowires.[10]

In addition to the chemistry of affinity biosensors, the signal amplification and transduction components are the other modules essential for a functional biosensor. Several platforms exist that cater to an electrode-based system, including screen-printed electrodes and interdigitated arrays.[11] With respect to affinity chemistry, many of these electrode configurations rely on changes to the electron transfer resistance at the interface between the electrode and sample solution as the analyte binds. Another method for signal transduction, growing in prominence, utilizes surface Plasmon resonance (SPR) phenomenon, which is an

optical technique based on the alterations to the refractive index of an Au surface upon adsorption of analytes.[12, 13] Efforts have recently been attempted to amplify this signal via coupling of a polymerization initiator to a bio-specific interaction, so as to allow inline atomic transfer radical polymerization (ATRP) for signal amplification. Ideally, however, practical implementations of detection systems would circumvent the need for sensitive electronics or precision optics, but rather be distilled to visible optics.

Electroless deposition is a wet redox process in which chelated metal ions are chemically reduced to metal by a reducing agent onto a catalytic substrate surface.[14] Palladium and some other catalysts such as gold have been widely used to catalyze non-metallic substrates to initiate the electroless deposition process.[15-19] Recently, a selective catalyzation technique was developed based on the fact that Pd^{2+} tends to chemically bind ligands containing nitrogen, sulfur and phosphorous donor atoms,[20-22] particularly amines, thiols[23, 24] and pyridine[21] groups. In these studies, self-assembled monolayers, which contain amplification groups that bridges non-metallic substrates and metal deposition, are utilized to achieve great efficacy and selectivity.

We have applied this technique to the detection of explosives. The phage, which binds to certain explosives, contains dense functional groups like amines and thiols, which selectively trap free Pd^{2+} in the catalyzation solution onto the surface to serve as strong catalyst for metal deposition. When Pd is used as a catalyst for electroless metal deposition, it's first reduced from Pd^{2+} to Pd^{0} by the reducing agent in the electroless metal bath. Once it is reduced, it catalyzes efficiently.

Nickel, copper, silver, cobalt, gold, platinum and palladium are all potential candidates to work with bound Pd to deposit electrolessly. Cu was chosen as a mature method for proof of principle. The most widely employed electroless bath uses formaldehyde as a reducing agent. However, like most other electroless metal baths, it requires high temperature and a high pH. An elevated operational temperature increases the complexity of the sensor component, while the high pH above 12 may potentially "damage" the shell of the phage and also entail more expensive alkaline resistive form factors. Alternatively, we explored the possibility of using a bath with dimethylamine borane as reducing agent, which operates under room temperature and mild pH below 9.

Experimental

The palladium catalyzation solution contains 0.1g/L palladium chloride ($PdCl_2$) and 2.5ml/L hydrochloric acid (HCl). The phages together with the substrates are generally immersed in this solution for 2 min to accomplish the catalyzation process. The electroless copper bath is detailed in Table 1 and the processing time varied between 2 min and 30 min. Scanning Electron Microscopy (SEM) experiments were performed on a Hitachi 4700. Plain unmodified silicon wafer coupon was used for the SEM studies.

The buffer solution of phage is TBS buffer with 50 mM Tris-HCl with 150 mM NaCl at a pH of 7.9. All the phage samples, including both insertless phages, which are phages without modification, and bio-engineered phages, which have high affinity to target explosives, were prepared using standard protocols.[6] Directed

evolution techniques have been employed to identify both an RDX binding peptide as well as RDX binding protein. The Banta Lab has developed a label free method to immobilize native RDX without chemical modification. They have used an unstructured phage library that biopanned over the immobilized RDX, and identified several promising RDX-binding peptides via phage display technology (Figure 1). After three rounds of selection over RDX they identified several candidate peptide sequences that were found repeatedly during sequencing results (Figure 1). After performing ELISA, they found promising candidates that could bind to RDX. Within the scope of this study, we performed most of our studies with insertless phages, with other experiments with modified phage with high affinity to RDX, "SGV" and "KAS". The concentration of phage is denoted as "E12", indicating 10^{12} phages per mL.

Results and Discussion

Hypothesis testing on glass slides

In order to test our hypothesis that electroless copper deposition can occur on properly catalyzed phage, we first carried out our process flow on glass slides. 10 μL of pre-cultured E13 insertless phage was first dropped on a glass slide. Once it was completely dried, we immersed our glass slide into palladium catalyzation solution for 2 minutes followed by aggressive rinsing with DI water to completely remove free palladium ion, which potentially could interfere with signal from catalyzed phage. Then the treated glass slide was immersed in electroless copper bath for 2 minutes as shown in Figure 2. Before deposition, the glass slide was

transparent all around and no phage was visible. After 1 minute, a semi-transparent deposit appeared, which continued to darken for 2 minutes.

We also performed control experiments with the catalyzation processes eliminated, or phage solution replaced with its buffer solution and neither showed any deposit. These experiments was in good agreement with our hypothesis that palladium solution can selectively catalyze phage for electroless copper deposition and the existence of phage can be visibly displayed within a couple of minutes.

A side comparison between insertless, SGV and KAS phages (modified phage with high affinity to explosive) is shown in Figure 3. Instead of using E13 phage, we used a lower concentration of 25E11 and all three showed similar solid deposits after 3 minutes of deposition. It not only showed the method's ability to detect phage at 4 times lower concentrations, but demonstrated the consistency of phage modification and the extendibility of our results with insertless phage to bioengineered practical phages. This extendibility is also consistent with our hypothesis that the catalyzation and electroless copper deposition occurs on the shell of the phage and hence should not be affected by the insert on the head. For simplicity, we performed most of our other experiments with the insertless phage.

"Coffee Ring Effect" and microscopic observation of interconnected phage

A typical M13 bacteriophage is 6.6 nm in diameter and 880 nm in length. The rate of electroless copper deposition has been determined to be about 15 nm/s under the present conditions.[22] Thus after 3 minutes of electroless copper deposition, the phage is expected to grow into about 100 nm in diameter and 970

nm in length, and these dimensions are in good agreement with the SEM images (Figure 4).

Assuming phage is spread evenly on the spotted area of about 0.3 cm^2 with 5 μL of solution, we calculated that the coverage of phage after 3 minutes of deposition could reach 170% with E11 phage concentration and 17% at E10 phage concentration. Apparently, the calculated coverage would be higher than the real distribution due to stacked structures and uneven distribution. However, we believe this estimation at least partially explains the drastic change in appearance when we used any phage concentration below E11.

A closer look at the microscopic configuration through SEM further explained the phenomena as shown in Figure 4. Looking at both copper coated E11 phage and E10 phage on silicon wafer coupon substrates, we could clearly see that they both formed a multilayer-stacked structure on the edge of the "hydro ring", while only E11 phage displayed a high coverage over the entire surface. The E10 phage, calculated to have 17% coverage (maximum) of the spotted area, only showed a very thin ring of about 10 μm in width, which is both less than 1% coverage and invisible to the bare eye. The image suggests that the phage, during the drying process, are preferentially "dragged" to the edge of the ring and "built" a stacked "wall" structure along the ring. This phenomenon is known as the "coffee ring effect". The mechanism of this effect has been shown to be due to capillary flow induced by the differential evaporation rates across the drop, i.e. liquid evaporating from the edge is replenished by liquid from the interior.[25] Once the "wall" is established with multiple layers of phage, a reversal capillary force between phage and liquid

counteracts the coffee ring force,[26] allowing the rest of the phage in the solution to remain in the center area. However if the phage amount is not sufficient to "build a wall high enough", there would be no phage covering the center area rather than the edge. There is also an opportunity to take advantage of the effect to physically reduce the effective condensed area without reducing the evaporating area, thus increasing the density of phage on the substrate to optimize the sensor detection limit.

Another interesting effect we observed is that the phage is self-aligned in a highly ordered manner in the same direction at the edge, especially the bottom layer, as shown in the bottom right image. The ordered structural property of hierarchically organized phage architectures is of interest in many fields. [27-29]

Demonstrating the explosive detection on simple filter paper substrate

Filter paper has been a widely used signal transduction substrate in various applications, such as pregnancy test and blood glucose test. It is sufficiently inexpensive for single-use applications, while also possessing properties allowing for the liquid to diffuse. However, it was not a priori clear whether phage could bind to filter paper into a pattern that results in visible and concentration-dependent form after copper deposition without interference from residual Pd^{2+}.

To investigate the palladium catalyzation process on filter paper, we studied copper deposition with varying concentration of palladium solution dropped on filter paper without phage. Figure 5 shows how $PdCl_2$ could serve as catalyst on filter paper for copper electroless deposition and the detection limit of $PdCl_2$

through this method. We could clearly see that all concentrations above 0.0156 g/L showed similar dark deposit within 2 minutes of deposition. This concentration was only about 10% of our regular palladium concentration. Direct adsorption of palladium catalyst onto filter paper would thus interfere with phage detection.

On a side note, a prolonged attempt of 10 minutes with electroless copper deposition, however, showed a very bold deposit at even lower concentrations of 0.0078g/L and a smaller dot at 0.0039 g/L as also shown in Figure 5. Further increase in deposition time to 3 hours did not show any deposit for lower concentrations. The well-reproduced results strongly suggest that apart from the deposit appearance (darkness, size), deposition time needed to display the deposit may also be a robust indicator for catalyst densities.

Since the previous method of catalyzation after phage is dried on substrate has been determined to introduce significant amount of interference from palladium, we instead catalyzed phage in solution before being dropped onto filter paper. As shown in Figure 6, we have also demonstrated that we can isolate phage from the Pd^{2+} via filter paper. When phage is catalyzed in solution by Pd^{2+} and then dropped on filter paper for electroless copper deposition, a rough deposit appeared in the center along with a smooth outer ring-shape deposit. Our hypothesis for the structure was that Pd^{2+} diffuses along with the diffusing liquid on the filter paper and forms a hydro-ring when dried and subsequently catalyzes electroless copper. The rough deposit in the center highly resembles the appearance of deposited phage on other substrates. A comparison experiment was conducted as shown to validate this hypothesis. Instead of using the mixture of both phage and free Pd^{2+}, we filtered

out phage using a 0.2 μm filter and dropped the solution with only free Pd^{2+} that passed through the filter. After electroless deposition, similar ring-shape structure appeared, which proved our hypothesis about the natural separation of free Pd^{2+} signal and phage signal.

Another interesting phenomena we observed is that certain peptide inserts, which have been shown to have high affinity to certain explosives, showed even stronger signal than unmodified insertless phage. Or at the very least, our findings with insertless phage should be extendible to peptide-engineered phage.

Correlating Electroless copper deposition indicators with phage concentration

As a very familiar substrate and robust tool for bioengineers, a pasteurized plastic well plate was of interest as a substrate. With its unique array form, it also has the potential as the substrate for bulk detection in sensors. Two reasonable indicators we have determined are time for the deposit to turn visible and area of deposit captured by image analysis software with a specified cutoff for gray scale.

The top image on Figure 7 shows 3 identical arrays of 10-μL phage solutions of different concentrations dropped and dried into each well and then subjected to catalyzation and 3 minutes of electroless deposition. Starting from top left well with E14 concentration, each well contained half concentration of the previous well, all the way to the bottom of second column of 3E9. The plot in Figure 7 shows the correlation between phage concentration and area of deposit. It turned out that for lower concentrations from E11 to E12, the area method could very well differentiate

areas with different concentrations proportionally. However, once the concentration reaches E12, the areas are almost identical. This method seems to work well in the situations where the range of target phage concentration is both small (within one magnitude) and known so that a proper time of deposition could be determined to achieve the sensitivity.

Another method however, uses the time it takes for the deposit to be visible. In an application, this could be automated with an image analysis tool. The resulting calibration curve between this time and phage concentration is shown in Figure 8. From E14 down to E11, with deposition time increases linearly from 20 seconds to 120 seconds. Below E11, as illustrated previously, the detection limit is reached so an impractically long time would be needed to see a deposit. For concentrations above E14, the time is less than 20 seconds and it became difficult to capture a difference in time. Overall, the time method has demonstrated its ability to analyze wide range of concentration with high accuracy and practicality in implementation

Pre-concentrating test solution on filtering column and detecting phage in-situ

While we have demonstrated the reproduced success of displaying phage with electroless copper methods with a phage concentration of E11 and above, the best sensor in the market today can detect explosives on ppt (parts per trillion) level (~E11). Recent research has seen a magnitude lower sensitivity. Assuming each phage associates with one explosive molecule, our detection limit is potentially on par with the best practice on the market. On the other hand, detection of phage

beyond our detection limit is possible by pre-concentrating the solution prior to electroless deposition.

Among others, the simplest and practical way would be to concentrate phage solution on a DNA spin column with a silica membrane. The membrane has an area of about 0.5 cm^2, which is similar to the previous solution drops on other substrates. However, instead of applying a minimal solution of only 10 ul, we filtered large amounts of solution through the membrane, while retaining all phage but minimal buffer solution on the membrane. With a simple portable vacuum pump, it only takes 10 minutes or so to pass 100 mL of solution, which increased the phage density by 4 orders of magnitude. Figure 9 shows that 20 µl of E12 phage solution barely showed a deposit and smaller concentrations failed to obtain any visible deposit. However, when we concentrate E9 phage by applying 100mL of solution, E10 phage by applying 10mL solution and similarly E11 and E12, we saw a deposit for phage concentrations ranging from E13 all the way down to E9. When we compared our results to our control sample (TBS buffer with 50 mM Tris-HCl with 150 mM NaCl, pH 7.9), we saw little to minimal copper deposition on our negative control (Figure 9). For these experiments, the membrane was treated with electroless copper deposition for 5 minutes.

Conclusions

In this study, a novel sensor amplification method was demonstrated that utilizes electroless copper deposition to image adsorbed phage. It is found that bio-engineered phages perform similarly to insertless phage during the signal

transduction process with electroless deposition. A non-formaldehyde electroless copper deposition bath was utilized so that the deposition operates at room temperature, non-corrosive pH and less toxicity. Evaluation studies of signal type to monitor phage concentration suggest the time required for a deposit to appear is the most accurate and robust. Finally, a detection limit in the ppt level is directly achieved on multiple substrates, and a pre-concentration device can be utilized to detect phage of lower concentrations without significantly increasing the time for detection.

ACKNOWLEDGMENTS

The authors gratefully acknowledge Jennifer Haghpanah and Professor Scott Banta of Columbia University for preparing all the high quality phage samples, both insertless and modified, for the scope of the study.

Reference

1. J. D. Rodgers and N. J. Bunce, Water Research **35** (9), 2101-2111 (2001).

2. K. Levsen, P. Mussmann, E. Berger-Preiß, A. Preiss, D. Volmer and G. Wünsch, Acta hydrochimica et hydrobiologica **21** (3), 153-166 (1993).

3. T. Urbanski, M. t. b. Jurecki and S. t. b. Laverton, *Chemistry and technology of explosives*. (Pergamon Press New York, NY, 1964).

4. J. I. Steinfeld and J. Wormhoudt, Annu Rev Phys Chem **49**, 203-232 (1998).

5. E. R. Goldman, A. Hayhurst, B. M. Lingerfelt, B. L. Iverson, G. Georgiou and G. P. Anderson, Journal of Environmental Monitoring **5** (3), 380-383 (2003).

6. E. R. Goldman, M. P. Pazirandeh, P. T. Charles, E. D. Balighian and G. P. Anderson, Analytica Chimica Acta **457** (1), 13-19 (2002).

7. T. M. Green, P. T. Charles and G. P. Anderson, Analytical biochemistry **310** (1), 36-41 (2002).

8. B. Krebs, H. Griffin, G. Winter and S. Rose-John, Journal of Biological Chemistry **273** (5), 2858-2865 (1998).

9. A. D. Griffiths, S. C. Williams, O. Hartley, I. Tomlinson, P. Waterhouse, W. Crosby, R. Kontermann, P. Jones, N. Low and T. J. Allison, The EMBO journal **13** (14), 3245 (1994).

10. C. Mao, D. J. Solis, B. D. Reiss, S. T. Kottmann, R. Y. Sweeney, A. Hayhurst, G. Georgiou, B. Iverson and A. M. Belcher, Science **303** (5655), 213-217 (2004).

11. N. J. Ronkainen, H. B. Halsall and W. R. Heineman, Chemical Society reviews **39** (5), 1747-1763 (2010).

12. R. Yatabe, T. Onodera and K. Toko, Sensors **13** (7), 9294-9304 (2013).

13. W. P. Hall, S. N. Ngatia and R. P. Van Duyne, The journal of physical chemistry. C, Nanomaterials and interfaces **115** (5), 1410-1414 (2011).

14. G. O. Mallory, American Electroplaters and Surface Finishers Society: Orlando, FL, 1-56 (1990).

15. S. Yokogawa, K. Kikuta, H. Tsuchiya, T. Takewaki, M. Suzuki, H. Toyoshima, Y. Kakuhara, N. Kawahara, T. Usami, K. Ohto, K. Fujii, Y. Tsuchiya, K. Arita, K. Motoyama, M. Tohara, T. Taiji, T. Kurokawa and M. Sekine, Ieee T Electron Dev **55** (1), 350-357 (2008).

16. T. Ishigami, T. Kurokawa, Y. Kakuhara, B. Withers, J. Jacobs, A. Kolics, I. Ivanov, M. Sekine and K. Ueno, Proceedings of the Ieee 2004 International Interconnect Technology Conference, 75-77 (2004).

17. Y. e. a. kakuhara, Proc. 2009 Int. Conf. Solid State Device and Materials, 804 (2009).

18. Y. e. a. Hayashi, Proc. 2009 IITC(IEEE 2009), 252.

19. W. K. Han, G. H. Hwang, S. J. Hong, H. H. An, C. S. Yoon, J. H. Kim, M. J. Lee, G. Hong, K. S. Park and S. G. Kang, Appl Surf Sci **256** (8), 2649-2653 (2010).

20. P. M. Maitlis, Academic Press, New York (1971).

21. W. J. Dressick, C. S. Dulcey, J. H. Georger, G. S. Calabrese and J. M. Calvert, J Electrochem Soc **141** (1), 210-220 (1994).

22. N. Kulyk, S. Cherevko and C. H. Chung, Electrochim Acta **59**, 179-185 (2012).

23. L. N. Xu, J. H. Liao, L. Huang, N. Gu, H. Q. Zhang and J. Z. Liu, Appl Surf Sci **211** (1-4), 184-188 (2003).

24. M. Ishida, M. Kasuga, T. Kaneko and T. Shimoda, Jpn J Appl Phys 2 **39** (3ab), L227-L229 (2000).

25. R. D. Deegan, O. Bakajin, T. F. Dupont, G. Huber, S. R. Nagel and T. A. Witten, Nature **389** (6653), 827-829 (1997).

26. B. M. Weon and J. H. Je, Phys Rev E **82** (1) (2010).

27. S. Magdassi, M. Grouchko, D. Toker, A. Kamyshny, I. Balberg and O. Millo, Langmuir : the ACS journal of surfaces and colloids **21** (23), 10264-10267 (2005).

28. M. H. Kim, S. H. Im and O. O. Park, Advanced Functional Materials **15** (8), 1329-1335 (2005).

29. B. G. Prevo and O. D. Velev, Langmuir **20** (6), 2099-2107 (2004).

List of Tables

Table I. Electroless copper bath constituents

Copper sulfate (CuSO4)	0.03 mole/L
Dimethylamine borane (DMAB)	0.1 mole/L
Ethylenediaminetetraacetic acid (EDTA)	0.035mol/L
Triethanolamine (TEA)	0.38mole/L
Temperature	22°C
pH (Adjusted with Tetramethylammonium hydroxide (TMAH))	8.6

List of Figures

Figure 1

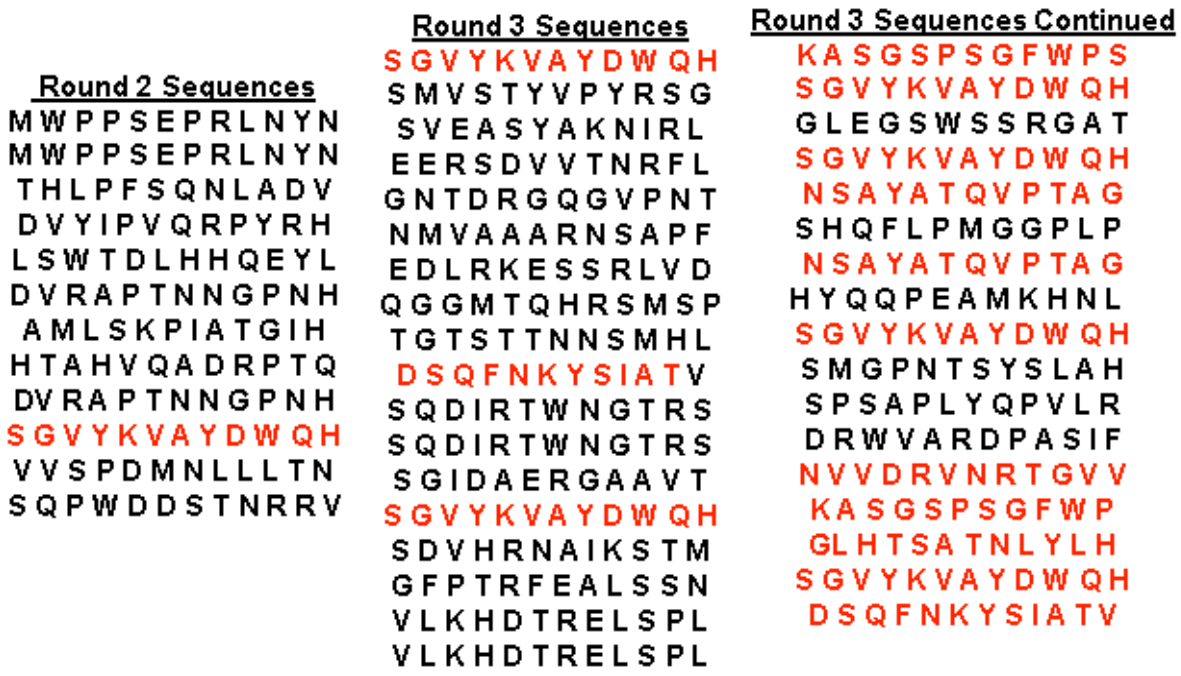

Figure 1. Promising sequences from biopanning RDX with sequences that appear multiple times highlighted in red (Courtesy of Jennifer Haghpanah)

Figure 2

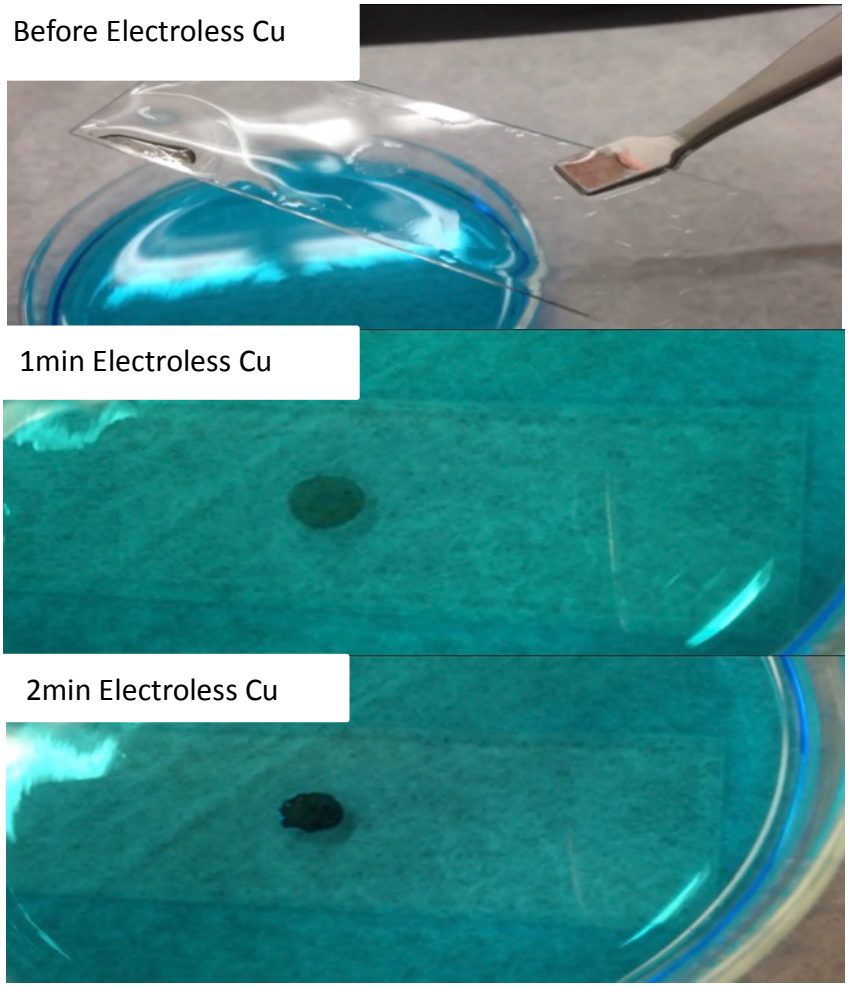

Figure 2. Step-wise demonstration of electroless copper deposition on E13 phage dried on glass slides. Top image is right before electroless deposition; middle image after 1 minute of deposition and bottom image after 2 minute of deposition

Figure 3

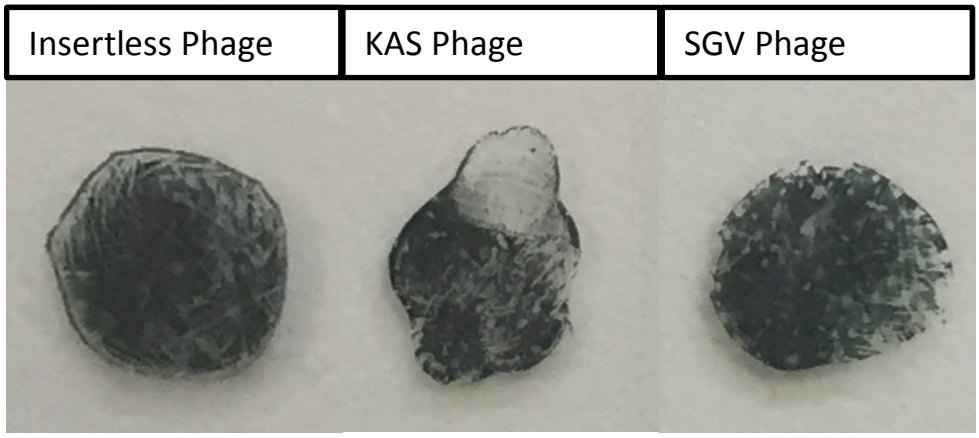

Figure 3. Comparison of electroless copper deposition results between insertless phage with bio-engineered phages (KAS and SGV) that bind to explosive. All three types of phage are of 25E11 in concentration and have undergone 3 minutes of deposition

Figure 4

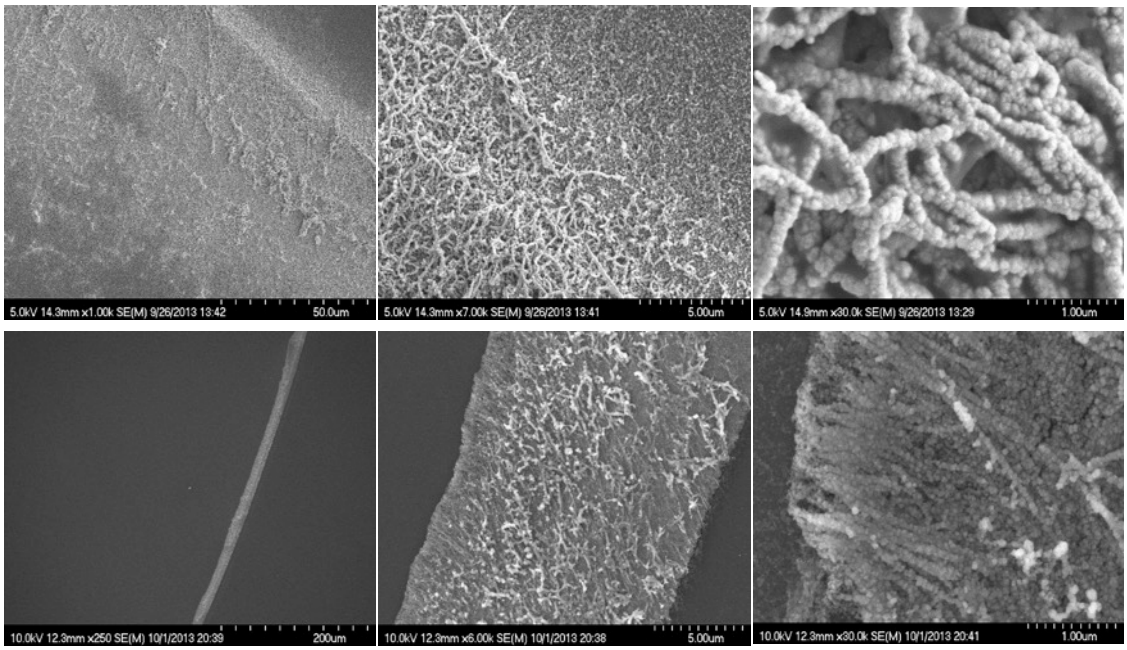

Figure 4. Images on the top row are when phage is of higher concentration (E11), Electroless Cu successfully formed a film on the spot (denser near the edge). Images on the bottom row are when phage is of a lower concentration of E10 and that no film was formed within the spotted area, except that most of the phage aggregated and aligned on the "hydro ring"

Figure 5

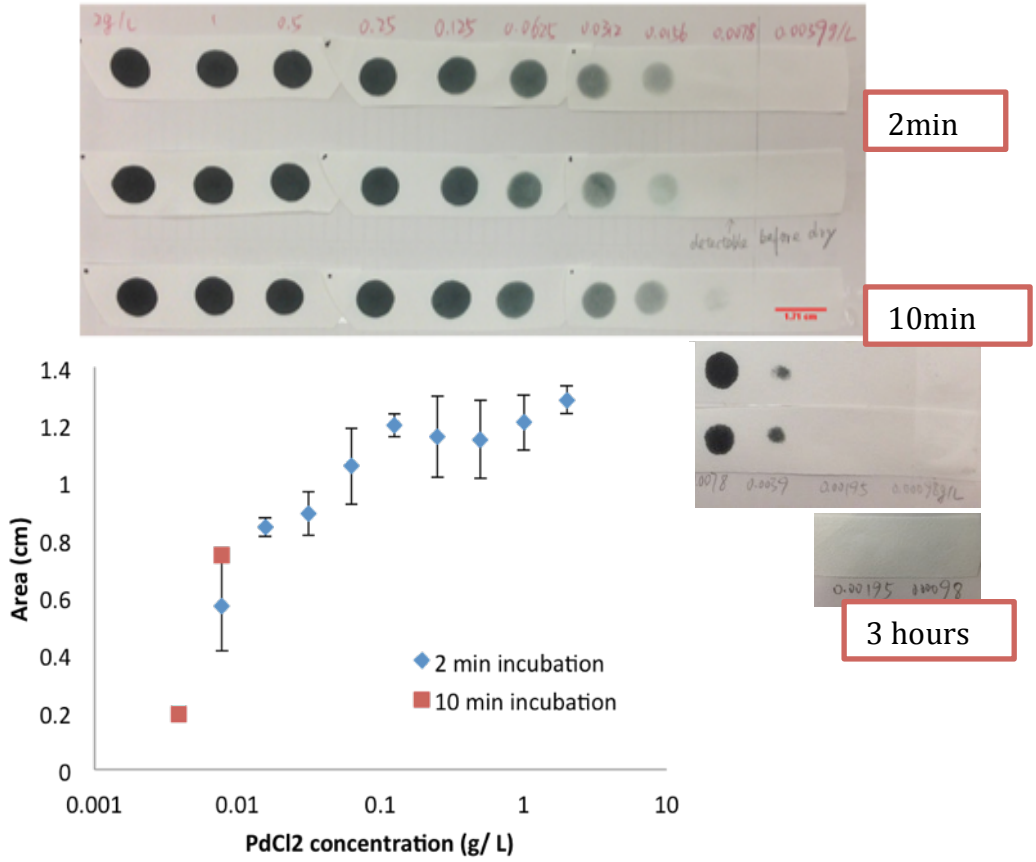

Figure 5. $PdCl_2$ calibration curve, showing the detection limit of $PdCl_2$ on filter paper and how prolonged deposition detected lower concentration of catalyst

Figure 6

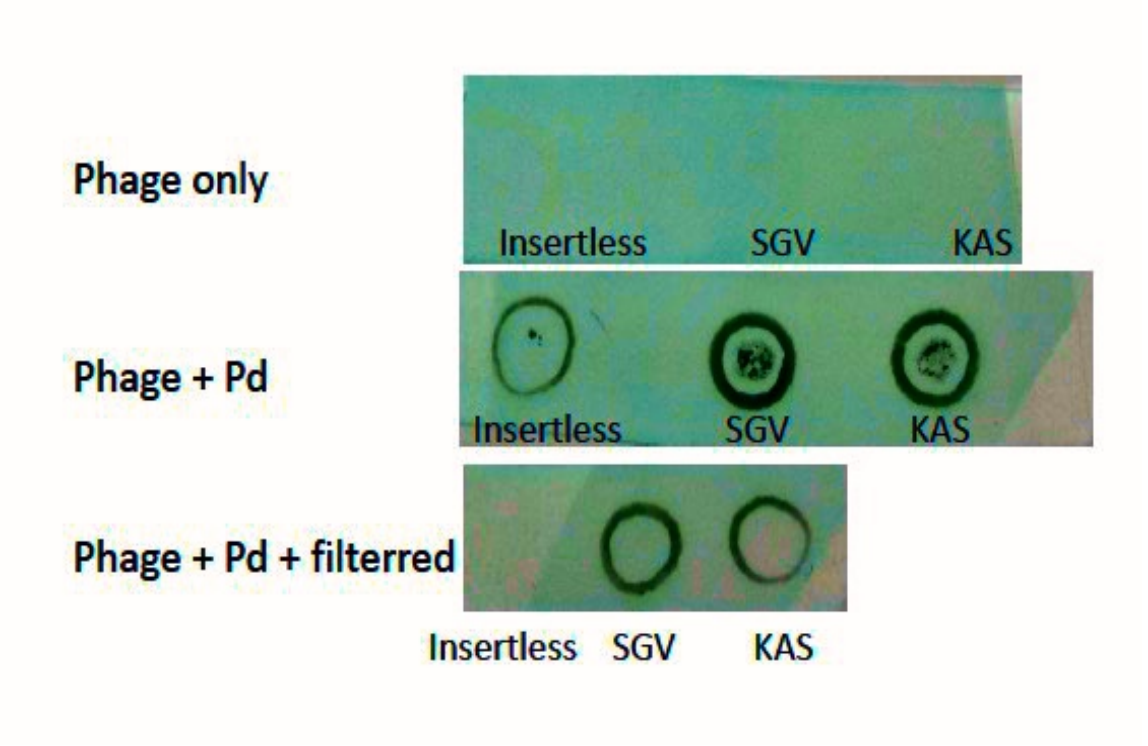

Figure 6. Detection of insertless phage and RDX binding peptide phages on filter paper with phage not catalyzed by Pd, phage catalyzed by Pd and filtered solution of the mixture of phage and Pd catalyzation solution.

Figure 7

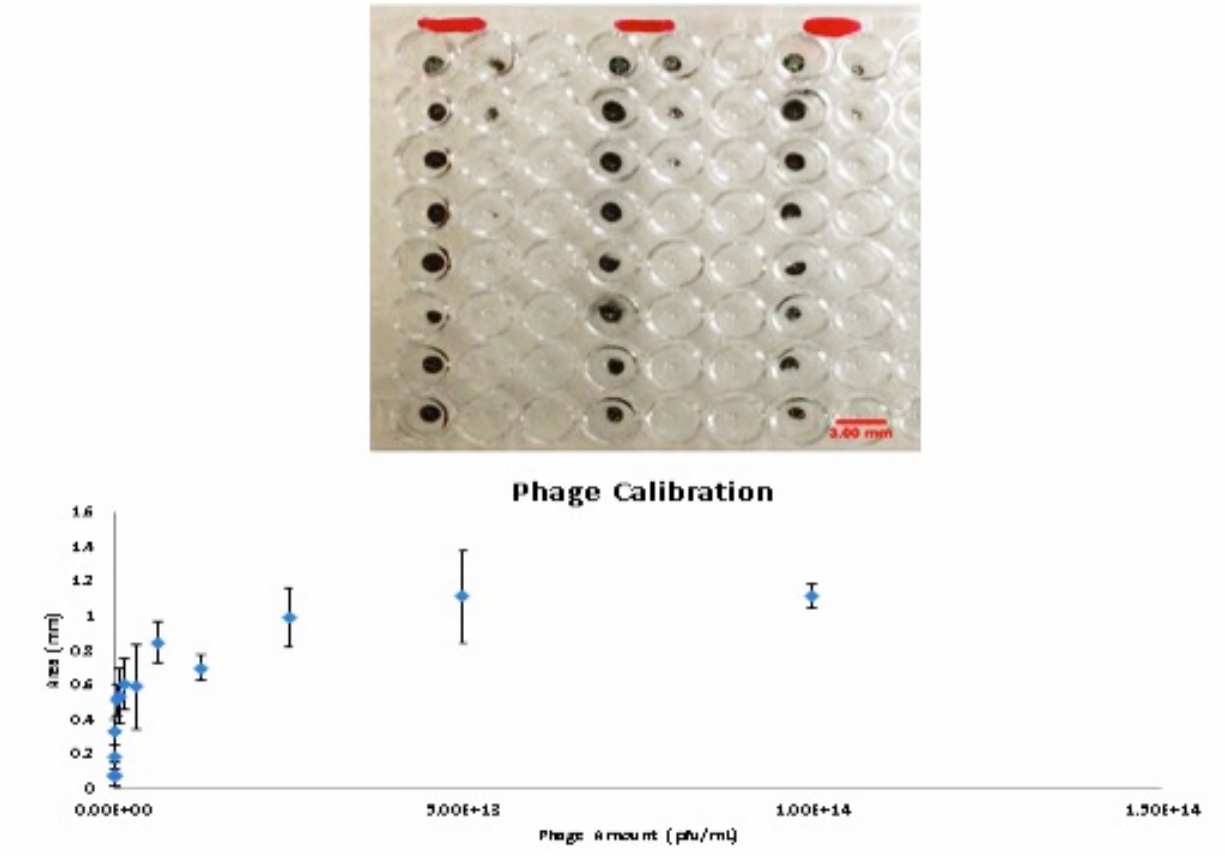

Figure 7. Phage concentration calibration curve with respect to the area of deposit after 3 minutes of deposition. The pasteurized well plate has polystyrene surface. Starting from top left well with E14 concentration, each well contained half concentration of the previous well, all the way to the bottom of second column of 3E9

Figure 8

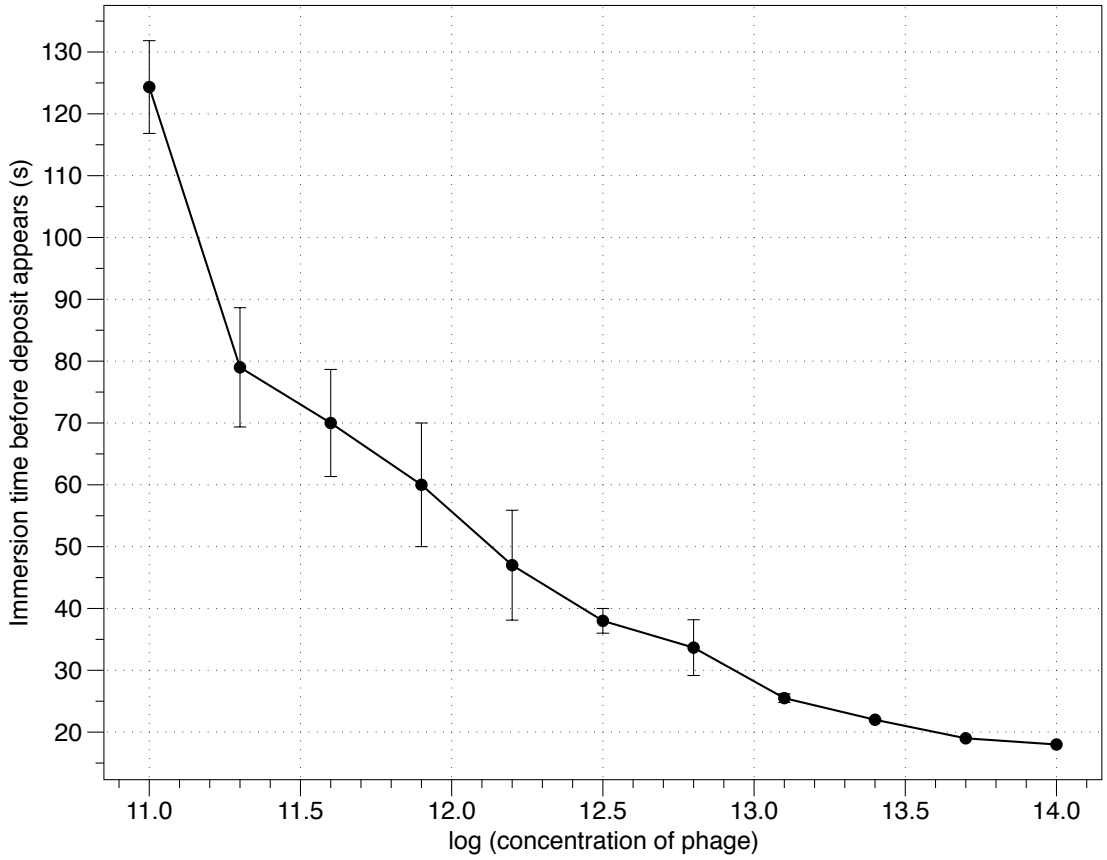

Figure 8. Phage concentration calibration curve with respect to the time it took for deposit to appear. The pasteurized well plate has polystyrene surface. Starting from top left well with E14 concentration, each well contained half concentration of the previous well, all the way to the bottom of second column of 3E9

Figure 9

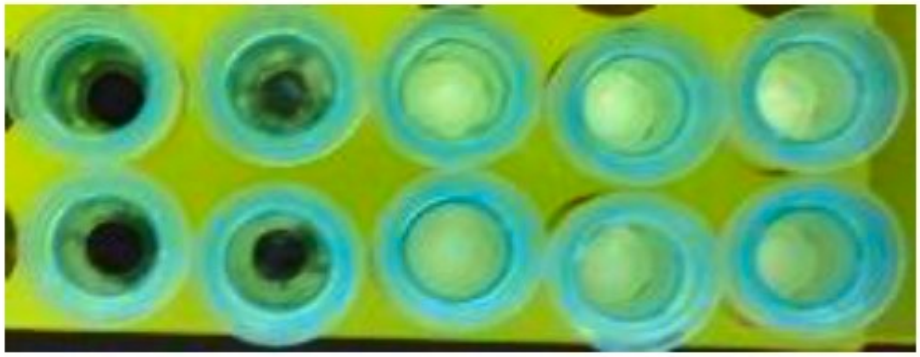

(a)

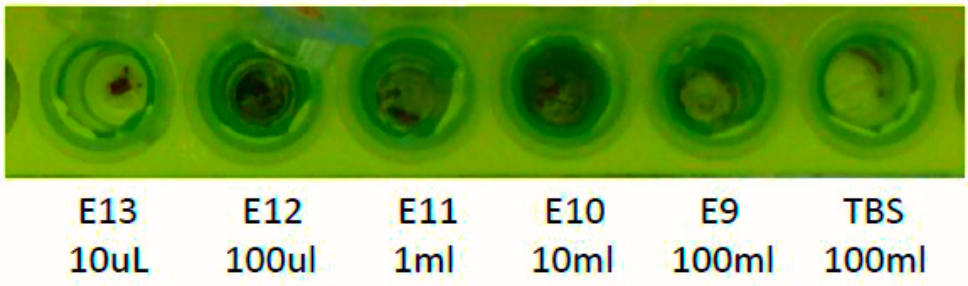

(b)

Figure 9. Electroless copper deposition (5 min) of catalyzed phage on silica filter column substrates (a) Appearance of deposit with labeled phage concentration and 20 µL phage applications (b) Appearance of different concentrations and volumes of phage with the control sample (TBS buffer with 50 mM Tris-HCl with 150 mM NaCl, pH 7.9)

Chapter 6:

Design of a Copper Electrowinning Cell

Abstract

Low energy density of media feed into a bioreactor is a bottleneck for the application of *Acidithiobacillus ferrooxidans* cells for production of hydrocarbon products facilitated by electricity. A novel method utilizing Cu^{2+}/Cu redox mediator has been proposed to improve existing energy density and this requires a copper electrowinning cell. A design of the electrowinning cell was built in-house and characterized in terms of cell voltage, current efficiency, deposit quality and product yield. Key factors that affect the electrowinning cell performance, such as inlet iron concentration, presence of citrate, electrode material and overall current applied were investigated.

Introduction

Genetically modified *Acidithiobacillus ferrooxidans* bacteria are chemolithoautotrophic cells that can fix gaseous CO_2 to produce valuable chemicals by extracting energy from the oxidation of iron using atmospheric O_2 as the electron acceptor:[1, 2]

$$4FeSO_4 + 2H_2SO_4 + O_2 \rightarrow 2Fe(SO_4)_3 + 2H_2O \quad (1)$$

A. ferrooxidans cells are attractive candidates for electrofuels application as they grow planktonically and the Fe^{3+} produced by the cells can be readily reduced electrochemically. *A. ferrooxidans* cells grow optimally at 28°C to 33°C and pH ranging from 2.0 to 2.3.[3-7] However, under such conditions, the solubility of Fe^{3+} is very low, resulting in limited energy density. [8]

Recently, two approaches have been explored to increase the system's energy density. The first approach utilizes Fe^{3+} chelators to solubilize iron.[9] The inclusion of citric acid up to 70 mM was demonstrated to successfully accommodate 72 mM iron in the system at an optimum pH of 2.2. However, further increase in citrate content to chelate more Fe^{3+} would induce inhibitory effect from citric acid, limiting the energy density still far below desired.

The second approach was to introduce an additional redox couple with higher solubility than iron, which can indirectly transfer electrons to *A. ferrooxidans*, such as V^{3+}/V^{4+}. In order for the redox couple mediator to work, the standard redox potential of the redox mediator must be lower than that of Fe^{2+}/Fe^{3+}, so that Fe^{3+} could be continuously reduced to supply Fe^{2+}. V^{4+} solubility is significantly higher than that of Fe^{3+} and the bacterial has been reported to be able to tolerate up to 98

mM of V^{4+}.[10] A combination of 10 mM Fe^{2+} supplemented with 60 mM V^{3+} has been shown to exhibit similar growth rate as the media with just iron.[11] With the introduction of such redox couple, both the Fe^{3+} solubility limitation and inhibition effects are resolved, with the same energy density contained. However, on the electrochemical side, the reduction of V^{4+} required a relatively lower reduction potential. This results in a higher overall cell voltage (the potential difference between the positive and negative electrode on the power supply during electrowinning process), which means higher power consumption, as well as the evolution of H_2, which lowers operational efficiency. Moreover, further increase in energy density with the V^{3+}/V^{4+} redox couple is limited by the bacteria's tolerance of V^{4+} up to 98 mM.

In this study, a design of a copper electrowinning cell was demonstrated to potentially enable an effectively higher energy density for the electrofuels process; in this case the system uses a Cu/Cu^{2+} redox couple. As determined previously in our group, the bacteria could tolerate over 400 mM Cu^{2+} (below 500 mM), as compared to 98 mM for V^{4+}. Moreover, the redox couple of Cu/Cu^{2+} supplies 2 electrons per pair, while both Fe^{2+}/Fe^{3+} and V^{3+}/V^{4+} supply only one electron to the bacteria. Thus 400 mM of Cu^{2+} is equivalent to 800 mM of Fe^{3+} in terms of energy density, which is a significant improvement over alternatives.

Although the Cu/Cu^{2+} redox couple is similar to the V^{3+}/V^{4+} redox couple in the sense that they both supply electrons through reducing Fe^{3+} to Fe^{2+}, the implementation is quite different. First of all, unlike the all-soluble vanadium redox system, the reduced copper is a solid and can be fed thus at very "high

concentrations." However, the reduction of Fe^{3+} with solid form Cu is not easily integrated inside the bioreactor because the abundant air through sparging in the bioreactor could easily oxidize or passivate copper. Moreover, the local concentration of Cu^{2+} around copper solids might be too high and become toxic for the bacteria.

To overcome these challenges, a system was designed, as illustrated in Figure 1. A rapid flow will be cycled between bioreactor and copper column to maintain a high level of Fe^{2+} and a high Fe^{2+}/Fe^{3+} ratio in the bioreactor. A second outflow from the Cu column goes to the electrowinning tank to reduce copper and generate sulfuric acid for the potentially coupled bioreactor. The flow rate to the electrowinning cell is independently determined by system requirements. Prior to entering the cell, biomass is removed. A cell was designed by analogy with industrial cells used for the production of copper sheets. The advantage of designing such an electrowinning tank not only lies in its abundance of relevant designing guidelines, but also in its promising commercial value in producing high quality copper sheets at extensive scale. At small lab scale, these electrowon copper sheets are recycled to the Cu column to maintain the mass balance. At large scale, high quality electrowon copper sheets could be harvested and copper scraps of lower value could conceivably be supplied in the Cu column for the same effect.

In addition to the design of the coupled system, an electrowinning cell was built in house and characterized in terms of current efficiency, cell voltage, deposit quality and product yield capability. Key factors that determine the electrowinning performance are identified with detailed study carried out with respect to electrode

material, solution conductivity, inlet iron concentration, presence of citrate and overall current applied.

Concepts and Design of Electrowinning Cell

Electrode Process

The cathode process is mainly the electrodeposition of copper:

$$Cu^{2+} + 2e^{-} \rightarrow Cu \tag{2}$$

along with the side reaction:

$$Fe^{3+} + e^{-} \rightarrow Fe^{2+} \tag{3}$$

In most cases, these two reactions consume all the electrons provided by the power supply. However, at very high currents or low copper concentrations, hydrogen evolution can also occur:

$$2H^{+} + 2e^{-} \rightarrow H_2 \tag{4}$$

On the other hand, the oxygen evolution is the major reaction on the anode side:

$$2H_2O \rightarrow O_2 + 4H^{+} + 4e^{-} \tag{5}$$

along with the oxidation of Fe^{2+}:

$$Fe^{2+} \rightarrow Fe^{3+} + e^{-} \tag{6}$$

The cyclic oxidation and reduction of the Fe^{2+}/Fe^{3+} redox couple could potentially lower the current efficiency, especially when the iron concentration is high.

Faraday's Law

For general electrochemical applications, quantitative correlation between electric charge Q applied and *n* moles of the substance reduced or oxidized is analyzed with Faraday's Law:

$$n = \frac{Q}{z \cdot F} \tag{7}$$

where *z* is the reactant's valence number change and *F* = 96485 C/mol is the Faraday constant. Electrical charge Q is the product of current and time $Q = I \cdot t$.

Current Efficiency

The current efficiency (CE) is the ratio of the current used to reduce copper to the total applied current:

$$CE = \frac{n_{Cu_{redu}}}{n_{Cu_{equivalent}}} \times 100\% \tag{8}$$

$$n_{Cu_{equivalent}} = \frac{I \times t}{2 \times 96485 C / mol} \tag{9}$$

The amount of electrodeposited copper reduced was determined by two methods. The first method was weighing the produced copper sheets. This method is particularly easy to use if all the metal adhered to the substrate. However, in the cases where adhesion is poor, the collection of metal sheets becomes difficult and inaccurate.

Another method uses the measured copper concentration of the effluent and through a material balance, implicitly determining the amount of deposited copper. This latter approach was used when copper adhesion was poor.

Cell Voltage

Energy minimization is a key consideration in designing an electrowinning cell. Thus, the cell voltage is a key metric. The total voltage across the cell can be divided into three components:

1. The reversible equilibrium potential difference between the oxidation reaction and reduction reaction ($V_{eq} = V_a - V_c$).
2. The activation and concentration overpotentials of the anode and cathode (η_a, η_b).
3. The potential drop due to the ohmic resistance (IR drop) of the electrolyte and the electrical contacts (U_{ohm}). The electrical contact resistance is negligible in our application. For parallel plate electrodes, IR drop can be estimated by:

$$U_{IR} = I \times R_{ohm} = I \times \frac{d}{A_e \times \kappa} = i \times \frac{d}{\kappa} \qquad (10)$$

where d is the spacing between electrodes (2 cm), κ is the conductivity (mS.cm) measured by conductivity meter, A_e is the total area of cathode (400 cm^2) and i is the current density (mA/cm^2)

Experimental

The growth media (base electrolyte) contained 0.8 g/L $(NH_4)_2SO_4$, 2 g/L $MgSO_4 \cdot 7H_2O$, 0.4 g/L K_2HPO_4, 5 mL/L Wolfe's Mineral Solution, 10 mM or 144 mM of $FeSO_4 \cdot 7H_2O$ and pH adjusted to 1.8 in most cases. 70 mM citrate is added in the form of 35 mM of $Mg_3(C_6H_5O_7)_2 \cdot 9H_2O$ when present. Generally, the inlet flow contained

around 360 mM of $CuSO_4 \cdot 5H_2O$. All chemicals were purchased from Sigma Aldrich unless otherwise noted.

The inlet solution is pumped in with Cole Parmer Masterflex L/S pump onto three cathodes in parallel by three pump heads, totaling 700 mL/h. The outlet solution is pumped out at the same rate by one pump on top of the solution at a graduated liquid level to maintain the volume in the electrowinning device to be 1.5 liters. Air sparging was performed with Tetra Whisper air pump 60. The air tubes were bundled together with the inlet solution tubes under the three cathodes.

Cathodes in the electrowinning device are corrosion-resistive stainless steel 316. Platinized titanium mesh anode was purchased from Stuller, Inc. Mixed metal oxides (MMO) anodes are purchased from De Nora Tech, Inc. Constant electrical current was supplied with DC power supply from Agilent Technologies (N8734A) with a built-in voltage monitor.

The Fe^{2+} concentration was determined by titration of 0.1 M cerium (IV) sulfate into mixtures of solution samples (1 mL) and ferroin indicator (0.1 mL), and observing the color change. Since the combination of Fe^{2+} and Fe^{3+} at any time should be equal to the initial Fe^{2+} concentration, Fe^{3+} can be simply calculated by deducting the Fe^{2+} amount from the total. The conductivity of the solution was measured with portable Orion Star conductivity and temperature meter from Thermo Scientific.

The cupric ion concentration was measured with Atomic Adsorption Spectrophotometer (AAS) from Buck Scientific (Model 200A) with a hollow cathode lamp for elemental copper (P/N 4114). The copper primary adsorption line of 324.7

nm was chosen as the detection wavelength. 5.3 A of current was applied to the lamp for all measurements, and a standard calibration curve was developed for data analysis.

Results and Discussion

Assumptions and Calculations

A typical cell density of *A. ferrooxidans* is around 0.01 to 0.1 OD (1 OD = $8.3*10^9$ cell/mL).[11, 12] Under optimal conditions, our lab has achieved cell densities of 0.5 OD. With the copper redox couple mediated system, an aggressive projection of cell density could be up to 1 OD. The electrowinning cell was designed with the capability to maintain the mass and electron balance for a 7-liter bioreactor with 1 OD of *A. ferrooxidans* cells. The rate of consumption for Fe^{2+} is about 0.0058 mmol per 10^9 cells per hour. Thus in a 7L bioreactor of 1 OD, the rate of Fe^{2+} consumption is 0.336 mol/h, equivalent to 0.168 mol/h of copper. Assuming a current efficiency of 90%, by Faraday's law, the required current needed is 10 A.

Assuming a current density of 25 mA/cm^2 that is typically utilized in an electrowinning cell,[13] the total surface area for the cathode was set to 400 cm^2. Four anode sheets and three cathode sheets of equal size (8 cm in width; 8.3 cm in length) were placed in parallel, with each cathode sheet surface faced with an anode surface at a distance of 2 cm. All 7 electrodes were secured in the electrowinning device of 10 cm in width, 15 cm in length and 16 cm in height. Solution was filled up to about 10 cm from the bottom to make up a volume of 1.5 liter.

With an inlet copper concentration of 360 mM, at 700 mL/h, the outlet copper concentration could be expected to be reduced to around 120 mM at 90% current efficiency and 10 A of current. The outlet copper concentration can be adjusted by changing the flow rate.

Cell Voltage and Its Dependence on Anode Material, Presence of Citrate and Temperature

Most industrial applications use lead anodes instead of platinized titanium anodes due to its much lower costs, despite the higher resulting cell potential and additional maintenance requirements.[14, 15] Some recent studies have shown promising dimensionally stable anodes made with mixed metal oxides (MMO), which is not only several folds cheaper than platinized titanium, but appears to be more catalytic for water oxidation.[16, 17]

MMO anodes were compared to platinized titanium anodes. The inlet solution contained 360 mM Cu^{2+}, 10 mM of Fe^{2+} and 70 mM citrate in addition to the base electrolyte. As shown in Figure 2 (red vs. black plots), the overall cell voltage in both experiments decreased by about 0.6~0.7 V. This decrease could be well explained by the decrease in IR drop as calculated from measured conductivities with equation (10). The increase in conductivity results from an increase in the concentration of H^+ as shown in Figure 4.

On the other hand, the cell with MMO anodes operated at potentials constantly lower than that with platinized titanium anodes by about 0.4 V, with a low cell voltage of only 3.3 V at the end of the electrowinning cycle. The 0.4 V of

reduction with MMO anode is consistent with industrial estimates. By utilizing MMO anodes, our cell voltage was reduced by 11%. Notably, the MMO anodes generally cost about 4 times less than platinized anodes.

Also with MMO anodes, experiments without citrate were performed as a comparison (red vs. green plots in Figure 2). Again, the conductivity and ohmic drop were similar. However, the cell voltage with no citrate was slightly reduced by about 150 mV. When 70 mM citrate is present, it is expected that significant amounts of copper in the solution would exist in a chelated form rather than the more readily reduced form of Cu^{2+}. The reduced Cu^{2+} concentration leads to an increase in overpotential for copper reduction on the cathodes and thus the 150 mV increase in cell voltage.

The temperature in commercial electrowinning facility is usually around 55 °C or 65°C in order to maximize the conductivity of solution and thus minimize ohmic drop. Thus temperature is an important factor. As shown in Figure 3, we took the outlet solution at 10 hours (near steady state) of the experiment shown in red in Figure 2 (MMO anodes and with citrate) and measured its conductivity at increasing temperature from 23°C up to 52°C. A linear increase in conductivity at a rate about 1.2 mS.cm/°C from 23°C to 38°C. was observed. After 38°C, little increase in conductivity was gained with elevated temperature.

Copper Reduction and Acid Generation Ability at Low and High Iron Concentrations

The aforementioned three experiments shown in Figure 2 were also monitored in terms of Cu^{2+} concentration, Fe^{2+} concentration and pH in the outlet solution of electrowinning device. As shown in Figure 4, in all three cases, both Cu^{2+} concentration and pH decreased in a similar manner, with Cu^{2+} approaching 130 mM and pH approaching 0.7 after 10 hours of electrowinning. Assuming 100% current efficiency, the steady-state Cu^{2+} concentration would be 110 mM based on 360 mM of Cu^{2+} inlet concentration, which is close to our experimental result. The pH during the experiment with no citrate decreased slightly faster than the other two because of the absence of buffering by citrate. At only 10 mM of inlet Fe^{2+} concentration, its effect on electrowinning performance is not significant.

At an iron concentration of 144 mM of Fe^{2+} in the inlet solution, experiments were performed at 10 A with MMO anodes and with and without citrate. As shown in Figure 5, after 4.5 hours, the outlet Cu^{2+} concentration was above the results at low iron concentration. Without citrate, Cu^{2+} concentration decreased from 360 mM to about 240 mM; while when 70 mM citrate is present decreased to 270 mM. As shown in Figure 5, in both cases, Fe^{2+} concentration decreased significantly by roughly half. The concentration of outlet Fe^{2+} reached steady state in only about an hour. When both Fe^{2+} and Fe^{3+} exist in the solution at high concentrations of about 70 mM, the redox couple is expected to lower the current efficiency. When citrate is present, Cu^{2+} and Fe^{2+} concentration, as well as pH all varied more steadily and to less extent than the no citrate cases.

Evaluation of Current Efficiency and Deposit Quality

It has been consistently seen that the adhesion of copper deposit on stainless steel cathodes is poor in the presence of citrate. Two sets of deposit with and without citrate are given in Figure 6 at both high and low acid concentrations in the solution. When citrate is not present, deposits are smooth and well adhered. In the presence of citrate, the poorly adhered deposits fall from the cathode, and current efficiencies cannot be determined by weighing the cathodes. In these cases, the current efficiency of copper reduction is computed with copper concentrations, albeit with lower confidence in the results. For example, with good deposits, current efficiencies were calculated by both methods and are listed on Figure 6. At low iron concentration, the current efficiencies were around 90%, while at high iron concentration, the current efficiency decreased to about 70%. The lowest current efficiency was observed when both high iron concentration and citrate were present. In other cases when only 10 mM of iron is supplied, the current efficiencies were also around or above 90%, which is consistent with industry standards.[13]

Electrowinning Experiments under Other Conditions

Aside from the above standard conditions, tests on other conditions were also performed, with two examples shown in this section. Figure 7 shows how the cell performed over 4 hours of time when high Fe^{2+} concentration of 144 mM and low Cu^{2+} concentration of only 85 mM is electrowon at a high current of 16 A. Under such an extreme condition, Cu^{2+} is completely depleted at the outlet, with almost 60 mM of Fe^{2+} turned into Fe^{3+}. The variation of pH, as well as conductivity was not as significant as previous cases, since the cyclic oxidation and reduction of iron redox

couple consumed most of the current on the electrodes. Also, at such an aggressive condition, the cell voltage was 5.4 V.

Experimental results obtained at 4 A is shown in Figure 8, where 10 mM of Fe^{2+} and 380 mM of Cu^{2+} is supplied. At such mild conditions, outlet Cu^{2+} remained at high level above 300 mM with an effluent pH of 1.2. The biggest advantage that comes along with such a low current density is that the cell voltage is only 2.5 V. When the demand for electrons in the bioreactor is low, it is desired that the current be set to a lower value accordingly. Again, the outlet Cu^{2+} concentration and pH could be easily adjusted with the flow rate whenever needed.

A closer look at the dependence of cell voltage on supplied current is demonstrated in Figure 9. The data were obtained with platinized titanium anodes and normal electrolytes in the electrowinning cell. Clearly the cell voltages after 4 hours of electrowinning were lower than those at the onset of the experiment due to the increase in acid content. The trend of the plots is well characterized by Butler-Volmer equation, where the low overpotential region and high overpotential region could be distinguished. The plots serve as a general guideline for future needs of adjusting current based on the scale of bioreactor.

Conclusions

In this study, a copper electrowinning cell was designed for an integrated electrofuels process. A power saving effect was observed by utilizing novel mixed metal oxides anodes. Copper deposits adhered well both at low and high iron concentrations without citrate; but with 70 mM of citrate, deposit quality is poor.

The current efficiency during electrowinning is above 90% at low iron concentration and 70% at high iron concentration.

ACKNOWLEDGMENTS

This research was supported by New York Battery & Energy Storage Technology (NY-BEST). The authors gratefully acknowledge Danjie Lu of Columbia University for her assistance in performing experiments.

Reference

1. M. P. Silverman and D. G. Lundgren, J Bacteriol **77** (5), 642-647 (1959).

2. M. Nemati, S. T. L. Harrison, G. S. Hansford and C. Webb, Biochemical Engineering Journal **1** (3), 171-190 (1998).

3. W. J. Ingledew, Biochimica et Biophysica Acta (BBA) - Reviews on Bioenergetics **683** (2), 89-117 (1982).

4. D. G. Karamanev and L. N. Nikolov, Biotechnol Bioeng **31** (4), 295-299 (1988).

5. D. T. Lacey and F. Lawson, Biotechnol Bioeng **12** (1), 29-50 (1970).

6. D. G. MacDonald and R. H. Clark, The Canadian Journal of Chemical Engineering **48** (6), 669-676 (1970).

7. J. R. Smith, R. G. Luthy and A. C. Middleton, Journal Water Pollution Control Federation **60** (4), 518-530 (1988).

8. K. H. Gayer and L. Woontner, The Journal of Physical Chemistry **60** (11), 1569-1571 (1956).

9. X. Z. Li, R. Mercado, T. Kernan, A. C. West and S. Banta, Biotechnol Bioeng **111** (10), 1940-1948 (2014).

10. D. Pradhan, J. G. Ahn, D. J. Kim and S. W. Lee, Korean J Chem Eng **26** (3), 736-741 (2009).

11. X. Li, R. Mercado, S. Berlinger, S. Banta and A. C. West, AIChE Journal **60** (12), 4008-4013 (2014).

12. X. Li, R. Mercado, T. Kernan, A. C. West and S. Banta, Biotechnol Bioeng **111** (10), 1940-1948 (2014).

13. N. T. Beukes and J. Badenhorst, J S Afr I Min Metall **109** (6), 343-356 (2009).

14. M. Clancy, C. J. Bettles, A. Stuart and N. Birbilis, Hydrometallurgy **131–132** (0), 144-157 (2013).

15. W. C. Cooper, Journal of Applied Electrochemistry **15** (6), 789-805 (1985).

16. A. L. Antozzi, C. W. Brown Jr and A. Calderara, presented at the Electrometallurgy 2012 - TMS 2012 Annual Meeting and Exhibition, March 11, 2012 - March 15, 2012, Orlando, FL, United states, 2012 (unpublished).

17. K. Asokan and K. Subramanian, *COPPER ELECTROWINNING USING NOBLE METAL OXIDE COATED TITANIUM - BASED BIPOLAR ELECTRODES*. (Minerals, Metals & Materials Soc, Warrendale, 2009).

List of Figures

Figure 1

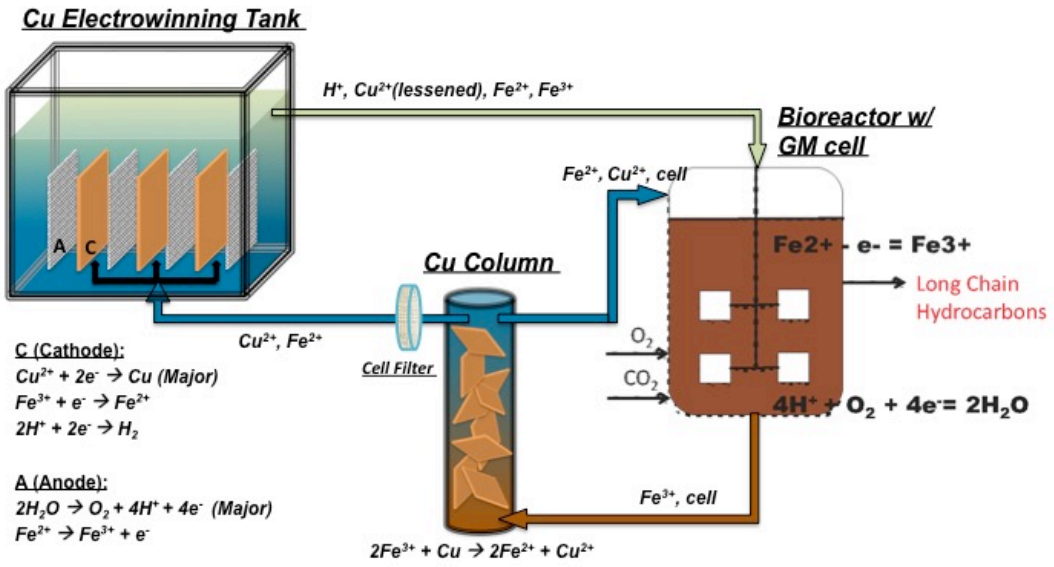

Figure 1. Schematic diagram of continuous hydrocarbon production system with *A. ferrooxidans* cells mediated *by* Cu^{2+}/Cu redox couple

Figure 2

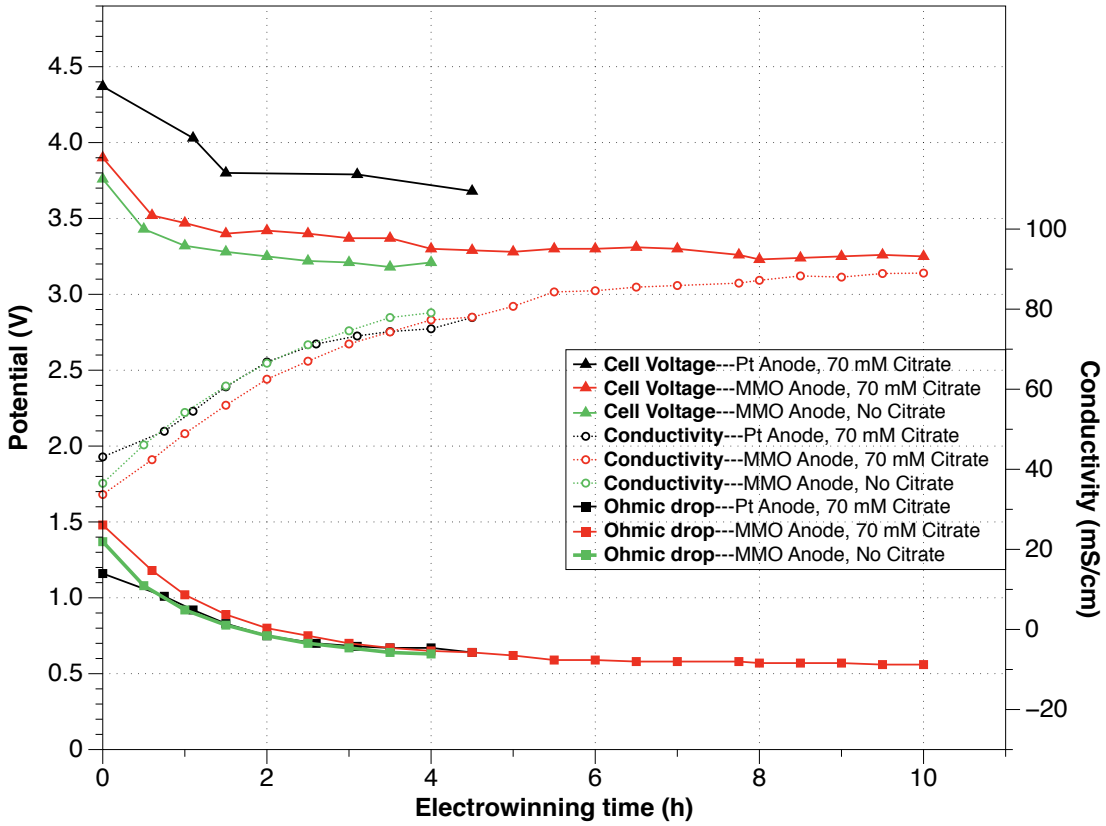

Figure 2. Variation of cell voltage, ohmic drop and conductivity during electrowinning experiments under three conditions. In the legend: "Pt Anode" represents platinized titanium anode; "MMO Anode" represents mixed metal oxides anode

Figure 3

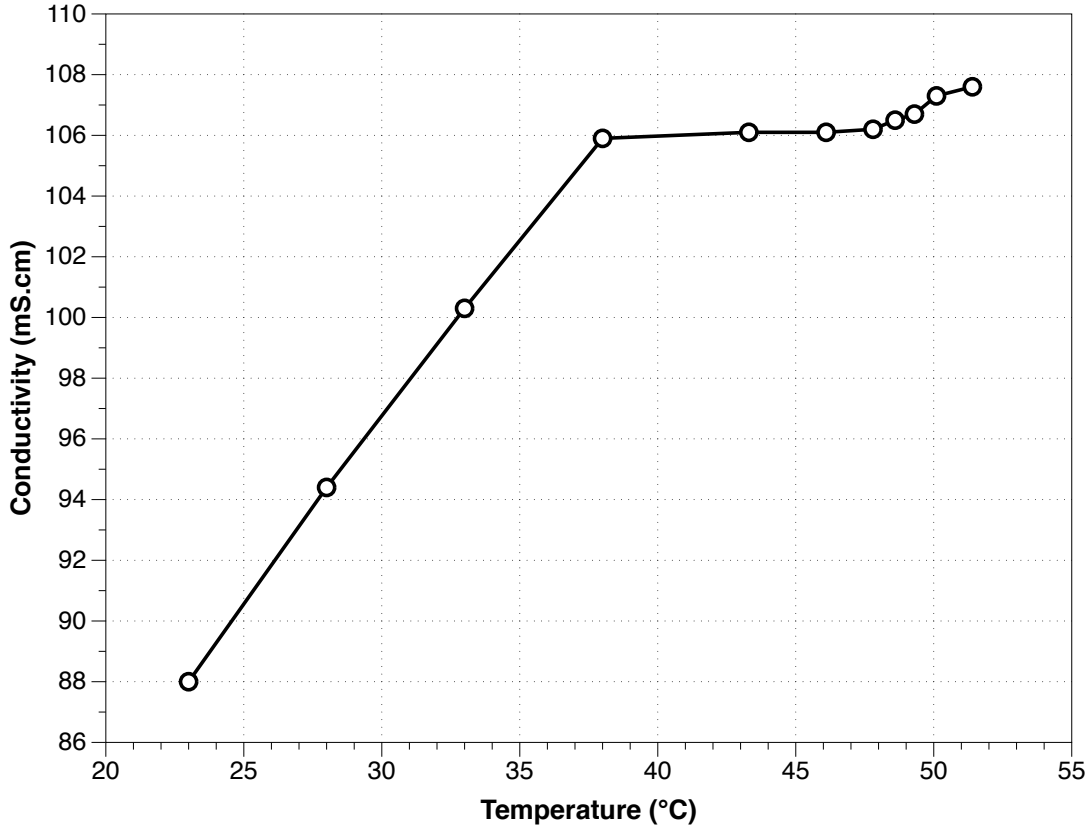

Figure 3. Conductivity variation as a function of temperature. Sample solution was taken from a typical electrowinning experiment at its steady state

Figure 4

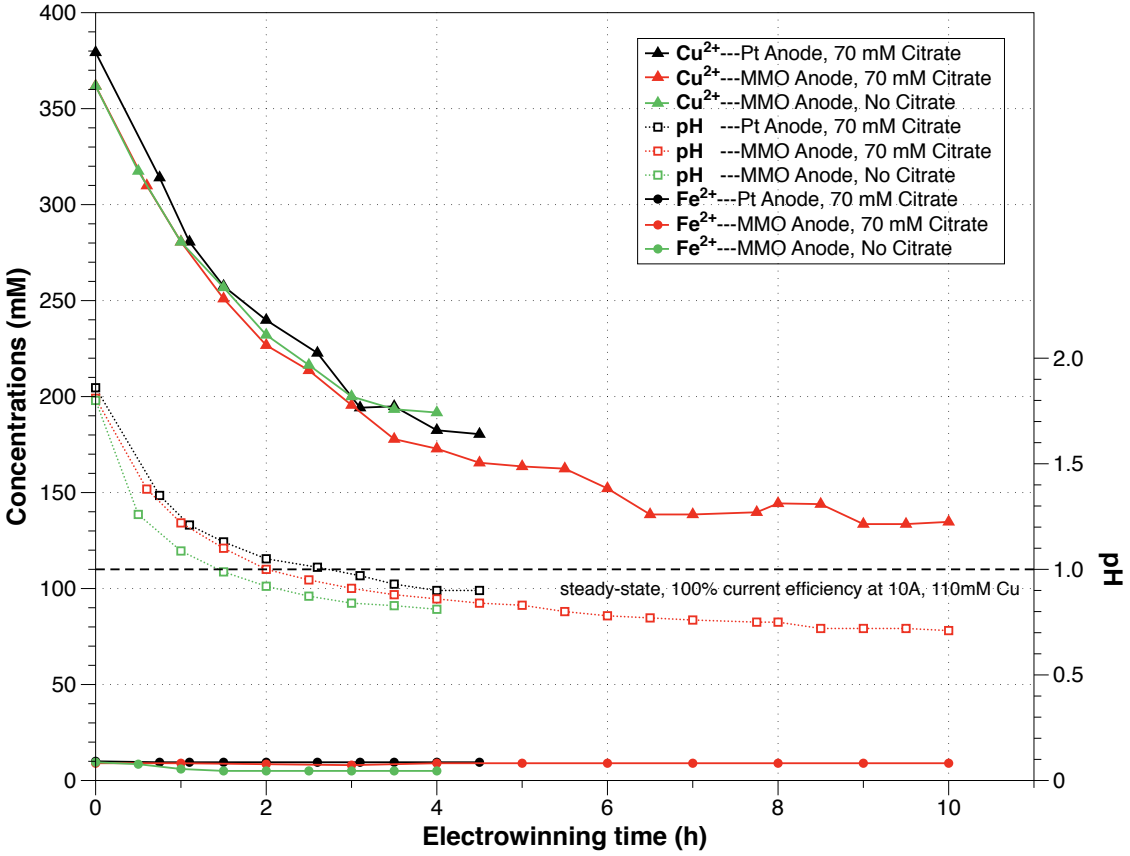

Figure 4. Variation of Cu^{2+} and Fe^{2+} concentrations and pH in the outlet solution of electrowinning device as a function of electrowinning time under three conditions with low iron inlet concentration. (Same experiments with Figure 2)

Figure 5

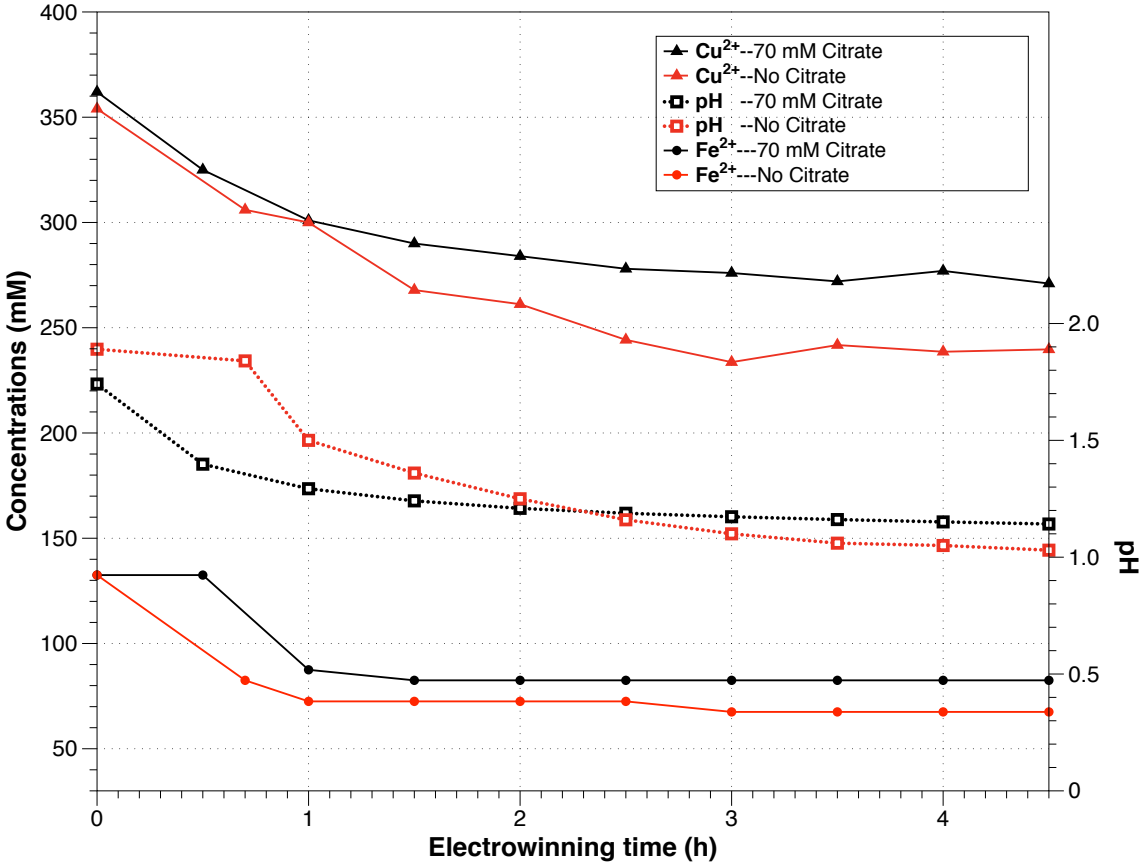

Figure 5. Variation of Cu^{2+} and Fe^{2+} concentrations and pH in the outlet solution of electrowinning device as a function of electrowinning time with high iron inlet concentration of 144 mM. (red) no citrate; (black) with 70 mM citrate

Figure 6

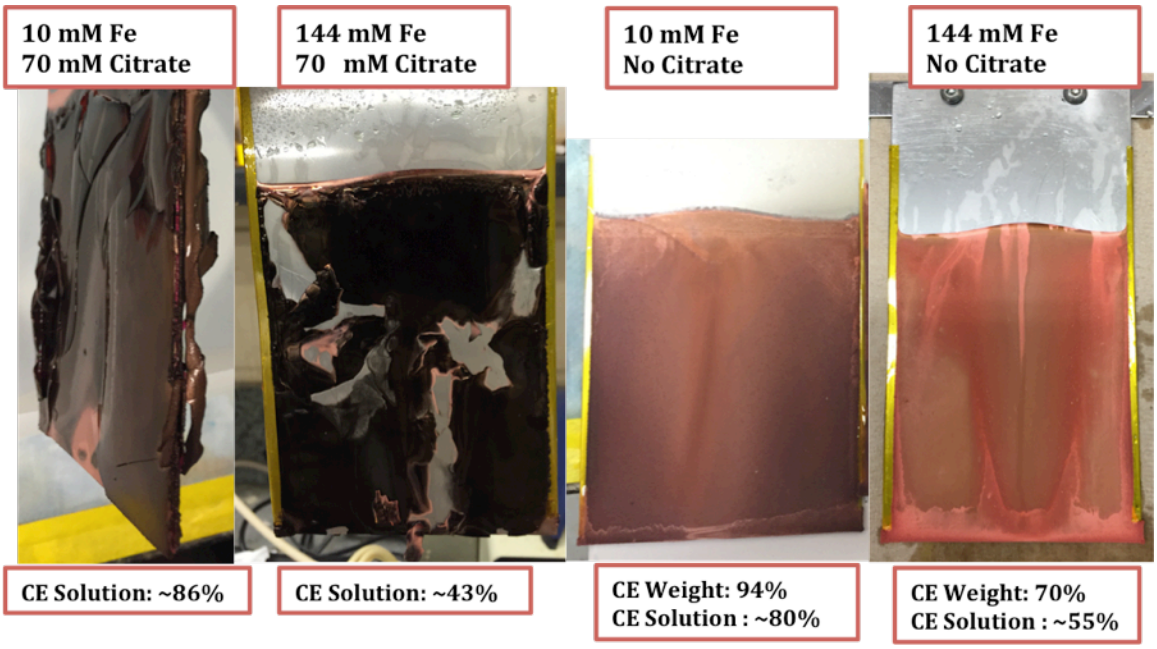

Figure 6. Deposits of copper on stainless steel cathodes under four conditions labeled on top of images. "CE Weight" represents current efficiency calculated by weighing the mass of copper deposit; "CE Solution" represents current efficiency calculated by copper concentrations

Figure 7

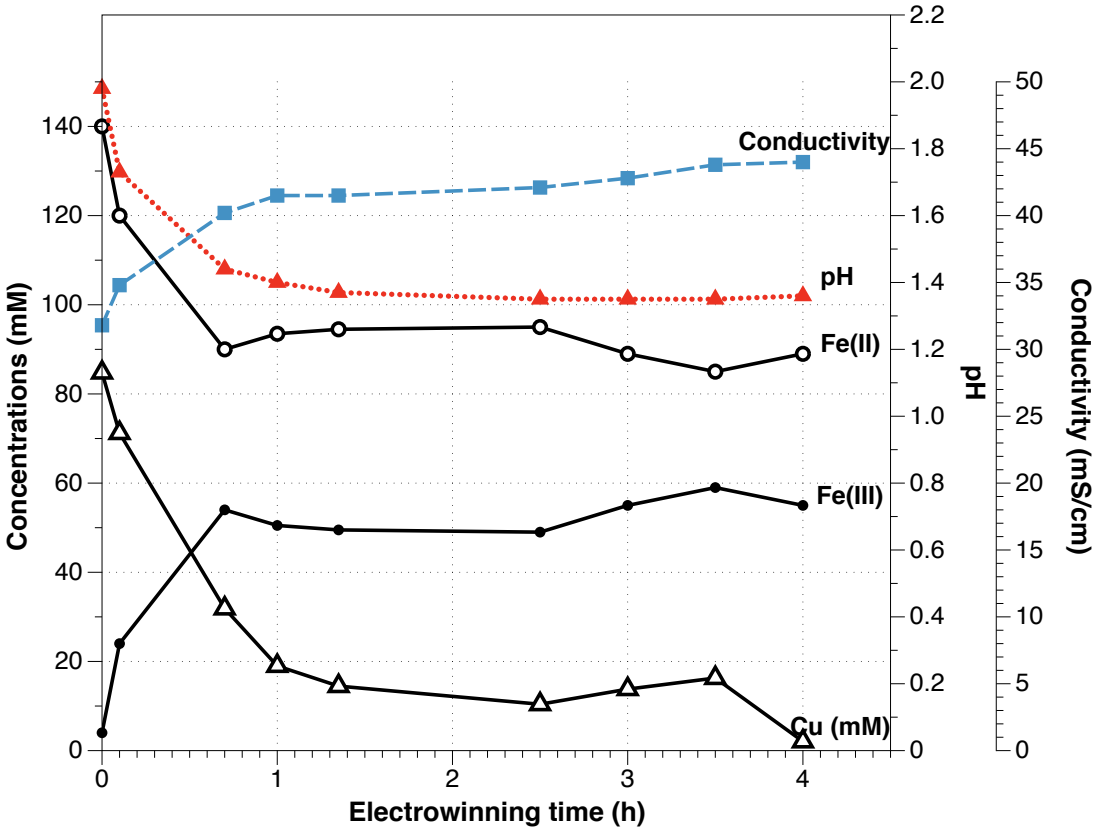

Figure 7. Variation of conductivity, pH, Fe^{2+}/Fe^{3+} and Cu^{2+} concentrations during electrowinning experiment at 16 A. Combination of high inlet iron concentration of 144 mM and low inlet copper concentration of 80 mM is supplied

Figure 8

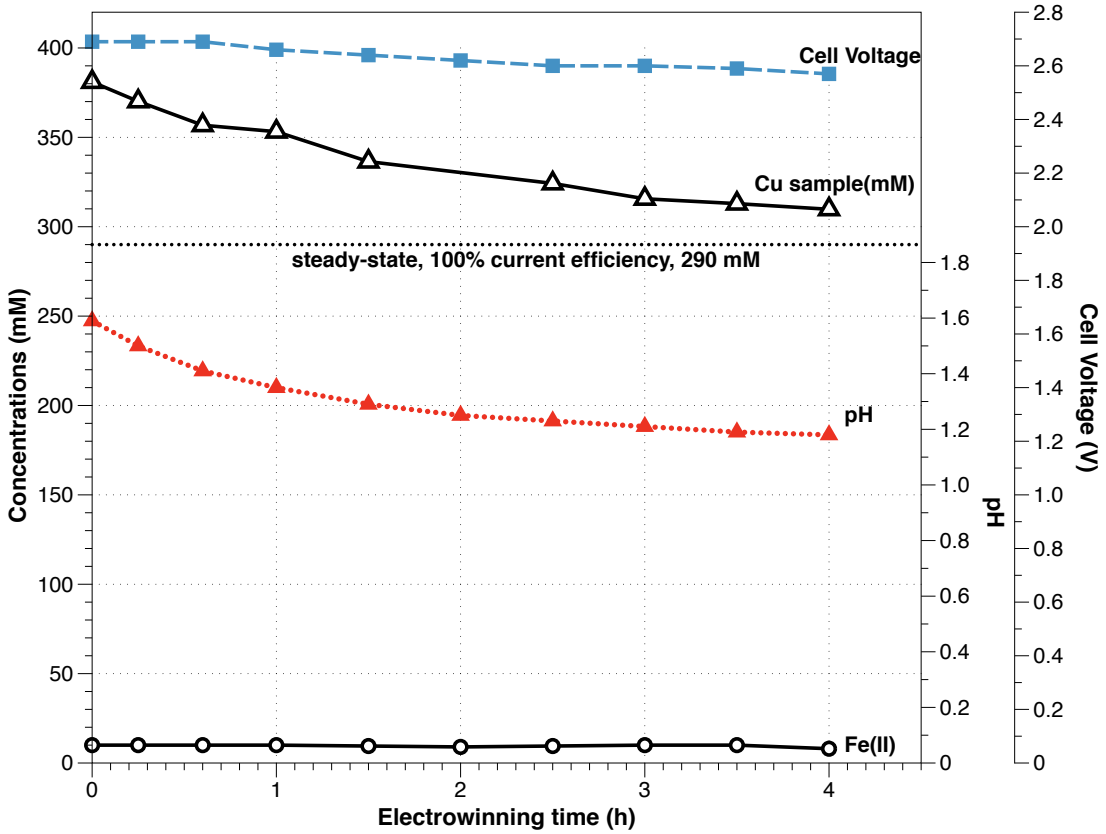

Figure 8. Variation of cell voltage, pH, Fe^{2+} and Cu^{2} concentrations during electrowinning experiment at 4 A. Combination of low inlet iron concentration of 10 mM and high inlet copper concentration of 380 mM is supplied

Figure 9

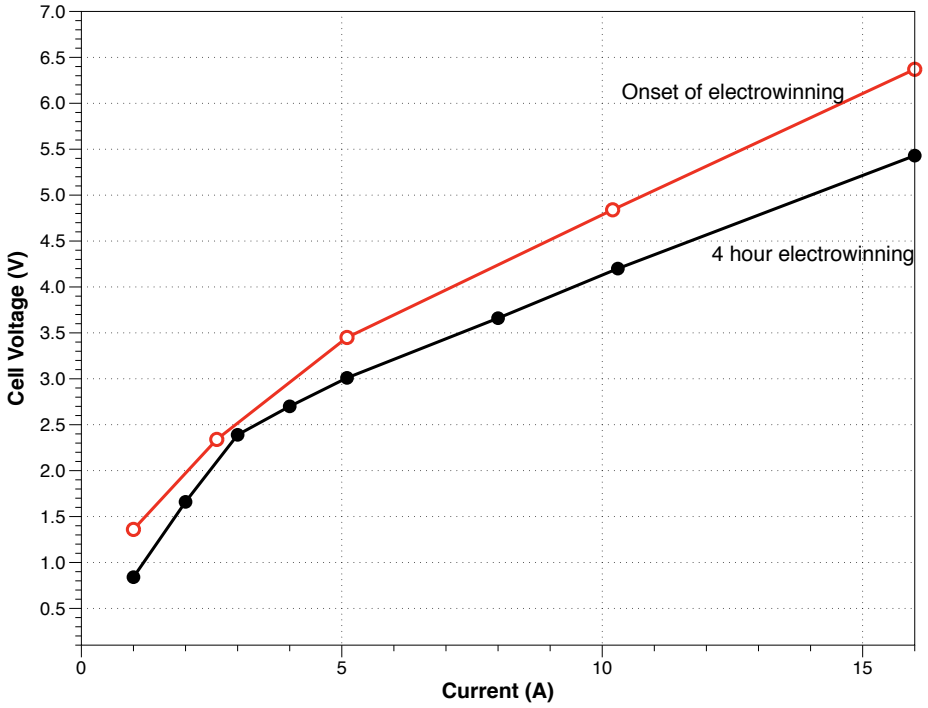

Figure 9. Dependence of cell voltage on applied current from 1 A to 16 A. Observation is done both at the onset and 4 hour of electrowinning experiment. Normal electrolyte and platinized titanium anode was used.

Chapter 7:

Conclusion

In the first part of the thesis, copper deposition techniques for interconnect fabrication are discussed. Electroless copper deposition as a promising candidate for next generation metallization method was studied. Lab-scale tools for copper electrodeposition were developed.

Electroless copper deposition is presented in chapter 2. The DMAB bath performance was characterized, which showed that the rate of deposition most dramatically increases with an increase in pH, followed by temperature and then the concentrations of DMAB and copper sulfate. Inhibition was seen with additional EDTA and the addition of PEG. Mixed potential theory studies revealed a catalytic effect of the presence of the anodic reaction to the cathodic reaction.

Nucleation study results showed that the nucleus density is consistently reduced by the addition of the PEG by about half, that the nucleus density at pH 8.2 is significantly higher than those at pH 8.6 and 8.9, and that the lower temperature of 22°C results in higher nucleus density than at 55°C. The substrate also influenced nucleus density, with the highest nucleus density obtained on pretreated ruthenium, followed by PVD copper and then cobalt. With the use of a combination of SAM pretreatment and Pd activation, copper nuclei was formed onto non-catalytic silica substrate with comparable nucleus density.

In chapter 3, a novel additive aging cell for copper electrodeposition process is presented. A modified anolyte chemistry for cathode SPS aging was proposed to overcome the limitation of membrane selectivity, which leads to significant acid level and copper content variation during aging process. A CVS method successfully quantified SPS concentration in copper plating bath. Results showed that SPS aging on cathodes is significant. The rate of aging as a function of charge passed is higher at lower current density and higher acid level. Also, the addition of PEG reduces the rate of SPS aging. Through characterization of mass transfer of SPS on rotating cylinder electrode, it was found that the aging process under current operating conditions may be diffusion controlled. By monitoring the pH change of the membrane-separated compartments before and after aging experiments, the effectiveness and practicality of using modified anolyte chemistry in achieving desired transport properties was validated.

Another tool design that improves uniformity of copper electrodeposition is presented in chapter 4, and this is also important to characterization of additives. By simulation, optimal insulating shields for lab scale plating tool was designed to redistribute current for much better film uniformity during copper plating on coupons. In the sensitivity screening, it was concluded that the shield-to-substrate distance and inner radius of shield are the most critical factors in redistributing current density. Some of the designs were validated in experiments with good agreement. A significant reduction in the disparity between the minimum current density and the average was obtained. This design was also tested to be very simply integrated and manufactured.

The second part of the thesis covers two copper deposition applications coupled with biological elements: biosensor signal amplified with electroless copper deposition and biofuel production integrated with a copper electrowinning cell.

A novel sensor signal amplification method that utilizes electroless copper deposition to image adsorbed phage is presented in chapter 5. A non-formaldehyde electroless copper deposition bath was utilized so that the deposition operates at room temperature, non-corrosive pH and lower toxicity. Evaluation studies of the protocol to monitor phage concentration suggest that the time required for a deposit to appear is the most accurate and robust. The concentration of insertless phage was successfully quantified by the electroless deposition signal. It was also found that bio-engineered phages perform similarly to insertless phage during the signal transduction process with electroless deposition. Finally, a detection limit in the ppt level is directly achieved on multiple substrates, and a pre-concentration device can be utilized to detect phage of lower concentrations without significantly increasing the time for detection.

Last but not least, chapter 6 presents a design of a copper electrowinning cell to be used in an integrated electrofuels process. A power saving effect was observed by utilizing novel mixed metal oxides anodes. Copper deposits adhere well both at low and high iron concentrations without citrate; but with 70 mM of citrate, deposit quality is poor. The current efficiency during electrowinning is above 90% at low iron concentration and 70% at high iron concentration.